Track Based Alignment of the CMS Silicon Tracker and its Implication on Physics Performance

Dissertation

zur Erlangung des Doktorgrades

des Departement Physik

der Universität Hamburg

vorgelegt von

Jula Draeger

aus Berlin

Hamburg

2011

Gutachter der Dissertation:	1. Prof. Dr. Peter Schleper 2. Prof. Dott. Ernesto Migliore 3. Dr. Oliver Buchmüller
Gutachter der Disputation:	1. Dr. Erika Garutti 2. Prof. Dr. Johannes Haller
Datum der Disputation:	19.08.2011
Vorsitzende des Prüfungsausschusses:	Dr. Georg Steinbrück
Vorsitzender des Promotionsausschusses:	Prof. Dr. Peter Haussschildt
Leiterin des Fachbereichs Physik:	Prof. Dr. Daniela Pfannkuche
Dekan der Fakultät für Mathematik, Informatik und Naturwissenschaften:	Prof. Dr. Heinrich Graener

Abstract

In order to fully exploit the discovery potential of the CMS detector for new physics beyond the Standard Model at the high luminosity and centre-of-mass energy provided by the Large Hadron Collider, a careful calibration of the detector and profound understanding of its impact on physics performance are necessary to provide realistic uncertainties for the measurements of physics processes. This thesis describes the track-based alignment of the inner tracking system of CMS with the Millepede II algorithm. Using the combined information of tracks from cosmic rays and collisions taken in 2010, a remarkable local alignment precision has been reached that meets the design specifications for most regions of the detector and takes into account instabilities of the detector geometry over time. In addition, the impact of the alignment on b tagging or the Z boson resonance are investigated. The latter is studied to investigate the impact of correlated detector distortions which hardly influence the overall solution of the minimisation problem but introduce biases in the track parameters and thus the derived physics quantities. The determination and constraint of these *weak modes* present the future challenge of the alignment task at CMS.

Zusammenfassung

Um das volle Entdeckungspotential bezüglich neuer Physik jenseits des Standard Models mit dem CMS Detektor ausschöpfen zu koennen, ist eine sorgfältige Kalibration und ein profundes Verständnis auftretender Detektoreffekte von Nöten, um realistische Abschätzung für die detektorspezifischen Unsicherheiten angeben zu können. In dieser Arbeit wird das spurbasierte Alignment des Silizium-Spurdetektors von CMS mit dem Millepede II Algorithmus beschrieben, welches unter Verwendung der Informationen aus Spuren der kosmischen Strahlung und aus Kollisionendaten bei Schwerpunktsenergien von 7 TeV, eine hervorragende lokale Alignment Präzision erzielt, die in weiten Teilen des Detektors die Designspezifikationen erreicht. Desweiteren werder die Auswirkungen des Alignments auf das 'b-tagging' oder die rekonstruierte Z-Boson Resonanz untersucht. Letztere speziell im Hinblick auf solche Detektorverzerrungen, welche die Lösung des zu Grunde liegenden Minimierungsproblems kaum verändern, dafür aber die Spurparameter und die aus ihnen abgeleiteten Größen beeinflussen. Die Determinierung und Vermeidung solcher *weak modes* stellen die zukünftigen Herausforderungen an das Alignment dar.

List of Figures

List of Tables

Contents

Chapter 1

Introduction

The standard model (SM) of particle physics describes the fundamental structure of matter with a remarkable accuracy. Except for the Higgs boson, considered to be responsible for the masses of fundamental particles, all components predicted by the SM could be confirmed experimentally over the last 30 years. A prime motivation for building the Large Hadron Collider (LHC) is thus to either confirm or falsify the existence of a SM Higgs boson. In spite of the outstanding achievements of the SM, its scope is limited to an energy regime of about 1 TeV and extensions to the theory are necessary to address the hierarchy problem or to provide a candidate for dark matter necessary to explain various observations in astrophysics. Various theoretical extensions have been developed, amongst others, theories that predict super-symmetrical particles or extra dimensions. Depending on the parameters chosen, the predicted values are accessible at the LHC. Prior to hopeful discoveries, the precise understanding of the machines and detection devices is an essential milestone.

The CMS detector, one of the two multipurpose detectors, was built to precisely measure the momenta and energies of the decay products of the short lived particles produced in the proton proton collisions and thus allow the reconstruction of the event. Tracks of charged particles play a key role in the measurement and reconstruction of electrons, muons and taus as well as jets that they are associated to. To measure these charged tracks, the innermost tracking system was built, facing challenging demands on the hardware due to the high energies and high luminosity provided by LHC. Withstanding the high radiation in the innermost detector volume, the over 16,000 silicon modules have been designed to provide precise position measurements of the hits from a particle traversing the detector. A major systematic uncertainty of this measurement is the accuracy of the modules position itself. Given the limited mounting precision and the inaccessibility of the tracker volume during operations, the most accurate method to determine the silicon-module positions is to use the information of the data recorded by CMS when traversed by a charged particle.

Within the thesis presented here, the track-based alignment of the CMS silicon tracker is described using the combined information of tracks from cosmic rays and collisions in order to determine the module positions. Both track and small corrections

to the module positions are considered as free parameters of a simultaneous fit. The Millepede II algorithm is used to reduce the complexity of the resulting optimisation problem.

Besides a detailed description of the alignment strategy, several validation methods are presented used to monitor and test the quality of the achieved alignment. Therefore, basic alignment and tracking quantities are tested as well as information from combined physics objects.

Chapter 2 briefly introduces the current understanding of particle physics summarized in the formulation of the Standard Model. The predicted but not yet measured Higgs boson, assumed to be responsible for the generation of particle masses, is one of the prime motivations for the construction of the Large Hadron Collider and its experiments which are introduced in chapter 3. Focussing on the inner tracking system of CMS as the subject to the alignment procedure, necessary background information concerning the hardware is given before the basic ideas and mathematical concepts of track-based alignment are introduced in chapter 4. Besides a general description of the Millepede II algorithm, an external software package used to solve the minimisation problem formulated in track-based alignment, the CMS specific interfaces are explained in this chapter as well.

Chapter 4 presents the alignment strategy applied to the data recorded by CMS in 2010 and the results are discussed on the bases of several validation methods. Finally, basic studies concerning the impact of the achieved alignment and its remaining uncertainties on different physics processes are presented in chapter 6. First, the b tagging efficiency is compared for different possible misalignment scenarios. In addition, the Z boson resonance is used to test for biases arising in the track parameters arising from the alignment. The chapter concludes with ideas and suggestions on how to extend the presented strategy.

Chapter 2

Fundamental particles and their interaction with matter

The Standard Model (SM) of particle physics summarises our current understanding of over 40 years of experimental and theoretical research in high energy physics, by reducing the observed phenomena to a limited number of elementary particles and three of the four fundamental interactions. Only gravity is not implemented into the theoretical framework of the Standard Model as it is not possible so far to describe it with the same theoretical tools i.e. quantum field theory. The good agreement of theoretical predictions and precise experimental measurements stress the power of the underlying gauge principle. Section 2.1 gives a short overview of the Standard Model particles and fundamental interactions as well as a short interpretation of physics phenomena within the framework of the Standard Model.

In section 2.2 the underlying theory will be briefly introduced and applied to describe physics phenomena like interactions between particles with electric charge. Using the same methods, the Higgs mechanism can be included in the Standard Model which is necessary to introduce the particle masses and thus keep the Standard Model a consistent theory that describes nature. Although the Standard Model shows a remarkable predictive precision for the energy regime tested in the last 40 years, its validity range is limited and an extension is necessary for energies above 1 TeV[1]. To investigate that region of interest the Large Hadron Collider (LHC) has been built. Its centre-of-mass energy exceeds those of all past experiments and thus enables the search for physics beyond the Standard Model as well as measurements of Standard Model particle properties which suffer from statistical limitations at lower centre-of-mass energies.

For both tasks a thorough understanding of the experimental detectors is crucial. Therefore, known particle properties can serve as calibration values to test and if necessary adjust the detector output signals. The Z boson can serve as one of these *standard candles* and, therefore, its production mechanism is exemplary discussed in sections 2.2.3 and 2.3. It has been measured with high precision at the LHC's

[1]Throught this thesis, natural units are used in which $c = \hbar = 1$

predecessor: the Large Electron Positron Collider (LEP). Furthermore, the underlying theory is well understood and can be modelled precisely in the simulation.

Another powerful source of information in this context are muons generated by cosmic rays interacting with the atmosphere which will be described in section 2.5.

2.1 Constituents of the Standard Model

The theory of subatomic forces embodied in the Standard Model of particle physics is the outcome of theoretical developments combined with experimental discoveries over many decades beginning in 1927 when Dirac published the first pioneering paper combining quantum mechanics with the classical theory of radiation. The relativistic expansion of this approach and the discovery of antimatter in 1932 were the beginning of the great success of the Standard Model with its fermion spectrum completion in 2000 with the discovery of the τ neutrino [13].

The Standard Model consists of both particle types that are distinguished in quantum mechanics. All matter particles are fermions, which carry half integer spin and obey the Pauli exclusion principle. They split into leptons and quarks, which can be separated into three generations as shown in table 2.1. The lepton pairs in each generation contain one electrically charged particle and a corresponding neutrino. While the charged leptons participate in both the electromagnetic and weak interactions, the neutrino only interacts via the weak force. Both quarks in each generation carry electric charge and thus participate in electromagnetic and weak interactions. In contrast to the leptons, quarks also participate in the strong interaction, which is expressed by the additional colour charge. In section 2.2.1 it will be shown that the electroweak theory distinguishes between right and left handed particles, such that each generation is subdivided into a left-handed lepton and quark doublet and right-handed singlets. In addition to the flavour, the generations only differ in the particles' masses, which are free parameters in the Standard Model and thus only accessible by measurement.

	1.Generation	2.Generation	3.Generation	Q	colour
Quarks	$\begin{pmatrix} u \\ d \end{pmatrix}_L \; u_R \; d_R$	$\begin{pmatrix} s \\ c \end{pmatrix}_L \; s_R \; c_R$	$\begin{pmatrix} t \\ b \end{pmatrix}_L \; t_R \; b_R$	$+2/3$ $-1/3$	R,G,B
Leptons	$\begin{pmatrix} \nu_e \\ e \end{pmatrix}_L \; \nu_{e\,R} \; e_R$	$\begin{pmatrix} \nu_\mu \\ \mu \end{pmatrix}_L \; \nu_{\mu\,R} \; \mu_R$	$\begin{pmatrix} \nu_\tau \\ \tau \end{pmatrix}_L \; \nu_{\tau\,R} \; \tau_R$	0 $+1$	—

Table 2.1: The matter particles of the Standard Model grouped in three generations which are subdivided in left-handed doublets and right-handed weak singlets. Q denotes the electric charge of the particles while colour refers to the colour charge of the strong interaction.

In the Standard Model of particle physics, interactions are described by the exchange of intermediate particles. Hence, the Standard Model contains additional intermediate particles for the electromagnetic, the weak and the strong force, which are bosons with integer spin. Both, the electromagnetic force, mediated by a γ, and the strong force, mediated by the gluons g, conserve all quantum numbers: parity P, charge conjugation C, time reversal T, lepton number L and baryon number B and the flavour quantum numbers. Both forces only act between particles within the same generation.
Weak interactions are subdivided into charged and neutral currents. While the neutral current can be described by a linear combination of Z^0 and γ interacting with both right and left-handed particles, the charged current mediated by $W^{\pm}$ interacts only with left-handed particles and, therefore, violates parity as well as charge conjugation to the maximum. The charged current is also able to change the flavour of a particle. As no flavour changing neutral currents have been measured, the resulting theoretical explanation, referred to as the GIM mechanism, predicted the existence of the charm quark before its discovery [14]. Furthermore, precision measurements concerning the Z boson decay at LEP exclude a forth generation of light particles.

Another difference between the interactions can be explained from the mass differences of the intermediate particles. While a massless photon leads to an infinite range of the electromagnetic force, the massive $W^{\pm}$ and Z^0 bosons result in a short ranged force of 10^{-17} m to 10^{-16} m. Their lifetime is bound to about $3 \cdot 10^{-24}$ s.
At distances of 10^{-18} the weak force has almost the same magnitude as the weak force while at distances of 10^{-17} it is already 10^5 times weaker. The strong force is also limited in range but the reason is not founded in large gluon masses – in fact gluons are treated as massless in the Standard model – but in a mechanism referred to as confinement. Since gluons themselves carry colour charge (unlike the photon which is electrically neutral), they interact with themselves. These gluon-gluon interactions constrain colour fields to string-like objects called "flux tubes", which exert constant force when stretched. Due to this force, quarks are confined within composite particles called hadrons which effectively limits the range of the strong interaction to 10^{-15} m, roughly the size of an atomic nucleus. The self-interaction of the gluon implies another feature of the strong force concerning the strength of its coupling. All coupling constants depend on the energy scale. An electron in quantum electrodynamics (QED) can emit virtual photons which subsequently annihilate into electron-positron pairs such that the original electron is surrounded by a cloud screening its "bare" charge. Therefore, the measurement of the electric charge depends on the distance of the used test charge. When moving the test charge closer to the electron, it penetrates the screening cloud such that the measured charge increases. In principle the same effect occurs for the colour charge in quantum chromodynamics (QCD), but the gluon self-interaction leads to the opposite behaviour of the familiar effect from electric charge screening. The resulting anti-screening is referred to as "asymptotic freedom". Two red quarks for example, asymptotically interact via colour fields of reduced strength, resulting in a state where they behave as essentially free, non-interacting particles.

In the following section the theoretical framework of the Standard Model shall be introduced by describing the particles and their interactions summarised above with mathematical tools. The theoretical description will lead to some open questions concerning the Standard Model, for example the origin of the particle masses.

2.2 The theoretical background of the Standard Model

The theoretical basis of the Standard Model can be found in group theory which underlies the treatment of symmetry. Following from the Noether theorem for classical mechanics or the analogon from quantum field theory, the Ward-Takahashi identities, each symmetry operation leads to a conserved physical quantity. The present belief is that all particle interactions are governed by local gauge theories. Some of the major concepts and the terminology of gauge theory can be found in Appendix A. The principle of global and local symmetries will be shown for QED in section 2.2.1. A necessary extension of the formalism, presented in section 2.2.2 will introduce the Higgs boson which has not yet been measured. Section 2.2.3 introduces the Feynman rules which can be derived from the QED formalism in order to calculate cross-sections and other measurable quantities. In section 2.2.4 the basic formalism is applied to strong interactions.

2.2.1 QED and electroweak unification

QED describes the interaction between charged particles and photons by formulating the photon field as a vector field

$$A_\mu \to A_\mu + \frac{1}{e}\partial_\mu \alpha \,. \tag{2.1}$$

that couples to a charged Dirac particle described by the complex field

$$\psi(x) \to e^{i\alpha(x)}\psi(x) \,. \tag{2.2}$$

which are gauge invariant under the symmetry group U(1) of unitary transformations, meaning that ψ can be altered by an arbitrary phase factor provided that A_μ is adjusted in a suitable way. Since A_μ should be invariant under equation 2.1 it can only involve the field strength tensor

$$F_{\mu\nu} = \partial_\mu A_\nu - \partial_\nu A_\mu \,. \tag{2.3}$$

This extension leads directly to the Lagrangian of QED

$$\mathcal{L} = \bar{\psi}\left(i\gamma^\mu \partial_\mu - m\right)\psi + e\bar{\psi}\gamma^\mu A_\mu \psi - \frac{1}{4}F_{\mu\nu}F^{\mu\nu} \,. \tag{2.4}$$

where γ^μ are Dirac matrices and e is the coupling constant. The last term was added for completeness. It corresponds to the kinetic energy of the gauge particle. As a term like $\frac{1}{2}m^2 A_\mu A^\mu$ is prohibited by gauge invariance, the gauge particle, in this case the photon, must be massless. To include weak processes in the formalism the procedure above has to be repeated using the SU(2) symmetry group. Formally the left-handed and right-handed particles introduced in section 2.1 can be distinguished by an additional quantum number referred to as the weak isospin. It is $I = \frac{1}{2}$ for the left-handed fermion doublets with the third component

$I_3 = \begin{cases} 1/2 & \text{for } \nu_l \\ -1/2, & \text{for } l^- \end{cases}$ and $I_3 = 0$ for the right handed singlets.

The weak isospin and the electric charge are linked to the weak hypercharge via the Gell-Mann-Nishijima relation

$$Q = I_3 + \frac{Y}{2} \tag{2.5}$$

The generation changing properties of the weak interactions can be explained by the assumption that the mass eigenstates do not exactly correspond to the flavour eigenstates. The Cabbibo-Kobayashi-Maskawa (CKM) matrix combines the two states by rotations of small angles that can only be obtained from measurements.

Especially the precise measurement of the matrix element V_{tb} is of particular interest as rare decays of the top quark related to physics beyond the Standard Model would lead to the violation of the measured 3×3 unitary constraints on V_{tb}.

The gauge transformation for the left-handed doublets L can be written as

$$L' = \exp\left(i\frac{g}{2}\vec{\tau}\cdot\vec{\beta}(x)\right) L \tag{2.6}$$

while the weak hypercharge transforms like the electric charge under U(1) for right R and left-handed L particles

$$L' = \exp\left(i\frac{g'}{2}Y\chi(x)\right) L \tag{2.7}$$

$$R' = \exp\left(i\frac{g'}{2}Y\chi(x)\right) R\,. \tag{2.8}$$

with the Pauli matrices $\vec{\tau}$ (see AppendixA), the coupling constants g and g' of the electromagnetic and weak force and space-time point dependent phase transformations $\vec{\beta}(x)$ and $\chi(x)$. To keep the Lagrangian invariant under that kind of transformation the gauge field for the weak hypercharge is introduced as in QED while the invariance under $SU(2)_L$ requires three vector fields W_i^μ (i=1,2,3). As before the derivative needs to be modified as well

$$D^\mu = \partial^\mu + ig\vec{T}\cdot\vec{W}^\mu + i\frac{g'}{2}YB^\mu \tag{2.9}$$

with $\vec{T} = \vec{\tau}/2$ for the left-handed and $\vec{T} = 0$ for the right-handed particles. The physical fields realized in nature can be obtained by using the notation of ladder operators for $\vec{\tau} \cdot \vec{W}^{\mu}$ such that

$$\vec{\tau} \cdot \vec{W}^{\mu} = \sqrt{2} \left(\tau_{+} W^{(-)\mu} + \tau_{-} W^{(+)\mu} \right) + \tau_3 W_3^{\mu} \tag{2.10}$$

and

$$D^{\mu} = \partial^{\mu} + i \frac{g}{\sqrt{2}} \left(\tau_{+} W^{(-)\mu} + \tau_{-} W^{(+)\mu} \right) + i \frac{g}{2} \tau_3 W_3^{\mu} - i \frac{g'}{2} B^{\mu}. \tag{2.11}$$

Now the charged W bosons introduced in section 2.1 can be directly extracted as

$$W^{(\pm)\mu} = \frac{1}{\sqrt{2}} \left(W_1^{\mu} \pm W_2^{\mu} \right) \qquad \longmapsto W^{\pm} \tag{2.12}$$

while the gauge field for the photon and Z boson are linear combinations of the fields W_3^{μ} and B^{μ}

$$A^{\mu} = B^{\mu} \cos\theta_W + W_3^{\mu} \sin\theta_W \qquad \longmapsto \gamma \tag{2.13}$$

$$Z^{\mu} = -B^{\mu} \sin\theta_W + W_3^{\mu} \cos\theta_W \qquad \longmapsto Z^0. \tag{2.14}$$

The mixing angle ${\theta_W}^2$ is related to the coupling constants g and g' as follows

$$\cos\theta_W = \frac{g}{\sqrt{g^2 + {g'}^2}} \quad , \sin\theta_W = \frac{g'}{\sqrt{g^2 + {g'}^2}} \tag{2.15}$$

and is measured to a value of $\sin^2\theta_W = 0.23122 \pm 0.000065$ [2].

2.2.2 The Higgs Mechanism

All considerations have so far been made for massless particles which disagrees with nature as especially the gauge bosons W and Z have high masses of 80.4 GeV and 91,2 GeV, respectively [2]. To generate particle masses in a gauge invariant way, the $SU(2) \otimes U(1)$ symmetry must be broken. The process of spontaneous symmetry breaking in the Standard Model is called the Higgs mechanism. It describes the coupling of all massive particles to the Higgs field, an omnipresent background field which can be introduced as a doublet of complex scalar fields [15]

$$\phi = \begin{pmatrix} \phi^{+} \\ \phi^{0} \end{pmatrix}. \tag{2.16}$$

That leads to a Lagrangian

$$\mathcal{L} = (D^{\mu}\phi)(D_{\mu}\phi) - V(\phi^{\dagger}, \phi). \tag{2.17}$$

The Higgs potential

$$V(\phi^{\dagger}, \phi) = -\mu^2 \phi^{\dagger}\phi + \lambda^2 (\phi^{\dagger}\phi)^2 \tag{2.18}$$

[2] also referred to as Weinberg angle

is invariant under $SU(2) \otimes U(1)$ transformations. To induce spontaneous symmetry breaking a minimum is obtained for non-vanishing ϕ values

$$\left|\phi^\dagger \phi\right| = \frac{\mu^2}{2\lambda^2} \equiv \frac{v}{\sqrt{2}}\,. \tag{2.19}$$

This minimum is called the vacuum expectation value. A possible choice could be

$$\phi_0 = \frac{1}{\sqrt{2}} \begin{pmatrix} 0 \\ v \end{pmatrix}\,. \tag{2.20}$$

Figure 2.1 shows that the zero-field configuration is unstable to small perturbations

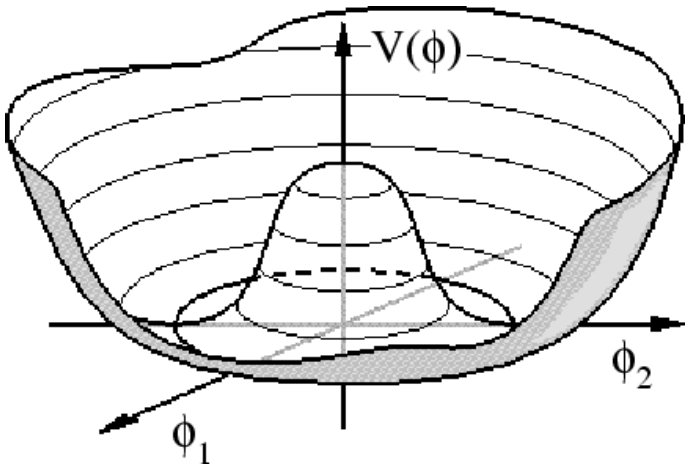

Figure 2.1: The "Mexican Hat" shape of the Higgs potential with a minimum for non-vanishing ϕ values.

and would "fall" into a lower energy state. This means that the natural state of space (the vacuum) is not empty, but is permeated by the Higgs field. By selecting one particular point in the moat around the local maximum at zero as vacuum state, the symmetry of the Higgs potential is broken.

A Taylor expansion around this minimum $v \rightarrow v + \eta(x)$, where η is small, inserted

in the Lagrangian gives the mass terms for the intermediate particles:

$$\begin{aligned}
\mathcal{L} = & \left[(\partial^\mu \eta)\,(\partial_\mu \eta) - 2\mu^2\eta^2\right] && \left\{ \begin{array}{l} \text{massive Higgs} \\ \text{with } m_H = \sqrt{2}\mu \end{array} \right. \\
& + \frac{1}{2}\cdot\frac{g^2v^2}{4}\left[\left|W_\mu^{(+)}\right|^2 + \left|W_\mu^{(-)}\right|^2\right] && \left\{ \begin{array}{l} \text{massive W bosons} \\ \text{with } m_W = \frac{gv}{2} \end{array} \right. \\
& + \frac{1}{2}\cdot\frac{g^2v^2}{4cos^2\theta_W\left|Z_\mu\right|^2} && \left\{ \begin{array}{l} \text{massive Z boson} \\ \text{with } m_Z = \frac{gv}{2cos\theta_W} \end{array} \right. \\
& - \left(G_1\bar{L}\phi R + G_2\bar{L}\phi_C R + \text{hermitian conjugate}\right) && \left\{ \begin{array}{l} \text{lepton and quark} \\ \text{masses and} \\ \text{couplings to Higgs} \end{array} \right.
\end{aligned} \tag{2.21}$$

As equation 2.21 does not include a term $\propto |A_\mu|^2$ the photon remains massless. The first term shows the Lagrangian of a free Higgs boson with mass $m_H = \sqrt{2}\mu$. The last term describes the coupling of the massive fermions to the Higgs boson. $\bar{L}$ denotes the left-handed fermion doublets, R the right-handed fermion singlet. While ϕ as introduced for the coupling to the heavy gauge bosons in equation 2.16 and equation 2.20 can be used to describe the coupling of the leptons to the Higgs field, the conjugated doublet is used to generate the quark masses in the same way

$$\phi_C = \begin{pmatrix} -\bar{\phi}^0 \\ \phi^- \end{pmatrix} \xrightarrow{breaking} \sqrt{\frac{1}{2}}\begin{pmatrix} v+\eta \\ 0 \end{pmatrix}. \tag{2.22}$$

G denotes the coupling to the Higgs field referred to as Yukawa-coupling

$$G_f = \frac{\sqrt{2}m_f}{v}\,. \tag{2.23}$$

It is proportional to the fermion masses which stresses the importance of the top quark for a possible Higgs boson discovery, as the top quark is the heaviest known particle and thus has the strongest coupling to the Higgs field. The Higgs boson itself is the only unmeasured particle within the Standard Model. Direct searches from LEP exclude a Higgs mass below $m_H < 114\,\text{GeV}$ at 95% CL as shown in figure 2.2. Precision measurements of the electroweak parameters as function of the Higgs mass lead to an upper bound of $m_H = 219\,\text{GeV}$ again at 95% CL [2].

2.2.3 Matrix element calculation using Feynman rules

Since the Lagrangian itself is not subject to experimental measurements, the link between the theoretical formulation and measurable quantities shall be briefly introduced for the basic process $e^+e^- \to \mu^+\mu^-$ via the exchange of a Z boson.

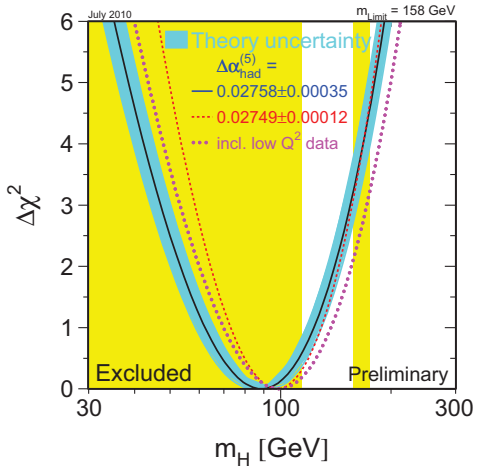

Figure 2.2: Global fit of electroweak data as a function of the Standard model Higgs mass [16]. The dashed line includes an updated value of the top mass. The yellow region was excluded by direct searches.

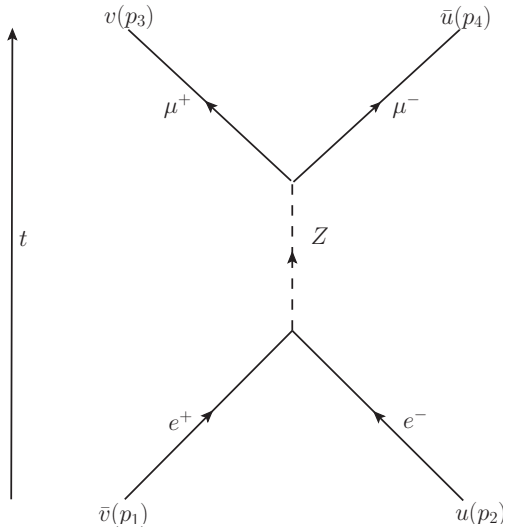

Figure 2.3: Feynman diagram for the process $e^+e^- \rightarrow Z \rightarrow \mu^+\mu^-$ via Z Boson exchange.

Figure 2.3 shows the Feynman diagram for the process in the s-channel. The cross section for this process is given by

$$d\sigma = \frac{|\mathcal{M}|^2}{F} dQ. \tag{2.24}$$

where F is the rate at which incident particles pass through and $|\mathcal{M}|^2$ is the matrix element which gives the transition rate derived from Fermi's Golden rule integrated over the phase space dQ. The matrix element can be formulated by following the

Feynman rules for the process under consideration which state that the matrix element is the product of the following factors:

- External lines: $u(\bar{u})$ for incoming(outgoing) particle; $v(\bar{v})$ for incoming(outgoing) antiparticle;
- Vertices: factor $-iQ_f e\gamma^\mu$ for photon, $-\frac{ig\gamma^\mu}{cos\theta_W}(g_V^f + g_A^f\gamma^5)$ for massive bosons
- Propagators: factor $\frac{-ig_{\mu\nu}}{q^2}$ for photons and $\frac{-ig_{\mu\nu}/M^2}{q^2-M^2}$ for bosons with mass M.

For the process in figure 2.3 applying the Feynman rules yields:

$$\begin{aligned} -i\mathcal{M} &= \bar{\nu}\frac{-ig\gamma^\mu}{cos\theta_W}(g_V + g_A\gamma^5)u\frac{-ig_{\mu\nu}/M^2}{(p_1+p_3)^2 - M^2}v\frac{-ig\gamma^\mu}{cos\theta_W}(g_V + g_A\gamma^5)\bar{u} \\ &= \frac{8G_F}{\sqrt{2}}\bar{\nu}\gamma^\mu(g_V + g_A\gamma^5)u\frac{ig_{\mu\nu}/M^2}{(p_1+p_3)^2 - M^2}v\gamma^\mu(g_V + g_A\gamma^5)\bar{u} \end{aligned} \tag{2.25}$$

where G_F is the Fermi constant which has been determined very precisely in measurements of the muon decay to $\frac{G_F}{(\hbar c)^3} = 1.16637(1) \times 10^{-5}\text{GeV}^{-2}$ [2]. To get the total cross section for $\sigma(e^+e^- \to Z \to \mu^+\mu^-)$ the matrix element has to be calculated for all possible helicities and integrated over the phase space and solid angle:

$$\sigma(e^+e^- \to Z \to \mu^+\mu^-) = \frac{1}{6\pi}\frac{G_F^2}{(s-M_Z^2)^2 + M_Z^2\Gamma_Z^2}\left[\left[(g_V^e)^2 + (g_A^e)^2\right]\left[(g_V^\mu)^2 + (g_A^\mu)^2\right]\right] \tag{2.26}$$

with the centre-of-mass energy s and the decay width of the Z boson $\Gamma(Z \to \mu^+\mu^-) = \frac{G_F M_Z^3}{6\pi}\left[(g_V^\mu)^2 + (g_A^\mu)^2\right]$. Hence, the total cross section is proportional to the sums of the squares of the vector- and axial-vector couplings of the initial and final state fermions.

2.2.4 QCD

The description of the strong force can be done in analogy to the previous section by replacing the used $SU(2) \otimes U(1)$ groups with the SU(3) group. To satisfy the requirement of local gauge invariance

$$q(x) \to e^{i\alpha_a(x)T_a}q(x) \qquad \text{with } a = 1,...,8 \tag{2.27}$$

this time eight gauge fields are needed. They can be identified with eight gluons. Since the gluons themselves carry colour charge, they can directly interact with each other. This consequence arises from the non-Abelian character of the SU(3) group which makes it necessary to add another term to the analogue expression in QED to keep the Lagrangian invariant

$$G_\mu^a \to G_\mu^a - \frac{1}{g}\partial_\mu\alpha_a - f_{abc}\alpha_b G_\mu^c\,. \tag{2.28}$$

Thus the final Lagrangian for QCD can be written as

$$\mathcal{L} = \underbrace{\bar{q}\left(\gamma^{\mu}\partial_{\mu} - m\right)q}_{\text{free quarks}} - \underbrace{g_S\left(\bar{q}\gamma^{\mu}T_a q\right)G^a_{\mu}}_{\text{gluon-quark interaction}} - \underbrace{\frac{1}{4}G^a_{\mu\nu}G^{\mu\nu}_a}_{\text{gluon self interaction}} \quad . \tag{2.29}$$

The effects of the self-interaction of gluons were already referred to in section 2.1 by discussing the screening effects in QED and the anti-screening in QCD respectively. The screening, due to higher order effects like photon or gluon radiation, is absorbed in the effective coupling. This procedure is known as renormalisation and turns the theory into a framework for quantitative calculations. Hence the coupling is no longer scale independent but increases with energy for QED and decreases for QCD, respectively.
A good understanding of the complex mechanisms in QCD is of great importance for the experiments at the LHC as the incoming particles in a collision are protons and thus a mixture of quarks and gluons. The existing theoretical descriptions of the proton structure, which base mainly on measurements from HERA and Tevatron, have to be extrapolated to the energies provided by the LHC. The theoretical uncertainties concerning this extrapolation give a non negligible contribution to most physics analysis performed at LHC.

2.3 Proton Proton Physics at the LHC

While the underlying theory behind QED as well as QCD can be elegantly formulated using the Lagrangian formalism, the verifiable predictions derived from the theory are usually formulated in terms of cross sections and branching ratios of the scattering processes under study. At high-energy hadron colliders two classes of scattering processes are distinguished:

- hard scattering, where rates and properties can be predicted with good precision using pertubation theory, e.g. for Higgs boson or high p_T jet production
- soft scattering, where total cross sections, the underlying event rates and properties are dominated by non-perturbative QCD effects which are less well understood [1].

Although the hard processes are usually considered the processes of interest a good understanding of the soft scattering is crucial as it often occur along with the hard interaction. Inelastic non-single diffractive events are often referred to as minimum bias[3] [17]. Minimum bias events give the largest contribution to the total cross section at high-energy hadron colliders as indicated in 2.4, where the cross sections of some important SM processes are compared to the total cross section.

[3]The definition of minimum bias events depend on the trigger of an experimental setup. In general, minimum bias events correspond to a totally inclusive trigger.

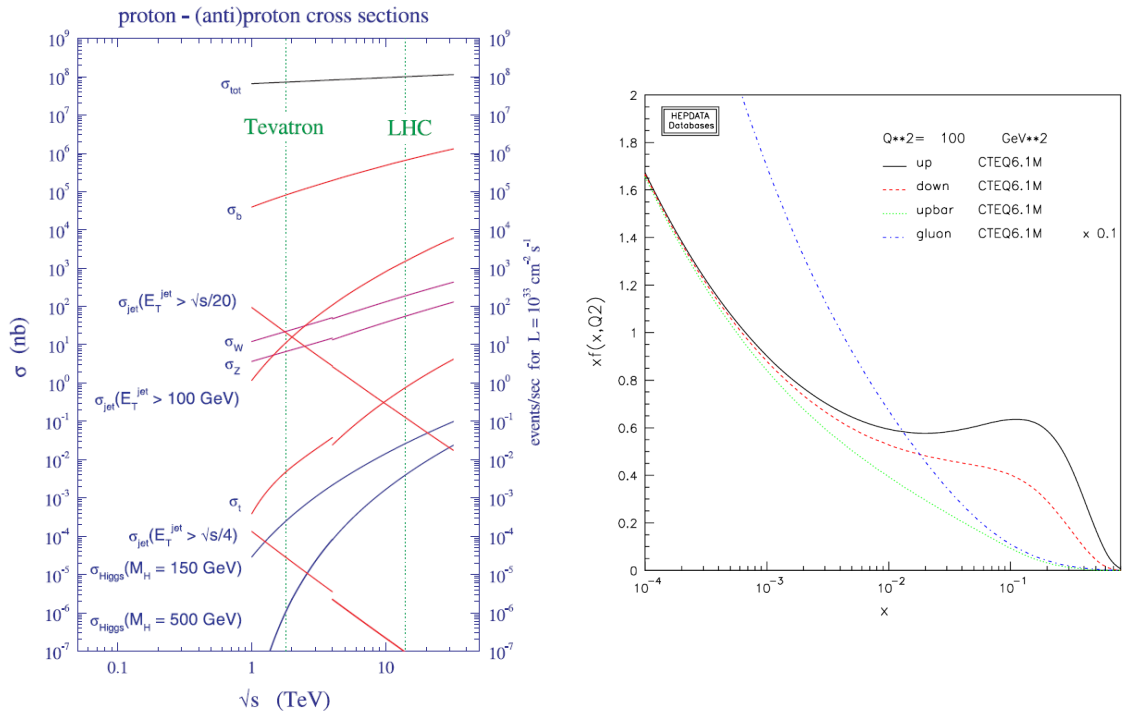

Figure 2.4: Cross sections as a function of the centre-of-mass energy at hadron colliders (left) and the parton distribution functions (right) [1].

To calculate the cross sections of proton proton collisions Drell and Yan suggested to convolute the cross section of the fundamental process, e.g. quark-antiquark annihilation $q\bar{q} \to X$, with the parton distribution functions (pdfs) which provide a parametrisation of the partonic content of the proton extracted from experimental measurements [18]. To obtain the cross section for quark-antiquark annihilation to a lepton pair via an intermediate Z boson, the fundamental cross section σ_{QED} calculated in section 2.2.3 is taken, adding the appropriate colour factors N and charge factors and Q_q:

$$\sigma(q\bar{q} \to Z \to \mu^+\mu^-) = \sigma_{QED}\frac{1}{N}Q_q^2 \tag{2.30}$$

Since the incoming quarks cover a broad spectrum of centre-of-mass energies $\sqrt{s}$, it is more appropriate to consider the differential cross section [1]:

$$\frac{d\sigma}{dM^2} = \frac{d\sigma'_{QED}}{M^2 N}Q_q^2\delta(\hat{s} - M^2) \tag{2.31}$$

where M is the mass of the produced fermion pair. Expressing the momenta of the incoming partons in their centre-of-mass framework $p_1^\mu = \frac{\sqrt{s}}{2}(x_1, 0, 0, x_1)$ and $p_2^\mu = \frac{\sqrt{s}}{2}(x_2, 0, 0, -x_2)$ and folding in the pdfs for the initial state quarks and antiquarks

results in:

$$\frac{d\sigma}{dM^2} = \frac{d\sigma'_{QED}}{M^2 N} \int_0^1 dx_1 dx_2 \delta(x_1 x_2 s - M^2) \times \left[\sum_k Q_k^2 \left(q_k(x_1, M^2) \bar{q}_k(x_2, M^2) + [1 \leftrightarrow 2] \right) \right] \tag{2.32}$$

with $\sqrt{\hat{s}} = x_1 x_2 s$ relating the partonic centre-of-mass energy to the one of the hadronic system. The rapidity y of the outgoing fermions can be expressed as $y = 1/2 \log(x_1/x_2)$ such that $x_1(2) = \frac{M}{\sqrt{s}} e^{(-)y}$ and the double differential cross section yields:

$$\frac{d\sigma}{dM^2 dy} = \frac{d\sigma'_{QED}}{M^2 N s} \left[\sum_k Q_k^2 \left(q_k(x_1, M^2) \bar{q}_k(x_2, M^2) + [1 \leftrightarrow 2] \right) \right] \tag{2.33}$$

Different values of M and y probe different values of the parton x of the colliding hadrons [1]. For a factorisation scale equal to the final state mass M, figure 2.5 shows the kinematics appropriate for the production of a particle with mass M and the rapidity y for the LHC in comparison to HERA or fixed target experiments. To produce a particle with mass M=100 GeV and rapidity y=2 requires 2 partons of x values around 0.05 and Q^2 values of roughly $10^4\,\mathrm{GeV}^2$.

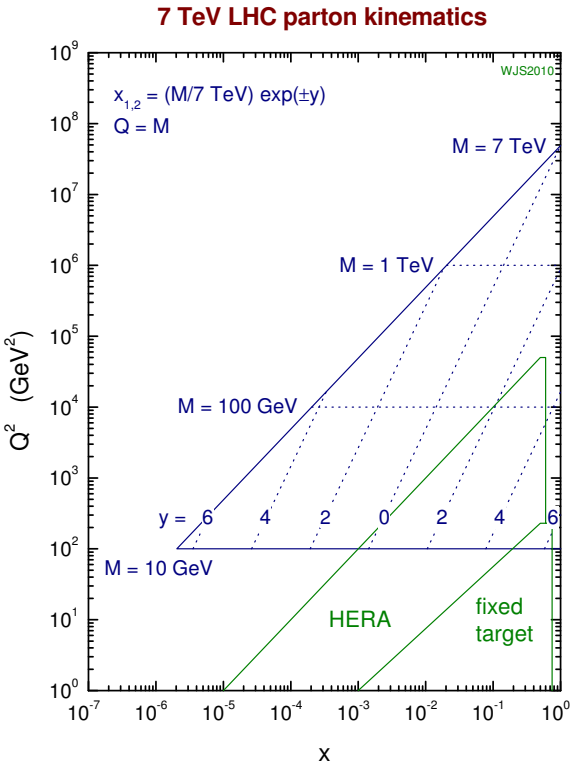

Figure 2.5: Graphical representation of connection between parton variables (x,Q^2) and the mass M and rapidity y of a particle in the final state for different high energy experiments [1].

2.4 Particle Interactions with Matter

To measure the fundamental quantities of the particles described in section 2.1 the particles or their decay products (depending on the life time) are forced to interact with matter in order to quantify the energy a particle is carrying or to measure its momentum. While calorimeters entirely absorb and hence destroy the incident particles to measure their energy, tracking devices are less invasive and all interactions influencing the particle's momentum are tried to be kept to a minimum [19]. Charged particles traversing matter mainly undergo electromagnetic interactions. For heavy charged particles, meaning particles with mass significantly larger than the electron mass $M >> m_e$, inelastic scattering with the atomic electrons dominates the overall energy loss during the passage through matter. The energy transferred from the particle to the atom in these collisions leads to an excitation or even an ionisation of the atom and although the amount of energy transferred in each collisions is rather small compared to the kinetic energy of the incident particle, the large number of collisions in dense matter accumulates to a substantial energy loss even in thin layers of material [19]. For electrons another process contributes to the overall energy loss, the emission of electromagnetic radiation arising from the interaction with the electric field of the nuclei, referred to as bremsstrahlung. The emission probability is proportional to the inverse square of the particle's mass and thus negligible for muons up to an energy of about 1 TeV while for electrons of a few 10's of MeV the contribution to the total energy loss is comparable or even greater than the one from collisions [19].

Another important interaction that particles undergo on their passage through matter is the elastic scattering off the nuclei. Although it does not contribute significantly to the overall energy loss, it causes a change of the flight direction of the incident particle. For spin-less point-like particles the effect was first described by Rutherford in 1906.

2.4.1 Inelastic scattering

The cross section for the inelastic scattering of a muon and an atomic electron can be derived using the formalism of Feynman diagrams. Figure 2.6 shows the diagram for an electron and exchanging a photon with a muon, where p and k denote the momenta of the incoming particles p' and k' the ones of the outgoing particles. The relative energy loss of the muons can be written like:

$$y = \frac{q \cdot k}{p \cdot k} = \frac{E - E'}{E} \tag{2.34}$$

where E' is the energy of the muons after the scattering process. The total energy ΔE lost on the path Δx is given then:

$$\Delta E = \bar{y} E \tag{2.35}$$

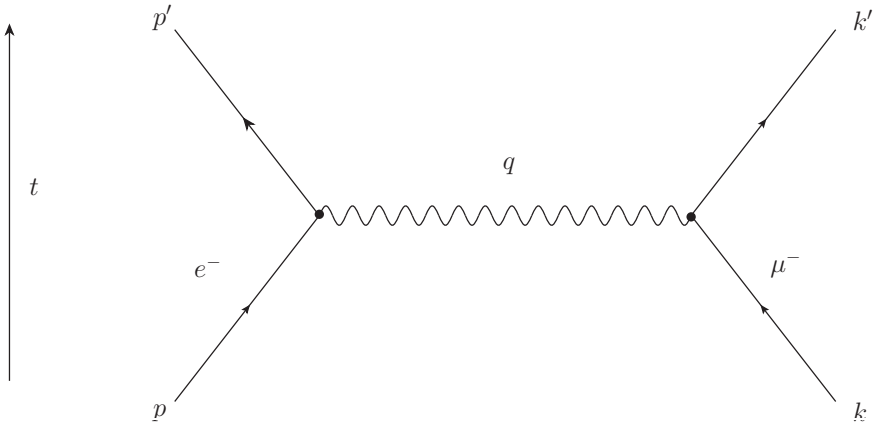

Figure 2.6: Feybnman diagram for electron muon scattering in Born approximation.

with $\bar{y}$ being the average relative energy loss derived from:

$$\bar{y} = n_0 Z \Delta x \int_{y_{min}}^{y_max} y \frac{d\sigma}{dy} dy \tag{2.36}$$

where $n_0 Z$ is the density of electrons in the medium with atomic number Z. The cross section $\frac{d\sigma}{dy}$ for the process taking into account the particle masses following the Feynman rules is given by:

$$\frac{d\sigma}{dy} = \frac{4\pi\alpha^2}{s_0 y^2} \frac{1}{1 - 4m^2M^2/s_0^2} \left(1 - y\frac{s}{s_0} - \frac{y^2}{2}\right). \tag{2.37}$$

with $s_0 = s - m^2 - M^2 = 2Em + m^2 + M^2$ considering the atomic electrons at rest. The maximal energy transferred in such a collision y_{max} is reached for a central collision at 180°:

$$y_{max} = \beta^2 \frac{s_0}{s} \tag{2.38}$$

such that equation 2.37 becomes:

$$\frac{d\sigma}{dy} = \frac{2\pi\alpha^2}{Em\beta^2 y^2} \left(1 - y\frac{\beta^2}{y_{max} + \frac{y^2}{2}}\right) \tag{2.39}$$

Neglecting the term $\frac{y^2}{2}$, integration over the whole energy range leads to [20]:

$$\bar{y} = n_0 Z \Delta x \frac{2\pi\alpha^2}{\beta^2 Em} \left(ln\frac{y_{max}}{y_{min}} - \beta^2\right) \tag{2.40}$$

which then also describes the average electromagnetic energy loss of spin-less particles like pions.

2.4.2 Bremsstrahlung

Every charged particle that is accelerated, for example in the electric field of a nuclei, radiates a certain amount of energy in form of bremsstrahlung. The emission probability is proportional to the inverse square of the particle's mass such that it is much stronger for light particles like the electron but does not effect a muon below an energy of 1 TeV [19]. Bremsstrahlung is an effect of higher order in perturbation theory. The corresponding Feynman diagrams for initial or final state radiation of the electron, neglecting the radiation on the muon side are shown in figure 2.7.

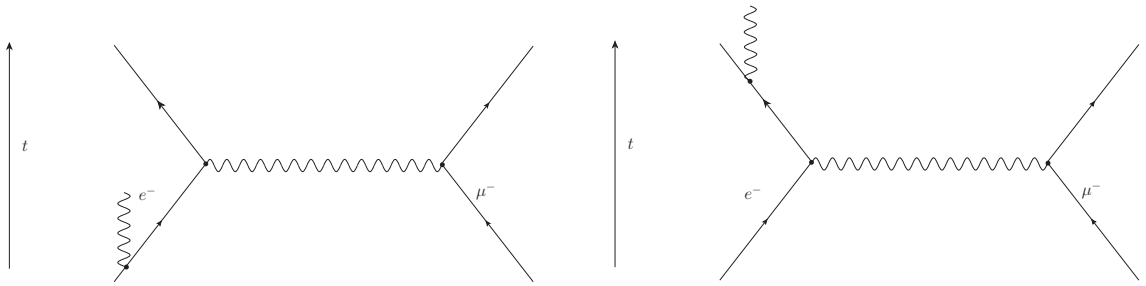

Figure 2.7: Initial (left) and final (right) state radiation of electron.

Defining y equivalent to the expression used for the inelastic scattering in the previous section:

$$y = \frac{q \cdot P}{p \cdot P} \tag{2.41}$$

the differential cross section can be written as

$$\frac{d\sigma}{dy} = \frac{4\alpha^3}{m^2 y}\left(1 + (1-y)62 - \frac{2}{3}(1-y)\right)\left(ln\frac{s_0(1-y)}{Mmy} - \frac{1}{2}\right) \tag{2.42}$$

In the case of radiation loss due to the Coulomb force from atoms with atomic number Z, a slight modification is necessary to account for the screening effect of the atomic electrons for small values of the transferred energy $\omega' = E' - E$:

$$\frac{d\sigma}{d\omega} = \frac{4Z^2\alpha^3}{m^2 w'}\left(1 - \frac{2E'}{3E} + \frac{E'^2}{E^2}\right) ln\frac{192}{Z^{1/3}} \tag{2.43}$$

To calculate the energy loss due to bremsstrahlung the differential cross-section times the photon energy is integrated over the allowed energy range:

$$\Delta E = -n_0 \Delta x \int_0^E \omega' \frac{d\sigma}{d\omega'} d\omega' \tag{2.44}$$

Whereas the energy loss transferred in collisions depends logarithmically on the energy and linearly on Z, the radiation loss increases almost linearly with the energy and quadratically with Z, leading to a rapid rise of radiation losses for high energies.

2.4.3 Bethe-Bloch formula

The average energy loss due to inelastic scattering as derived in section 2.4.1 is only valid down to a minimal energy loss y_{min} that is still large compared to the ionisation energy of the atomic electrons. Therefore, equation 2.40 has to be extended by including ionisation effects at the low energy regime as well as some correction from bremsstrahlung at the high energy regime. The resulting mean rate of energy lost in materials with intermediate atomic number Z in an interval $0.1 \lesssim \beta\gamma \lesssim 1000$ is described within a few % by the Bethe-Bloch equation [2]:

$$-\left\{\frac{dE}{dx}\right\} = Kz^2\frac{Z}{A}\frac{1}{\beta^2}\left[\frac{1}{2}ln\frac{2m_ec^2\beta^2\gamma^2T_{max}}{I^2} - \beta^2 - \frac{\delta(\beta\gamma)}{2}\right] \tag{2.45}$$

with constant $K = 4\pi N_A r_e^2 m_e c^2$, N_A being the Avocardo's number, m_e the electron mass, Z the atomic number of absorber, A atomic mass of absorber, $\beta = \frac{v}{c}$ is the velocity in terms of the speed of light, $\gamma = \frac{1}{\sqrt{1-\beta^2}}$, T_{max} the kinetic energy that can be imparted to a free electron in a single collision and I the mean excitation energy in electron volts. $\delta(\beta\gamma)$ accounts for the density corrections at high energies, when the particle polarises the atoms along its path and those electrons far from the path get shielded from the full electric field intensity, such that collisions with these electrons contribute less to the total energy loss. For low energies the assumption of a stationary atomic electron is no longer valid and a shell correction C/Z are necessary to account for atomic binding. Both correction terms depend on the absorbing material listed in detail in [2]. The distribution is shown in figure 2.8 for a muon traversing copper.

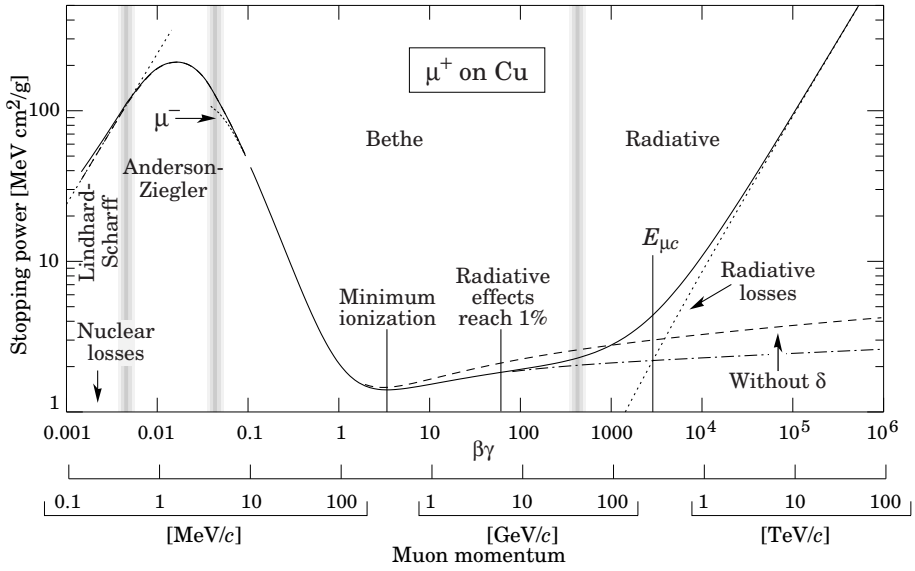

Figure 2.8: Energy loss for a muon in copper [2].

2.4.4 Rutherford scattering

If a charged particle traverses matter it undergoes deflection of its original path by elastic scattering off the electrons or the nuclei. Assuming its mass to be much smaller than the target mass, the latter can be considered at rest and the effective mass is approximately the one of the incoming particle. The classical differential cross section for this scattering process can be derived solving the equation of motion for a particle interacting with a central potential, referred to as *Rutherford formula*:

$$\frac{d\sigma_R}{d\Omega} = \frac{1}{4} q_1^2 q_2^2 \left(\frac{e^2}{Pv}\right)^2 \frac{1}{sin^4(\Theta/2)}. \tag{2.46}$$

It describes the probability of finding the particle deflected by the angle Θ in the solid angle $d\Omega = 2\pi\Theta d\Theta$, with q_1 and q_2 being the charges of the target and the projectile, respectively.

2.5 Muons originating from Cosmic Rays

The processes observed by collider experiments, built to study the particles of the standard model and their fundamental interactions in a laboratory, continuously take place when cosmic radiation penetrates the top level of the terrestrial atmosphere. Cosmic radiation consists of all stable particles and nuclei with lifetimes exceeding 10^6 years or longer. Electrons, protons, helium as well as carbon, oxygen, iron and other nuclei synthesized in stars are considered primaries, whereas heavier nuclei like lithium, beryllium and boron are produced in interactions of the primaries with interstellar gas and thus are referred to as secondaries [2]. The energy spectrum of the cosmic radiation covers several orders of magnitude up to ranges far beyond the scope of terrestrial collider experiments. Figure 2.9 shows the flux of cosmic rays as a function of the energy.

The majority of the primary nuclei are free protons, about 79%. When hitting the outermost atmosphere of the earth they interact hadronically with atmospheric nuclei and produce secondary particles, mainly pions (π^0, π^+,π^-) as well as less abundantly kaons and other mesons. Depending on their lifetime, energy and incident angle of these secondary particles interact further with atmospheric nuclei or they decay via the electroweak interaction. The neutral pions decay almost instantly into two photons, while the charged pions decay via the process [22]:

$$\begin{aligned} \pi^+ &\rightarrow \mu^+ + \nu_\mu \\ \pi^- &\rightarrow \mu^- + \bar{\nu}_\mu \end{aligned} \tag{2.47}$$

Although produced rather high in the atmosphere at about 15 km, most of the muons survive down to sea level, as their life time of approximately $2.2 \cdot 10^{-6}$ s is prolonged by time dilatition. The mean energy of muons at the ground is $\approx$4 GeV [2]. The

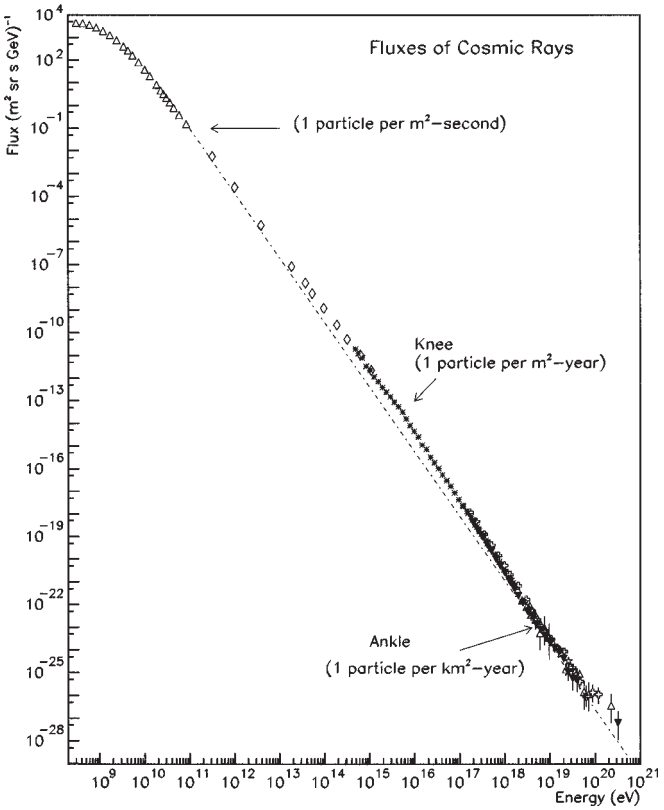

Figure 2.9: The flux of cosmic rays as function of the incident particles energy follows a power law almost entirely proportional to E^{-3} with two small deviations at 10^{15} and 10^{18} GeV referred to as *knee* and *ankle* [21].

higher number of protons over neutrons in the primary cosmic radiation and an excess of $\pi^+(K^+)$ over $\pi^-(K^-)$ in the forward fragmentation region of proton initiated interactions lead to a muon charge ratio $\mu^+/\mu^- > 1$ [2].

Chapter 3

The CMS experiment at the Large Hadron Collider

The Large Hadron Collider (LHC) was built to elucidate physics at the TeV scale to test the consistency of the Standard Model at high energies, to study the nature of electroweak symmetry breaking with a possible discovery of the Higgs boson as discussed in section 2.2.2 and to provide the opportunity for discoveries of physics beyond the Standard Model – such as supersymmetry or extra dimensions. In addition to the proton proton collisions necessary to study new physics at high energies, the physics programme of the LHC also incorporates heavy ion collisions to yield a deeper understanding of QCD under extreme conditions of temperature, density and parton momentum fraction. After a period of careful commissioning runs at the end of 2009 and beginning of 2010, the LHC has been providing collision data at a centre-of-mass energy of 7 TeV for physics analysis since March 2010. Due to an incident which delayed the LHC's beginning operations, the experiments started to commission their detectors using muons produced in the atmosphere from cosmic rays. These commissioning exercises already allowed a complete calibration and alignment of the detectors installed at the intersection points and are the basis for the excellent detector performance at the startup of the physics programme.
In the following section the LHC and its commissioning will be briefly described before the Compact Muon Solenoid (CMS) detector will be presented with a focus on the inner tracking detectors.

3.1 LHC

The LHC is contained in the old LEP[1] tunnel at CERN, which is 27 km in circumference. The design centre-of-mass energy for proton-proton collisions is 14 TeV with a luminosity of $L = 10^{34}\, cm^{-2} s^{-1}$. In order to keep the high energy proton beams at the given circumference, 1332 superconducting dipole magnets provide a magnetic

[1] **L**arge **E**lectron **P**ositron Collider operated by CERN from 1989-2000.

field of 8.4 T [23]. To ensure the secure operation of the machine, several protection systems were installed to monitor the circulating beams and the stability of the superconducting magnets. After a technical incident shortly after the first commissioning of the LHC in September 2008, it was decided to operate the collider at a centre-of-mass energy of 7TeV until a further upgrade of the quench protection system for the dipole magnets will be installed, which is foreseen to occur during a major shutdown in 2013 [24]. From March until October 2010 the LHC was operated with two proton beams. Before being injected and accelerated in the LHC the proton bunches are formed in the 26 GeV Proton Synchrotron (PS) and accelerated to 450 GeV in the Super Proton Synchrotron (SPS), after which they are injected to the LHC where they are ramped up to the final energy. During operation in 2010 the number of total bunches was subsequently increased and the bunch spacing was reduced so that at the end of the 2010 physics programme a luminosity of $L = 10^{32}\, cm^{-2}s^{-1}$ was reached. The total integrated luminosity provided by LHC during 2010 is shown in fig 3.1. About 90-95% of the collision events could be successfully recorded by the experiments.

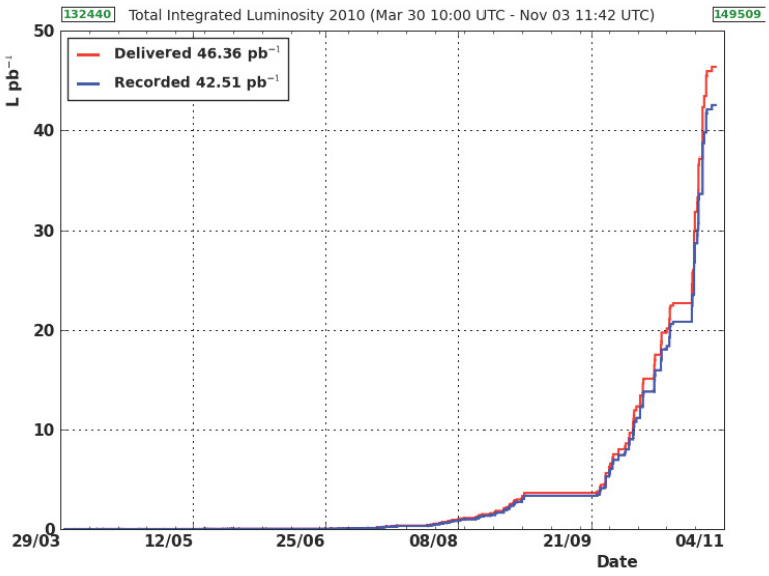

Figure 3.1: Delivered (red) and recorded (blue) luminosity of LHC over the 2010 run period[25].

In November and December 2010 LHC switched from proton to lead ion collisions at a centre of mass of 2.76 TeV per nucleon pair, and after a short period of adjusting the machines about $8.4\,\mu b^{-1}$ of integrated luminosity could be delivered during one month of running.

Figure 3.2 shows the four major detectors hosted at four intersection points of the

LHC. While ALICE[2] is dedicated to heavy ion collisions [26], LHC-b is designed to study CP-violation in B meson decays [27]. The large multipurpose detectors ATLAS[3] [28] and CMS are both accompanied by small detectors at some distance apart. They are supposed to measure the total proton-proton cross section and thus help to define the luminosity provided by the LHC as well as to study the physics of particles generated in the high η region. Therefore, the LHC-f[4] experiment consists of two detectors, 140 m on either side of the intersection point of the ATLAS experiment [29]. The TOTEM[5] detector consists of several modules which are up to 220 m away from the CMS detector [30]. The multipurpose detectors CMS and ATLAS are both designed for new discoveries of physics beyond the Standard Model, as well as for precision measurements of Standard Model processes. In the following section only the CMS detector will be described [3].

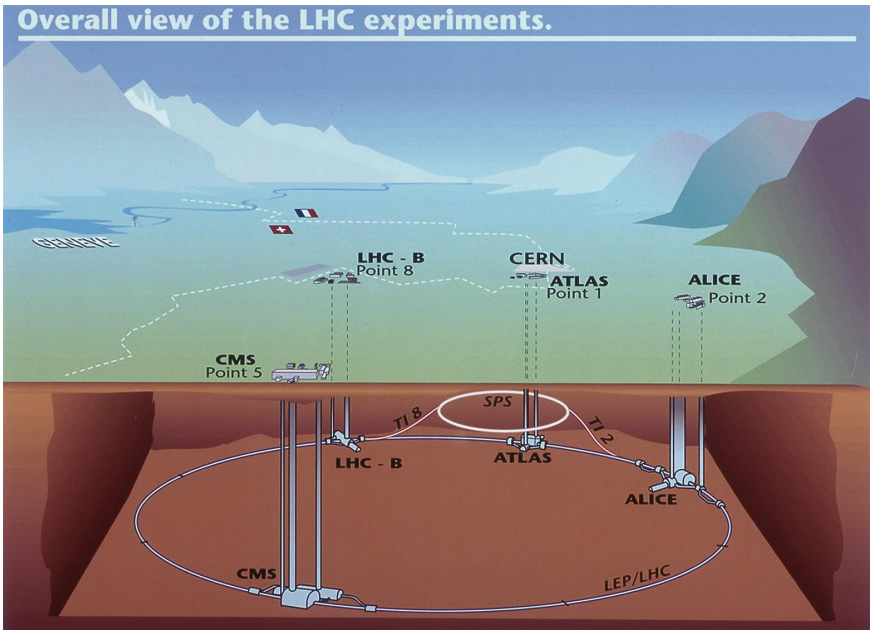

Figure 3.2: Overview of the LHC collider with the four large experiments, ALICE, ATLAS, CMS, and LHC-b. In addition, two smaller experiments are installed, TOTEM at the CMS interaction point 5 and LHC-f near the ATLAS detector [31].

3.2 CMS Detector

The design specifications of the LHC are not only a challenge by themselves, they also imply high technical requirements for the detectors used to analyse the data

[2] **A** **L**arge **I**on **C**ollider **E**xperiment
[3] **A** **T**oroidal **L**HC **A**pparatu**S**
[4] LHC- forward
[5] **TOT**otal**E**lastic and diffractive cross section **M**easurement

from collisions emerging every 25 ns. At the design luminosity, one event of interest is expected to be superimposed by about 20 inelastic collisions, resulting in around 100 charged particles coming from the interaction region. This so called pile-up can be counteracted by high-granularity detectors with good time resolution and thus low occupancy. However, a high granularity requires a very good synchronisation of the resulting millions of read-out channels.

In addition to the capability of detecting all the produced particles, their high flux implies that the detector material and read-out electronics must be radiation-hard. The requirements arising from the LHC physics programme can be outlined as follows [3]:

- Dimuon, dielectron and diphoton mass resolution of about 1% at 100 GeV
- Unambiguous determination of the charge of muons with momenta p > 1TeV
- A precise measurement of charged particle momenta and high reconstruction efficiencies in the innermost tracking system, to allow triggering and tagging of particles from secondary vertices, such as τ-leptons and b-jets
- Good missing transverse-energy E_t^{miss} and dijet resolution implying the highest possible hermetic geometric coverage of the hadron calorimeters

The key component of the CMS detector design is the 4 T superconducting solenoid of 13 m length and a diameter of 5.9 m. As shown in figure 3.3 its bore coil is large enough to accommodate the tracker as well as the calorimetry inside. With 2168 Ampere-turns, a current of 19.5 kA and a stored energy of 2.7 GJ it provides a bending power of 12 Tm. The return field saturates 1.5 m of iron in which four muon stations are integrated, constituting the outermost detector component.

In total the CMS detector has a weight of 12 500 t, a length of 21.5 m and a diameter of 15 m. The individual detector layers will be presented in the following sections, which will focus on the inner most tracking system. A complete and detailed detector description can be found in [3].

3.2.1 CMS coordinate system

The coordinate system chosen to describe processes measured in the different detector layers has its origin at the nominal collision point. The z-axis points along the beam pipe, while the x- and y-axes build a plane orthogonal to the z-axis, with y pointing vertically upwards and x pointing towards the centre of the collider. In that plane the azimuthal angle is measured with respect to the x-axis. The polar angle θ is measured from the z-axis but often replaced by the pseudo-rapidity which is defined as

$$\eta = -ln\, tan\frac{\theta}{2}\,. \tag{3.1}$$

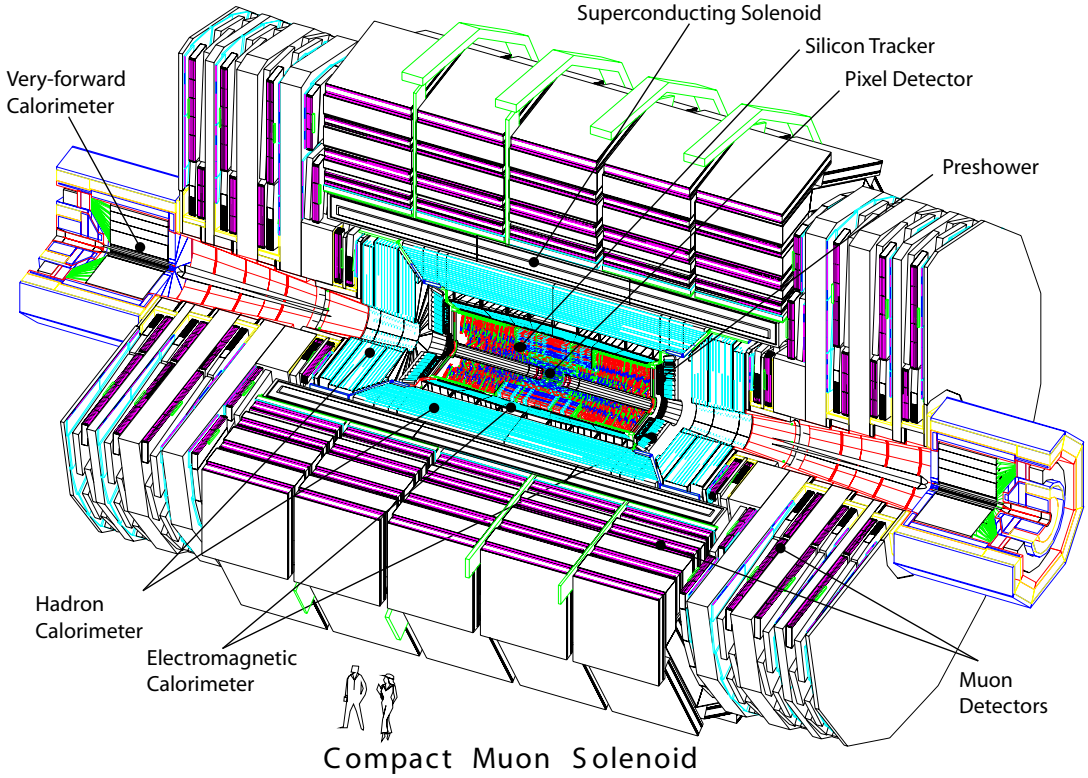

Figure 3.3: The CMS detector layout [3]

The difference in the pseudo-rapidity of two massless particles $\Delta\eta$ as well as of the azimuthal angle $\Delta\phi$ are independent of Lorentz boosts along the beam axis. The distance of two particles is often measured in terms of

$$\Delta R = \sqrt{(\Delta\eta)^2 + (\Delta\theta)^2}\,. \tag{3.2}$$

3.2.2 The CMS tracking detector

The innermost detector of CMS is the tracking system which consists of a silicon pixel detector surrounded by a silicon micro-strip detector. The design of the CMS tracker is the result of an optimisation process providing the necessary granularity and fast response by retaining the material budget as low as possible, to keep multiple scattering, bremsstrahlung, photon conversion and nuclear interactions to a minimum.

3.2.2.1 The silicon pixel detector

The pixel detector consists of three layers of silicon modules in the barrel and two discs in each forward direction. The barrel is 53 cm long and the layers are located at 4.4, 7.3 and 10.2 cm from the nominal beamline to enable the optimal reconstruction of primary and, especially, secondary vertices. The first layer and the second disc cover

a $|\eta|$-range of 2.5, matching the acceptance of the central tracker. Besides the precise measurement of tracking quantities important for the physics programme, the choice of a pixel detector as innermost device is also driven by the operating conditions. At LHC design luminosity the hit rate density is $1\,\mathrm{MHz}/mm^2$ at a radius of 4 cm. To keep the occupancy at about 1%, pixel detectors are necessary below a radius of 10 cm. According to the desired impact parameter resolution, the pixel size was chosen to be $100\,\mathrm{x}\,150\ \mu m^2$ in rΦ and z, respectively, resulting in an occupancy of 10^{-4} per pixel and LHC bunch crossing. For the modules in the barrel pixel the drift direction of the electrons to the collecting pixel is orthogonal to the homogeneous 3.8 T magnetic field. Due to the emerging Lorentz drift the collected signal charge is spread over more than one pixel. Charge interpolation using the analogue pulse read-out allows a spatial resolution of 15-20 μm [3], which could be further improved by using template fits for the hit reconstruction [32]. To induce charge-sharing also in the endcaps, the forward detectors are tilted by 20° in a turbine-like geometry.

As a consequence of the high radiation doses the innermost layer of the pixel will collect during LHC operations, the mechanics and cabling of the pixel system have been designed in order to allow easy access for necessary replacements. The pixel modules are mounted on cylindrical support structures as shown in figure 3.4. They are split vertically for installation in the presence of the beam pipe. In total, a number of 1440 pixel modules are installed, leading to about 65 million read-out channels. Although each pixel only generates around 50 μW, the total power output would overheat the detector; therefore, the pixels are mounted on cooling tubes, which are able to cool down the pixel detector to an operating temperature of $-10°$ C using C_6F_{14}. Due to the lower luminosity provided by LHC during operations in 2010 the pixel was operated at higher temperatures [33].

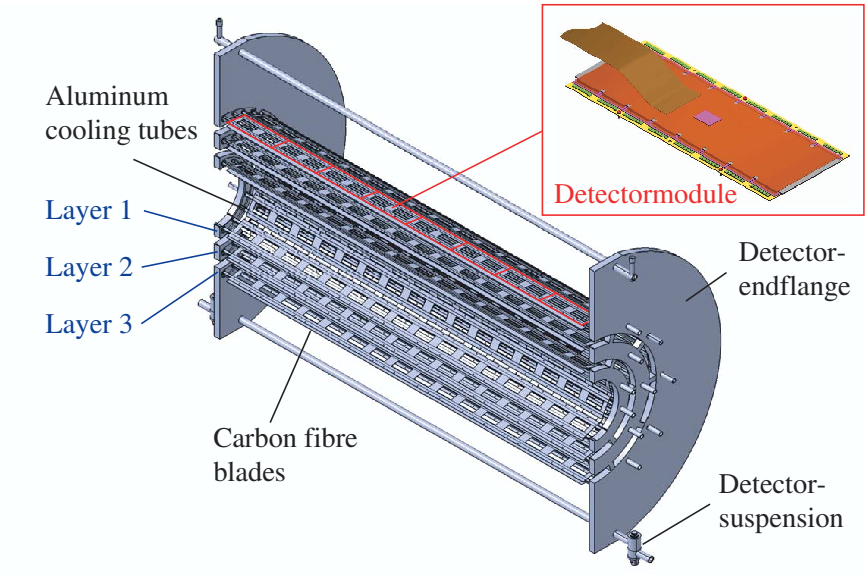

Figure 3.4: Halfshell of a pixel support structure.

3.2.2.2 The silicon strip tracker

With increased distance from the interaction point, the reduced particle flux allows the use of silicon micro-strip detectors. For the intermediate radii ($20\,\text{cm} < \text{r} < 55\,\text{cm}$) – the tracker inner barrel (TIB) and tracker inner discs (TID) in forward direction – the silicon micro-strip sensors are $320\,\mu$m thick, with the strips parallel to the beampipe in the barrel and radial on the endcaps. The TIB consists of 4 layers, each of them subdivided into four sub-assemblies ($\pm z$, up/down) for ease of handling and integration. The strip pitch varies between $80\,\mu$m in layer 1 and 2 and $120\,\mu$m on layer 3 and 4 in TIB allowing a single point resolution of $23\,\mu$m and $35\,\mu$m , respectively. Each TID is an assembly of three discs placed between ± 70 and $\pm 100\,\text{cm}$, each consisting of 3 rings. The strip pitch varies from $100\,\mu$m to $141\,\mu m$. Together TIB and TID cover a range in pseudo-rapidity up to 2.5 [[3], p.65].
In radial direction the TIB and TID are enclosed by the Tracker Outer Barrel (TOB) which is made of $500\,\mu$m thick micro-strip sensors, grouped in six layers with an outermost radius of 116 cm. For the inner four layers the strip pitch is $183\,\mu$m, layers 5 and 6 have sensors with a strip pitch of $122\,\mu$m. The resulting single point resolution is $53\,\mu$m and $35\,\mu m$, respectively. While in the TIB and the TID each tracker module is equipped with one silicon sensor, in the TOB the modules carry two sensors whose strips are electrically connected [[3], p.62].
In the TOB six to twelve modules are mounted to supporting structures referred to as rods. Two rods cover the complete length of the TOB in z. The mechanical support structure of the TOB is a 2.18 m long cylinder composed of four identical discs joined by three inner and three outer cylinders, supporting 688 rods. The design of the rod mechanics is chosen in such a way that the neighbouring rods, and thus the sensors on them, overlap in the rϕ-plane to provide two consecutive hit measurements with almost no material budget in between [[3], p.67]. The plain cylinder mechanics has been thoroughly measured via photogrammetry, theodolites, and 3D coordinate measurement systems and the relative positioning of the precision elements has been found to be within $100\,\mu$m of the nominal values, with maximum deviations observed around $200\,\mu$m [[3], p.68]. These survey measurements have been performed for all subdetectors and provide a reference geometry of the large detector structures for later precision alignments.

The tracker is extended to both sides by the Tracker Endcaps (TEC), covering the region between $124\,\text{cm} < |\,\text{z}\,| < 282\,\text{cm}$ and $22.5\,\text{cm} < \text{r} < 113.5\,\text{cm}$. Each endcap is subdivided into 9 discs, each carrying up to 7 rings of silicon micro-strip detectors. The three outermost rings are equipped with $500\,\mu$m thick sensors, while for the inner 4 rings the thin sensors of $320\,\mu$m are used. The average pitch of the radial strips varies between $97\,\mu$m and $184\,\mu$m, depending on the module shape and type. The thick modules in the TEC are also equipped with two sensors per module. Figure 3.5 shows the different geometries and shapes of the CMS tracker strip modules.
The sensitive coordinate of the micro-strip sensors is the one orthogonal to the strips, which translates into global rϕ for the sensors in the barrel and ϕ for the sensors in the endcaps. To provide a handle also on the coordinate parallel to the srips, z in

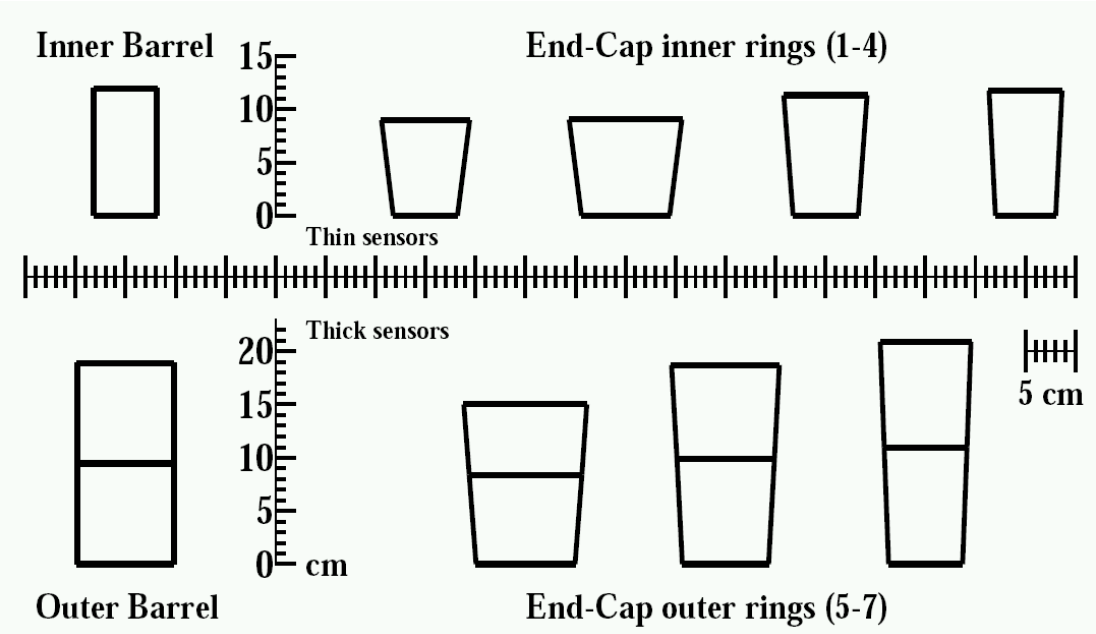

Figure 3.5: Silicon strip modules in different geometries and sizes.

the barrel and r in the endcaps, the first two layers and rings, respectively, of the TIB, TID and TOB as well as the rings 1,2 and 5 of the TECs are equipped with a second micro-strip sensor which is mounted back-to-back to the regular modules with a stereo angle of 100 mrad (see figure 3.6).

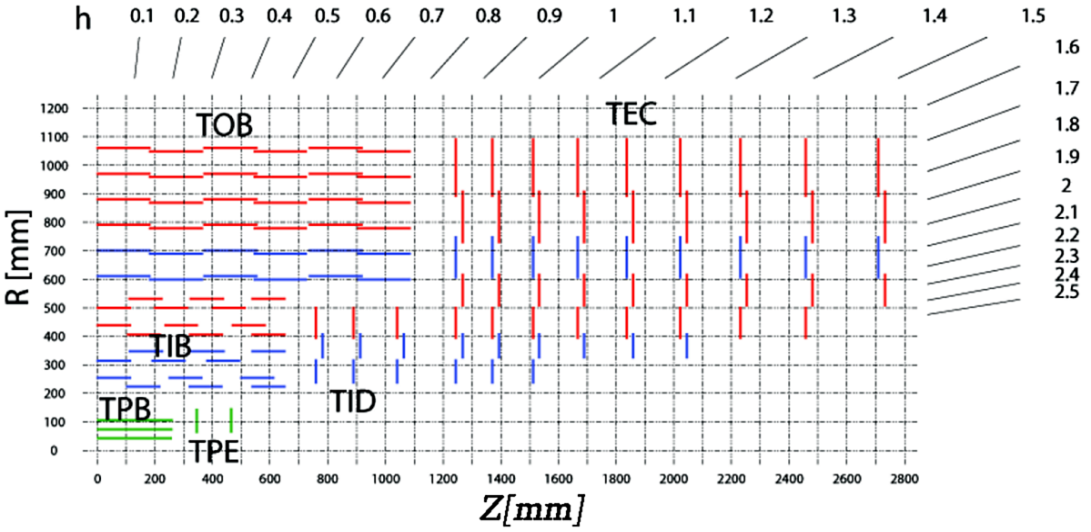

Figure 3.6: Sketch of the CMS strip tracker, highlighting the layers equipped with 1d-modules (blue) and 2d-modules (red).

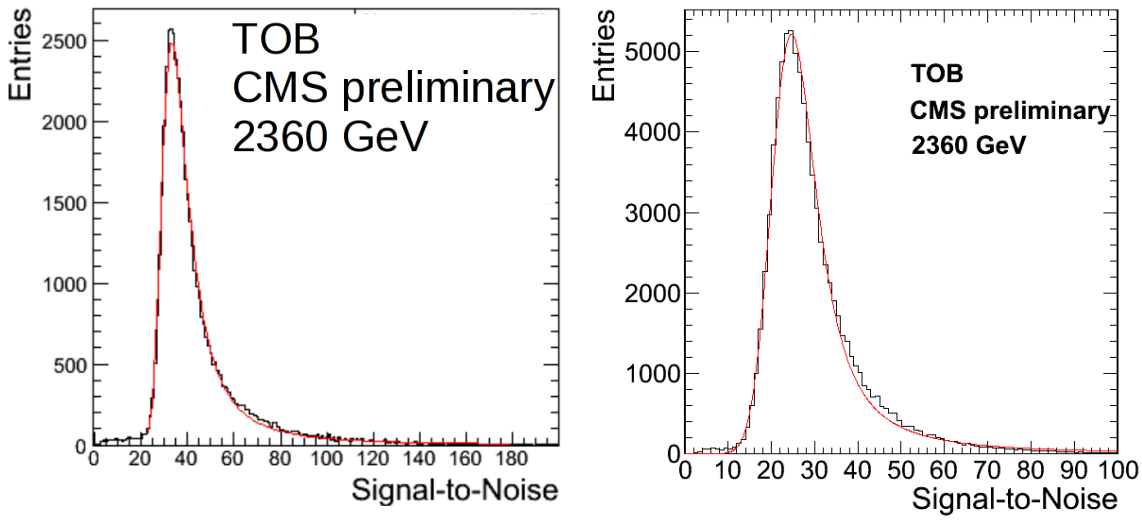

Figure 3.7: Signal to noise distribution in TOB for tracks taken in peak mode (left) and deconvolution mode (right) [4]

The achieved single point resolution for the z coordinate in the barrel is 230 μm in the TIB and 530 μm in the TOB, while the r-measurement in the endcaps varies with the strip pitch.

In total, the CMS strip tracker consists of 15,148 silicon micro-strip modules. Exact knowledge of each module's position is essential for most of the physics analyses. As the mounting precision is limited, track-based alignment is needed to further determine the module positions and to apply positional corrections in the reconstruction of the trajectory to improve the precision of the track parameters calculated via the trajectory fit (see section 3.4.1 for more details on the track reconstruction).
Due to the single-sided processing of the silicon sensors, the sensors are not entirely flat but show a significant bow, especially for the thick sensors [3]. The bow is required to be less than 100 μm.

The strip tracker can be operated in two different read-out modes, the so called *peak* and *deconvolution mode* [34]. In peak mode the charge collected is deduced by the height of the signal. This signal peak is reached at about 50 ns. In deconvolution mode the output charge for each strip represents a weighted sum of three consecutive pipeline cells in order to reduce the readout time to the 25 ns between two consecutive bunch crossings at nominal LHC luminosity [4]. The signal in deconvolution mode is about 10% smaller while the noise is slightly higher as in peak mode. This has implications for the signal-to-noise distributions as shown in figure 3.7 for hits in the TOB. To apply an equivalent quality cut for the signal to noise ratio of tracks taken in deconvolution mode compared to the tracks taken in peak mode, a signal-to-noise cut of 18 in peak mode has to be lowered to 12 in deconvolution mode.

3.2.3 Calorimetry

Besides the precise measurement of the trajectory information of a particle, the measurement of its energy plays an important role in particle identification and reconstruction. Therefore, CMS has an electromagnetic calorimeter (ECAL) that surrounds the tracker in the barrel while there is an additional preshower system installed in front of each ECAL endcap for π^0 rejection. Its main purpose is to identify and measure the energy of electrons and photons. Both ECAL barrel and endcaps are enclosed by a brass/scintillator sampling hadron calorimeter (HCAL) covering a pseudorapidity in the barrel region of $|\eta| < 3$. It is complemented by a tail-catcher in the barrel region (HO) resulting in a combined thickness in terms of interaction length of $10 - 15\lambda_I$. To make the coverage as hermetic as possible which is essential for the measurement of the missing transverse energy, there is an iron/quarz-fibre calorimeter in forward direction going up to $|\eta| < 5$ in pseudorapidity, as well as additional detectors in the most forward direction (CASTOR, ZDC) and the TOTEM detectors which are even outside the CMS detector.

The ECAL is made of 61,200 lead tungsten ($PbWO_4$) crystals in the barrel region ($|\eta| < 1.479$) and 7,324 in each of the two endcaps up to $|\eta| < 3$. The choice of lead tungsten scintillating crystals, which have a short radiation length ($X_0 = 0.89\,\text{cm}$) and Moliere radius (2.2 cm), allows the design of a compact calorimeter inside the solenoid. In the barrel region the crystals have a front face of $\approx 22 \times 22\ mm^2$ and a length of 230 mm, which corresponds to $25.8\,X_0$. They are arranged in a $\eta - \phi$ grid while in the endcap regions a x-y grid with crystals of $24.7\,X_0$ has been chosen. Within the time slot of 25 ns between two bunch crossings, 80% of the radiated light is emitted. It is amplified, sampled and digitised. The noise is about 40 MeV/channel. The energy resolution can be parametrised as follows:

$$\left(\frac{\sigma}{E}\right)^2 = \left(\frac{S}{\sqrt{E}}\right)^2 + \left(\frac{N}{E}\right)^2 + C^2 \tag{3.3}$$

where S is the stochastic term, determined to about 2.8% in test beam measurements, N denotes the noise of a super-module measured to be 0.12 GeV and C is a constant term measured to be 0.3% (see figure 3.8). This energy dependency leads to a resolution $\sigma(E)$ of less then 0.5% for $E = 100\,\text{GeV}$.

The hadronic calorimeter is essential for the measurement of missing transverse energy $\not{E}_T$ which is important for many studies of physics beyond the Standard Model. To provide a coverage of $|\eta| < 5$ the hadronic calorimeter consists of four parts: the barrel region(HB), the endcaps (HE), the hadron outer detector (HO), which is implemented outside the return yoke of the solenoid and the hadron forward calorimeter (HF), which covers the region very close to the beam pipe in the forward direction. Except for the HF, which is made out of steel, brass has been chosen as absorber material because it has a short interaction length and is non-magnetic. Plastic scintillator tiles which are read out with embedded wavelength-shifting fibres are used to measure the energy of the strong interacting particles. HCAL granularity of the three

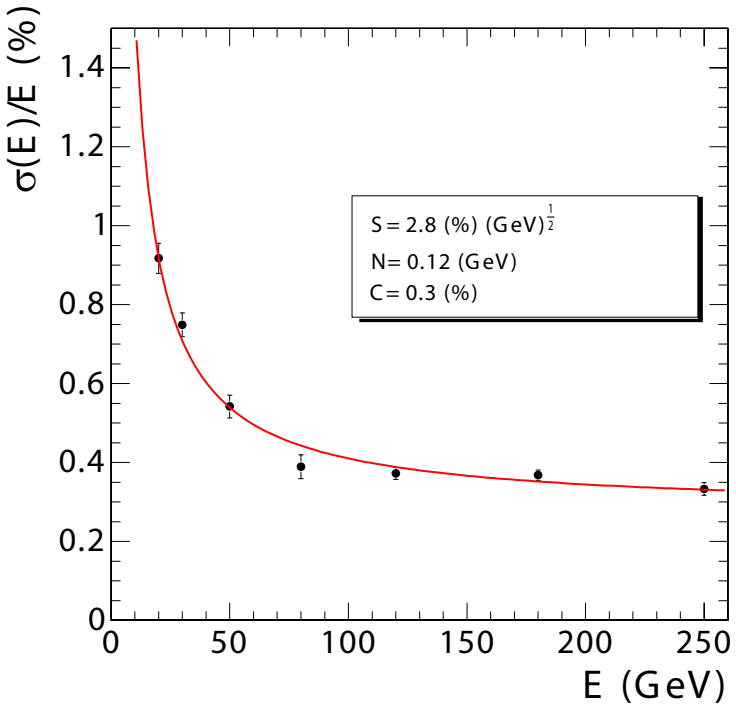

Figure 3.8: The ECAL energy resolution for a super-module measured in a test beam as a function of the electron energy [3].

geographic parts has been aligned such that the jet energy resolution as a function of E_T is similar in all parts as shown in figure 3.9. The jet energy resolution as a function of E_T is shown in figure 3.9 for different regions in $|\eta|$.

3.2.4 Muon system

The outermost part of the detector is the muon system. Figure 3.10 shows the design of the muon system for the barrel and endcap region. Its very large surface area and the different radiation environments had a large impact on the choice of technology. In the barrel region ($|\eta| < 1.2$) four layers of drift tube (DT) chambers are installed, separated from each other by one layer of return yoke. The first 3 stations measure the muon coordinate in the the $r\phi$-plane, the forth provides a measurement in z-direction, along the beam line. In forward region, where the neutron induced background rate is much higher, cathode strip chambers (CSC) are deployed, as they have a fast response, fine segmentation and a high radiation resistance. Again there are four stations of CSCs in each endcap separated by layers of the return yoke. The chambers are perpendicular to the beam line and while the cathode strips, which run radially outwards, provide a measurement in the $r\phi$-plane, the anode wires run approximately perpendicular to the strips and thus provide a measurements of $|\eta|$ and the beam-crossing time of the muon. Together both systems cover the full pseudorapidity interval of

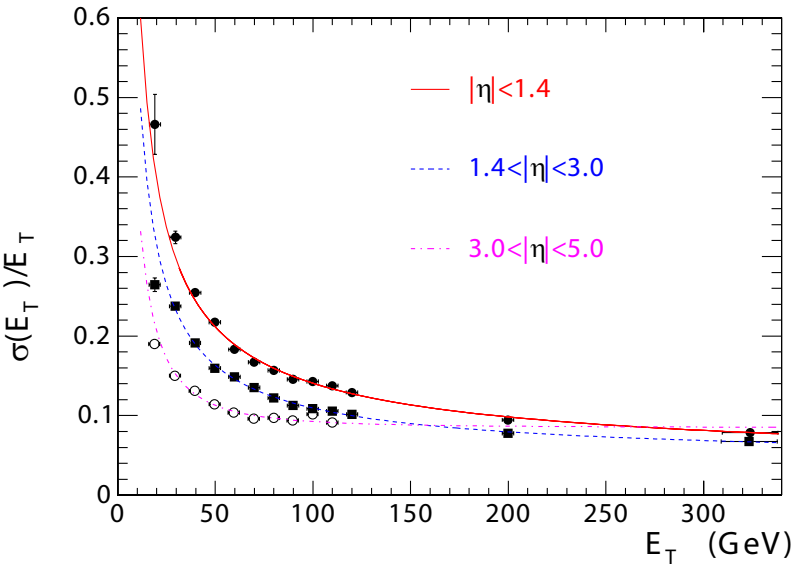

Figure 3.9: The jet transverse energy resolution as function of the simulated jet transverse energy for the barrel, endcap and forward region [3].

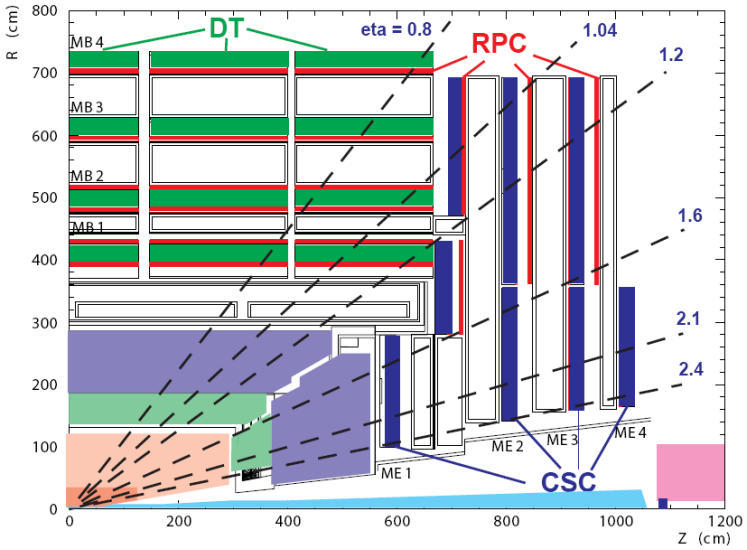

Figure 3.10: Four muon stations (MB1-MB4) are installed in the barrel region. Together with the four stations in the endcaps (ME1-ME4) a coverage of $|\eta| = 2.4$ is reached [3].

$|\eta| < 2.4$.

Although the muon is a weakly interacting particle and thus capable of passing the detector without loosing much energy, it undergoes multiple-scattering in the detector material before the first muon station; thus trajectory of the muon is influenced and the offline transverse momentum resolution of a muon reconstructed using information of the stand-alone muon system only is about 9% for small values of $|\eta|$ and p up to a muon p_t of 200 GeV. The resolution in the low momentum region can be improved by an order of magnitude by adding the measurement of the tracking system to the global muon fit as shown in figure 3.11.

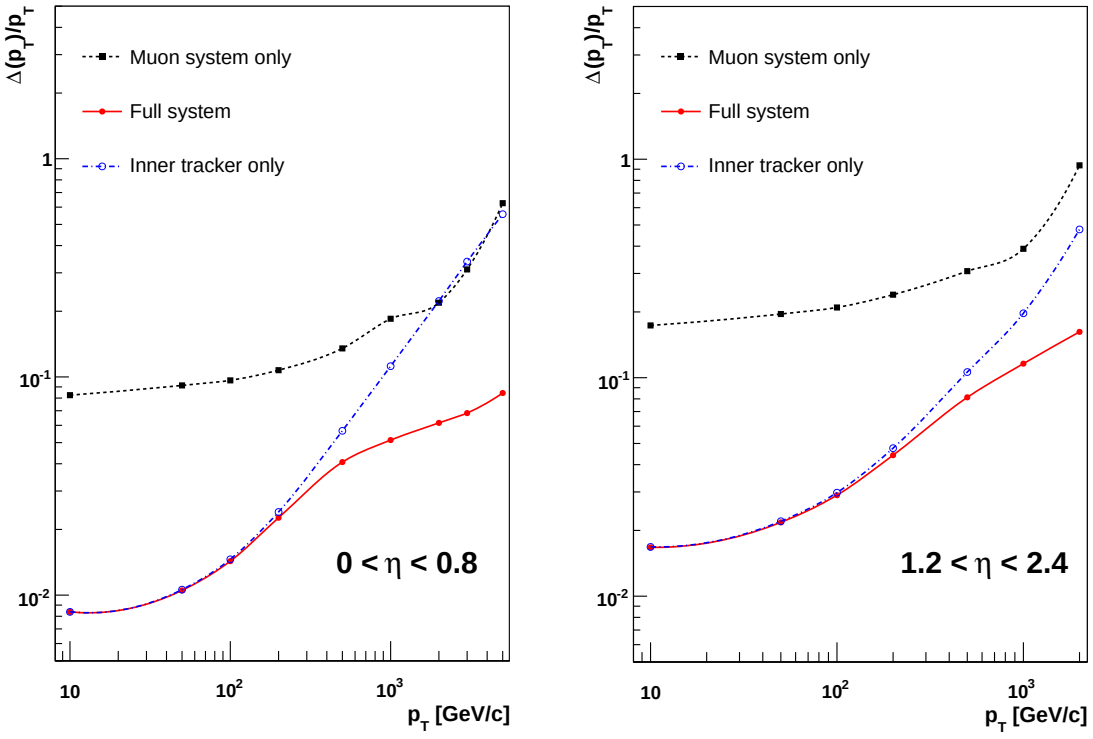

Figure 3.11: Muon reconstruction efficiency for stand-alone and global muons [3].

Even for muons with a $p_t > 1$ TeV the resolution using the combined information can profit from complementary measurements of the two systems, even though the single measurements of the tracking and muon system are of the same order of magnitude.

Although both the DTs and CSCs can each trigger on the transverse momentum of muons with good efficiency and high background rejection (Level-1 trigger resolution is about 15% in the barrel and 25% in the endcaps), there are additional resistive plate chambers (RPC) installed in both, barrel and endcap region, which provide an independent, fast and highly segmented trigger with a sharp transverse momentum threshold over the rapidity range of $|\eta| < 1.6$ of the muon system. These RPCs

were added to take into account the uncertainty in the eventual background rates and to guarantee the ability to measure the correct beam-crossing time at LHC design luminosity. region. Each layer is designed to give a four-vector, with a ϕ precision better than 100 μm in position and 1mrad in direction.

3.3 Trigger and Data Acquisition

Due to the bunch crossing rate of 40 MHz and up to 20 interactions per bunch crossing at design luminosity, about 10^9 interactions per second are expected at design luminosity of the LHC. As only data of 10^2 crossings/sec can be written to tape, the amount of data has to be reduced to the physics processes of interest. The CMS trigger system has to achieve a rejection factor of the order of 10^6 to lower the amount of data to a recordable size.

Each bunch crossing generates roughly 1.5 MB of data which results in 60 TB per second. Thus an efficient trigger system is necessary to reduce the amount of data to a feasible value for the storage system and offline computing facilities. The CMS trigger and data acquisition system (TriDAS), consisting of the detector electronics, the Level-1 trigger processors, the readout network and an online event filter system, is designed to select events at a maximum rate of $\mathcal{O}(10^2)$ Hz.

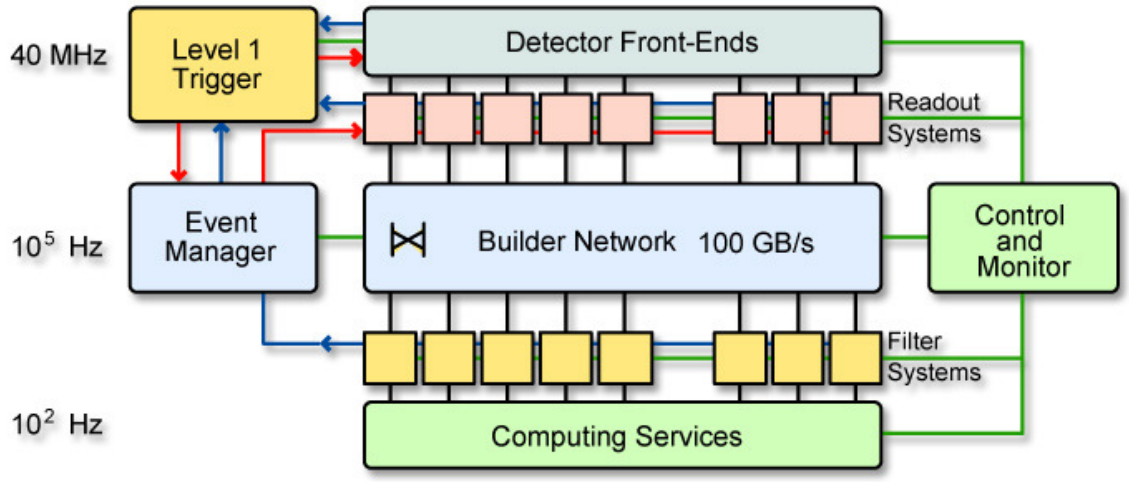

Figure 3.12: The reduction of data at the individual trigger levels [3].

The Level-1 trigger decision is based on the presence of primitive trigger objects reconstructed from reduced granularity and reduced resolution data from the muon and calorimetry systems. The total time allocated for the decision process is 3.2 μs. During this time the detector data is held in buffers, which are read out if the trigger threshold has been passed. The Level-1 trigger reduces the data by a factor of 400 to 100 kHz. The selected data is then transferred to a filter farm and for each event the same high-level trigger (HLT) software code is used to reduce the data even further

to 100 Hz (see figure 3.12). The amount of data available for analysis is expected to be about 1 PB/year at LHC design luminosity.
To make the data available for the different analyses performed all over the world the LHC computing grid has been developed, with the primary centre at CERN (Tier-0) supplemented by Tier-1 and Tier-2 computing centres at national laboratories and universities worldwide. To monitor the quality of the data taken by CMS, there are two monitoring circuits. First there is the online data quality monitoring (DQM) which is used to provide fast feedback and thus ensure the detector is recording good quality data. For each subdetector a specific data rate is defined for which certain histograms are produced, including basic detector read-out information as well as basic control variables from reconstructed events. For example, the tracker system is checked for basic information such as read-out errors of the front-end electronics, high voltage operation, as well as cluster shapes and even basic tracking information such as the overall χ^2 of the track fit. In a second monitoring step all the data recorded is analysed. Therefore, the full event is reconstructed for all data, typically within 24-48 h, and the full event information is used to investigate possible problems in more detail and/or give the finite data certification for physics analyses.

3.3.1 Alignment and Calibration Workflow

Alongside the monitoring of the data quality, the alignment and calibration workflows are embedded in the reconstruction chain of the data recorded by CMS. As illustrated in figure 3.13, parts of the data are reprocessed in the so-called 'express-stream' and the complete set of data is skimmed for the necessary data information needed to perform specific alignment or calibration tasks. These data skims are produced and stored at the calibration and alignment facility (CAF), whose computing power is reserved for tasks explicitly dedicated to calibration and alignment. New sets of alignment and calibration constants are stored in the offline condition database and can be used for prompt reconstruction which is delayed by 24-48 h.

3.4 Particle reconstruction at CMS

Besides meeting the high requirements for the hardware components of the CMS detector, the LHC also demands high standards on data-handling. After the events have passed the trigger steps described in section 3.3, the selected raw data has to be processed using high performance algorithms to reconstruct a particles way through the different subdetector components. While tracking algorithms associate the different hits recorded in the tracker system to trajectories of particle candidates, the calorimeter information of single cells is combined to energy deposits discriminating between particles according to their specific shower shapes. The muon system also provides stand-alone muon candidates reconstructed using information from the muon system only. The combined information of all subdetectors is then used to create particle candidates which can be used for physics analyses.

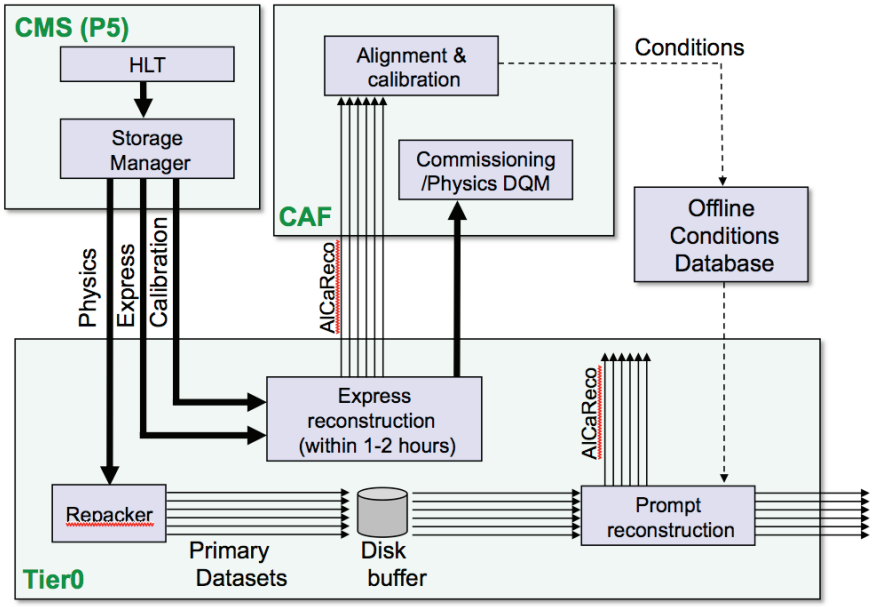

Figure 3.13: The data workflow for alignment and calibration tasks [3].

3.4.1 Track reconstruction

The track reconstruction in the CMS software framework CMSSW is done in four steps which are repeated for decreasing requirements on the input collection of hits:

- seed finding: find starting points of a possible trajectory
- pattern recognition: association of hits to the trajectory
- final trajectory fit: determination of trajectory parameters and errors
- collection cleaning and quality flagging: removal of hits associated to a track from the input collection and a quality assignment to the track according to the fit result

The default tracking algorithms used in the official CMS software package is the combinatorial track finder (CTF) [35] which will be described in more detail in section 3.4.1.2. It is a Kalman Filter based track finder, which uses the Kalman Filter both for the recognition of hits belonging to each trajectory, and for the estimation of track parameters.
The default tracking sequence applied in the CMS track reconstruction is an iterative approach, which runs the standard CTF tracking algorithm multiple times. At each iteration, the hits used by previous iterations are removed from consideration and the CTF tracking algorithm is run again with progressively looser setting, especially for the seeding step as shown in table 3.1.

Iteration	Seeding Layers	p_T cut (GeV)	d_0 cut (cm)	z_0 cut (cm)	min. number of hits
0	pixel triplets	0.5	0.2	15.9	3
1	pixel pairs	0.9	0.2	0.2*	3
2	pixel triplets	0.075	0.2	17.5	3
3	pixel pairs	0.35	1.2	7.0	4
4	TIB1+2 & TID/TEC ring 1+2	0.5	2.0	10.0	7
5	TOB1+2 & TEC ring 5	0.8	5.0	10.0	7

Table 3.1: Seeding layers and cuts for the different steps of the iterative tracking.The * indicates the impact parameter with respect to a pixel vertex

As both tracking algorithms use the Kalman Filter at some point, the following section outlines the basic principles of the Kalman Filter and its advantages, before the concrete seeding and the pattern recognition for the CTF algorithm is described in more detail, distinguishing between the reconstruction of tracks originating from collisions and tracks from muons produced in the atmosphere by cosmic rays.

3.4.1.1 Track fitting techniques

To reconstruct the trajectory of a charged particle passing through the detector volume, there are in principle two different basic approaches possible. The first approach is to fit the track globally, meaning that a vector describing the trajectory in a suitable tracking model starting at a certain point within the detector volume is used to describe the full path. The estimation of the final track parameters can then be derived by the Least Square Method (LSM). For a homogeneous magnetic field a helix describes the trajectory of a particle passing through the detector. In reality, the track usually deviates from a perfect helix caused by effects like multiple scattering in the detector material. such that the covariance matrix becomes non-diagonal because the effect of multiple scattering at a certain point of the trajectory influences all preceding trajectory points. In the case of multiple scattering the LSM needs the evaluation of the inverse of the $n \times n$ covariance matrix, where n is the number of measured coordinates. The computing time necessary for inversion grows as n^3 [36]. Neglecting the correlation between the measurements though leads to a non-optimal trajectory description. Alternative treatments of multiple scattering within a global approach will be introduced in section 4.3.2.1. Another possibility is to perform a local fit of the track, following the track from one surface to the other and updating the estimated track parameters every time a new measurement is available. One commonly used variant of this approach is the Kalman Filter. It provides a fast way to estimate the true value of a measurement that is itself smeared out by random effects

like multiple scattering. From the initial surface the known track parameters $\tilde{\tau}_i$ and given covariance matrix $C(\tilde{\tau}_i) \equiv C_i$ have to be propagated to the next position i+1 [36]

$$\tilde{\tau}_{i+1}^{(i)} = \mathbf{f}_{i+1}(\tilde{\tau}_i) \tag{3.4}$$

$$\mathbf{C}_{i+1}^{(i)} = \mathbf{D}_{i+1}^{(i)} \mathbf{C}_i (\mathbf{D}_{i+1}^{(i)})^T \tag{3.5}$$

$$\mathbf{D}_{i+1}^{(i)} = \partial \mathbf{f}_{i+1} / \partial \tau_i \tag{3.6}$$

where f_{i+1} is the precise track model between i and i+1.
The final estimate at the position i+1 is thus the properly weighted mean of the information of the actual measurement $\mathbf{m}_{i+1}$ and the prediction based on the information of all preceding detectors.

$$\tilde{\tau}_{i+1} = \left(\mathbf{C}'^{-1} + \mathbf{H}^T \mathbf{V}^{-1} \mathbf{H}\right)^{-1} \cdot \left(\mathbf{H}^T \mathbf{V}^{-1} \mathbf{m}_{i+1} + \mathbf{C}'^{-1} \tilde{\tau}_{i+1}^{(i)}\right) \tag{3.7}$$

The Kalman Filter is therefore a progressive fit. It has certain advantages:

- it can be used for both track finding and fitting
- no large matrices need to be inverted, the number of computations increases linearly with the number of detectors hit by the track
- the estimated track follows closely the path of the real track
- the assumption of a linear track model does not have to be valid for the whole track but only for the pathlength from one detector to the next

However, the method also has a fundamental drawback. The optimal precision is only known after the last step of the fit, as the track parameters only include the information from all preceding detectors. Therefore, the ability to discriminate outliers or ambiguities at an early step of the fit is low.
The reconstructed tracks are used as input for the vertex reconstruction and, if explicitly required, the momenta of the tracks and the full track-to-track covariance matrix can be reestimated with the vertex constraint, and thus improving the track parameters at this point [37].

3.4.1.2 Combinatorial Track Finder

For particles originating from the collision point, and thus the centre of the CMS detector, the track seeds are made from either three hits in the pixel, the so-called pixel triplets, or a pair of hits in the inner layers with the beam spot as an additional constraint. From these three points the initial track parameters are calculated under the assumption of a helical trajectory of a charged particle traversing through a constant magnetic field.

Depending on the precision of the initial track parameters a search window is opened around the predicted track position on the next outermost layer of the detector.

In case a hit is found within the search window the measurement is added to the track and the track parameters are updated as described in section 3.4.1.1. With the increasing number of measurements the precision of the track parameters is improved and the search window for new hits around the position of the propagated track crossing point gets smaller. In case of more than one missing consecutive hit the trajectory is discarded as fake and the propagation is stopped.

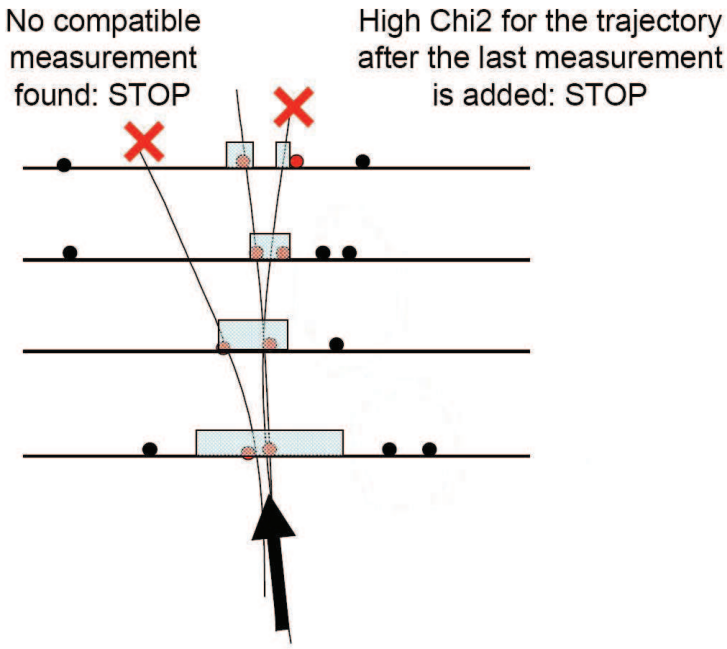

Figure 3.14: Pattern recognition based on the Kalman Filter [35].

In the concrete CMSSW implementation the trajectory state vector on each detector surface is $\vec{p} = (\frac{q}{p}, \frac{dx}{dz}, \frac{dy}{dz}, x, y)$ which is transformed into the curvilinear systems where it is parametrised as $\vec{p} = (\frac{q}{p}, \lambda, \phi, x_t, y_t)$ where $\frac{q}{p}$ is the inverse signed momentum of the track, λ denotes the dip-angle defined as $\tan\lambda = p_z/p_t$, ϕ is given by $\tan\phi = p_y/p_x$ and x_t, y_t are the hit coordinates on the local frame which is defined in such a way that its z-axis is tangent to the track's direction and its x-axis is parallel to the transverse plane. To counteract the drawback of the Kalman Filter approach of only having final precision for the state vector on the last surface, the fit is repeated in the opposite direction to recover the same degree of precision also for the innermost layer. To gain the final estimate both the forward and backward fit are combined.

The above procedure describes the seeding and pattern recognition for tracks originating from the interaction point. To enable the reconstruction of tracks having their origin outside CMS, as it is the case for cosmic muons, only the seeding step has to be adopted to the different conditions [35]:

- the seeds are made of hit triplets in the outermost and innermost barrel layers

and out of hit pairs from consecutive forward layers to the outermost layer of the detector

- no cuts on d_0 and z_0 can be applied as the tracks from cosmic rays do not necessarily traverse the tracker crossing the interaction region.

The normalized χ^2 resulting from the track fit for tracks from cosmic rays was larger than the one for tracks from the interaction point. A possible explanation was found to be the larger variety of impact angles under which tracks from cosmic rays hit the detector modules, which makes them more sensitive to deviations from the assumed module flatness. Studies with tracks from cosmic rays allowed a determination of the bow values orthogonal to the module plane of about $30\,\mu$m [38]. Figure 3.16 shows the χ^2-probability with respect to the impact parameter d_0, which is proportional to the impact angle α. With increasing angle or impact parameter, respectively, the χ^2-probability decreases significantly when the modules are described as rigid bodies. Allowing a kink angle between those modules which consist of two independent sensors but still assuming the single sensors to be rigid bodies helps to improve the description and thus leads to a χ^2-probability closer to the expected value of 0.5, especially for large impact angles. Allowing further degrees of freedom by assuming the sensors to be bowed instead of flat, flattens the χ^2-probability distribution up to an impact parameter of 50 cm.

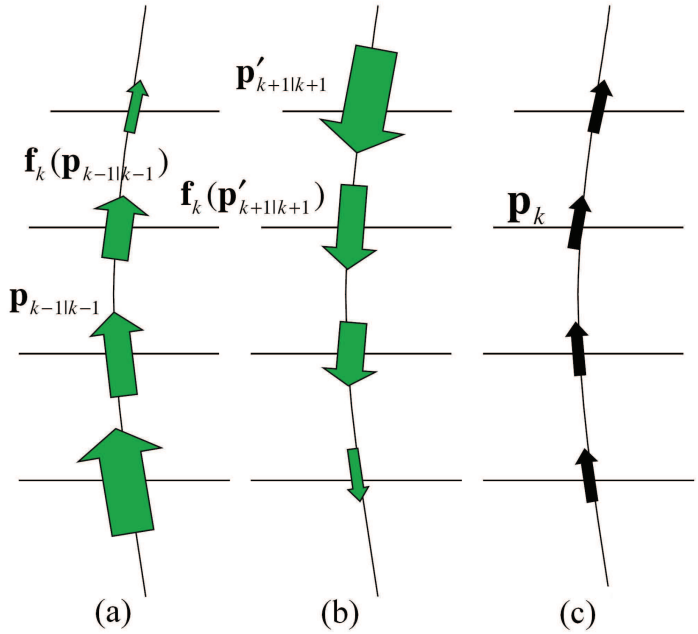

Figure 3.15: The size of the arrow illustrates the precision of the track parameters at a given layer for (a)forward fitting, (b) backward fitting and (c) the combined fit/trajectory smoothing. [35].

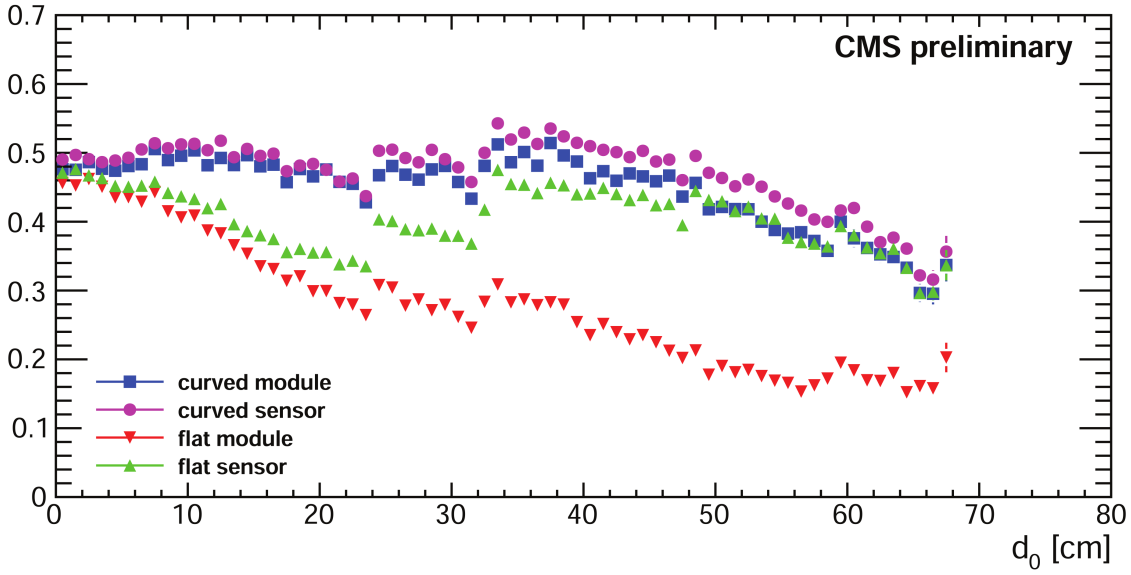

Figure 3.16: χ^2-probability as a function of the impact parameter d_0 for modules described as flat (red triangles pointing downwards), modules described as two sensors allowing a kink angle between them (green triangles pointing upwards), bowed modules (blue squares) and bowed sensors (magenta dots) for tracks from cosmic rays [38].

The improper description of the module surface as rigid body results in a bias of the cluster positioning errors (CPEs) assigned to the hits depending on the impact angle of the track as shown in figure 3.17. While the description is valid for small angles, the assigned value becomes too small for larger angles where the actual cluster width is much larger then the CPE. This effect is not reflected in the simulation and should be kept in mind when observing differences between data and simulation, especially if an effect shows a dependence on $|\eta|$. For large values of $|\eta|$ the tracks hit the modules under a larger angle.

3.4.2 Event simulation

To study detector responses and to develop analysis strategies, the expected physics processes are simulated using event generators like PYTHIA [40], Madgraph [41] or CMSCGEN [42]. The detector response is simulated based on GEANT4 [43] before the simulated events are reconstructed passing the same reconstruction sequence as the recorded signals by CMS as described in section 3.4.

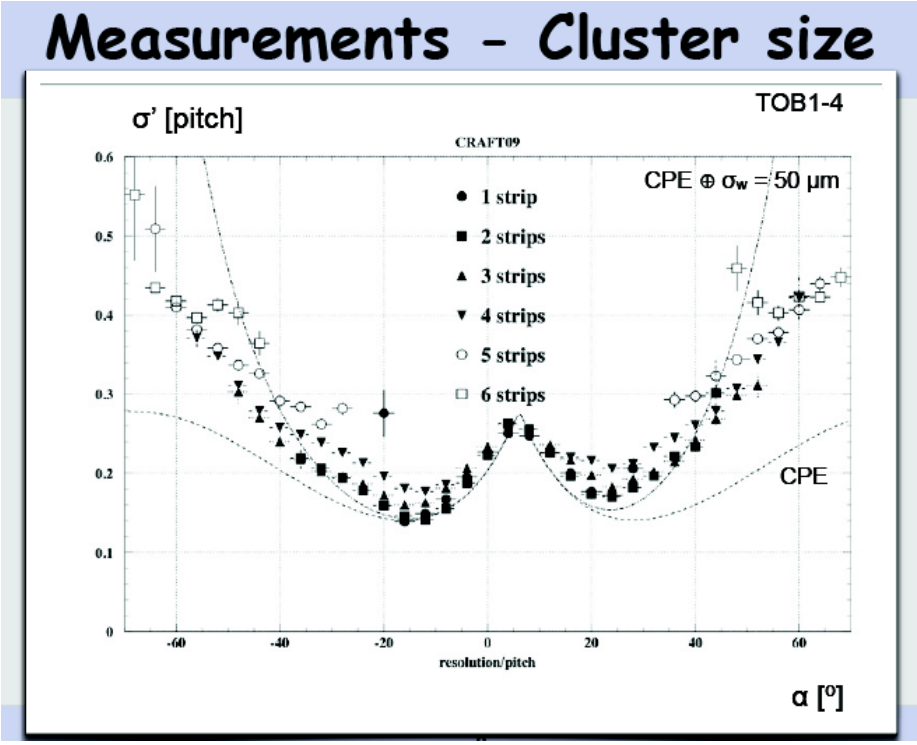

Figure 3.17: Hit position errors for layer 1-4 in the TOB in data and compared to the cluster positioning error (CPE) used in the default CMSSW track reconstruction for tracks from cosmic rays [39].

Chapter 4

Alignment

The CMS tracker was designed to provide excellent resolution for momentum measurements of charged particles. To achieve a desired precision on the measurement of the W boson mass of 15-20 MeV, the momentum scale has to be known to an accuracy of 0.02% to 0.025%, which implies the absolute detector positions to be known with a precision of better than 10μm in the rϕ plane [44].

Limited mounting precision as well as possible deformations due to temperature effects or influences of the magnetic field lead to misalignment which results in deviations from the real track recorded by CMS and the trajectory prediction used to extract the track parameters that are relevant for physics analyses as illustrated in figure 4.1.

Therefore, the tracks themselves are used to determine the exact module position. In

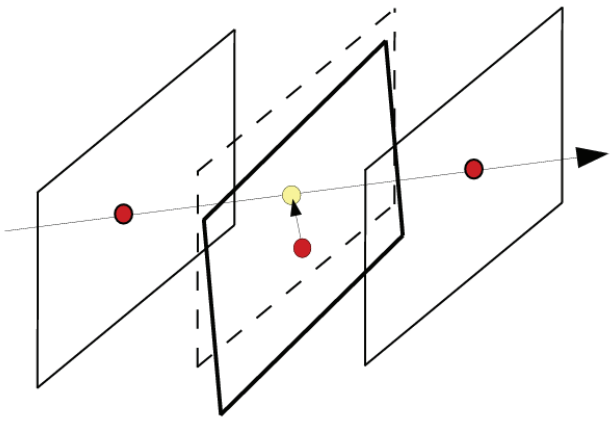

Figure 4.1: Displaced module leads to deviation between hit measurement and prediction.

this chapter the main concepts of track-based alignment will be introduced, followed by a detailed discussion of a possible solution to the resulting minimisation problem.

4.1 Track-based Alignment

The CMS tracker consists of more than 16.000 silicon modules as described in the previous section 3.2.2. In order to achieve an optimal track parameter resolution, the position and orientation of its modules need to be determined with a precision of a few micrometers. In section 3.4.1 the basic principles used in the CMS track reconstruction have been introduced, especially the fitting methods to estimate the track parameters. In the track-based alignment, not only the track quantities are free parameters, but also corrections to the position and orientation of the modules carrying the hits are fitted in order to minimise the deviation between measurements m_i and track predictions y_i

$$\chi^2(\boldsymbol{\tau}, \mathbf{p}) = \sum_j \sum_i r_{ij}^2(\boldsymbol{\tau}_j, \mathbf{p}). \tag{4.1}$$

where the residual is r normalised by the uncertainty of the measurement σ_i

$$r_{ij} = \frac{m_i - y_i(\boldsymbol{\tau}_j, \mathbf{p})}{\sigma_i} \tag{4.2}$$

Within the CMS collaboration there are three alignment algorithms implemented of which two have been used to align the CMS tracker before and during startup of LHC operations. The two algorithms are based on two different approaches to solve equation 4.1. The Hit and Impact Point (HIP) algorithm is a local approach that is applied iteratively, approximating equation 4.1 by assuming no track parameter dependence [45], such that an independent solution is calculated for each module. Hence, correlations between alignment parameters for different modules in one iteration are ignored and for misalignments many iterations are necessary to achieve convergence. Another approach is a global method, called Millepede II, which solves equation 4.1 in a single simultaneous fit of all global and local parameters. As the alignment results presented in this thesis are obtained using the Millepede II algorithm, the basic principles of the Millepede II algorithm as well as the integration of the standalone Millepede software package into the CMS software framework CMSSW will be outlined in this chapter.

4.2 The Millepede Alignment Algorithm

Solving equation 4.1 for millions of track and $\mathcal{O}(10^5)$ alignment parameters N in a reasonable computing time is not feasible since the computing time needed for inversion grows with N^3. Therefore, the Millepede approach exploits the distinction between the fit parameters. The track parameters are local parameters which are only present in a subset of the data, while the alignment corrections of the module positions are referred to as global parameters [5]. The global parameters of such a simultaneous fit can be determined from a matrix equation in such a way that the

matrix dimension is given by the number of global parameters only; for CMS of the order of 10^5. Hence, the computing resources and time can be limited to increase linear with N without loosing precision; the solution is still exact and the correlations between the parameters are taken into account without any approximation. In the following sections the basic methods and concepts underlying the Millepede algorithm will be explained, following the detailed description given in [5].

4.2.1 Mathematical concepts

In order to use a linear least squares fit to solve equation 4.1, it has to be linearised first, e.g. using the Taylor expansion up to the first order and $y_i(\boldsymbol{\tau}_{j0}, \mathbf{p_0})$ as linearisation point:

$$\chi^2 = \sum_j \sum_i r_{ij}^2(\boldsymbol{\tau}, \mathbf{p}) \tag{4.3}$$

$$\simeq \sum_j \sum_i \frac{1}{\sigma_i^2} \left(m_i - \left[y_i(\boldsymbol{\tau}_{j0}, \mathbf{p_0}) + \frac{\partial y_i}{\partial \mathbf{p}} \Delta \mathbf{p} + \frac{\partial y_i}{\partial \boldsymbol{\tau}_j} \Delta \boldsymbol{\tau}_j \right] \right)^2 \tag{4.4}$$

with $\mathbf{c}_i = (\frac{\partial y_i}{\partial p_1}, ... \frac{\partial y_i}{\partial p_n}, \frac{\partial y_i}{\partial \tau_1}, ... \frac{\partial y_1}{\partial \tau_m})$ as coefficients vector of the combined parameter vector $\mathbf{a} = (\Delta p_1, ..., \Delta p_n, \Delta \tau_1, ... \Delta \tau_m)$ the resulting normal equation can then be expressed as:

$$\underbrace{\sum_i \frac{1}{\sigma_i^2} (\mathbf{c}_i \cdot \mathbf{c}_i^T)}_{\mathbf{C}} \cdot \mathbf{a} = \underbrace{\sum_i \frac{1}{\sigma_i^2} (m_i - y_i(\mathbf{a}_0)) \mathbf{c}_i}_{\mathbf{b}}$$

$$\mathbf{C}\,\mathbf{a} = \mathbf{b}, \tag{4.5}$$

where $\mathbf{C}$ is a $(n+m) \times (n+m)$-matrix which is constant for linear problems and $\mathbf{b}$ is the constant part of the first derivative ∇F of the function 4.1. In the concrete case considered here the matrix $\mathbf{C}$ includes several sums over the track index k and many single-track-related sub-matrices:

$$\left(\begin{array}{c|c|c|c} \sum_k \mathbf{C}_k^{global} & ... & \mathbf{H}_k^{global-local} & ... \\ \hline \vdots & \ddots & 0 & 0 \\ \hline (\mathbf{H}_k^{global-local})^T & 0 & \mathbf{C}_k^{local} & 0 \\ \hline \vdots & 0 & 0 & \ddots \end{array}\right) \times \left(\begin{array}{c} \Delta \mathbf{p} \\ \hline \vdots \\ \hline \Delta \boldsymbol{\tau}_k \\ \hline \vdots \end{array}\right) = \left(\begin{array}{c} \sum_k \mathbf{b}^{global} \\ \hline \vdots \\ \hline \sum_k \mathbf{b}_k^{local} \\ \hline \vdots \end{array}\right) \tag{4.6}$$

The track index k can be of the order 10^6 for modern high energy detectors. C^{global} is an $n \times n$-matrix for n global parameters, C^{local} are l-by-l matrices and $H^{global-local}$ n-by-l matrices, if m track parameters are assumed. To be able to solve such a large matrix in a reasonable computing time, a matrix reduction is necessary. As shown in Appendix C the special structure of matrix 4.6 allows a matrix reduction such that for each local track fit the complete information is transferred to the global matrix. For each track a local fit is performed, the corresponding matrices C_k^{-1} and H_k are calculated and added to the global matrix in form of $-H_k C_k^{-1} H_k^T$ and to the vector b via $-H_k(C_k^{-1} b_k)$ [46]. After the loop over all tracks the complete information is collected and the matrix equation to be solved in order to extract the alignment parameters is:

$$\mathbf{C}'\ \mathbf{a} = \mathbf{b}' \tag{4.7}$$

with

$$\mathbf{C}' = \sum_k \mathbf{C}_k - \sum_k \mathbf{H}_k \mathbf{C}_k^{-1} \mathbf{H}_k^T, \qquad \mathbf{b}' = \sum_k \mathbf{b} - \sum_k \mathbf{H}_k (\mathbf{C}_k^{local})^{-1} \mathbf{b}_k \tag{4.8}$$

The matrix $\mathbf{C}'$ is now reduced to the size of the alignment parameters n. Still the computing time needed to invert matrix $\mathbf{C}'$ is proportional to n^3 and thus not suitable for a large number of alignment parameters. The Millepede algorithm uses MINRES [47] and sparse matrix storage to reduce the computing time and memory demands needed. The disadvantage of this method is that the covariance matrix $\mathbf{V}$ and thus the errors on the calculated alignment parameters are not available with MINRES. However, there is the possibility to calculate elements of the covariance matrix $\mathbf{V}$ with MINRES and thus get the errors for a set of selected parameters in a manageable computing time. For the chosen parameters j, the column vector of matrix $\mathbf{V}$ with index j is determined by the solution of the matrix equation $Cv_j = e_j$, where e_j is the j-th column vector of the unit matrix. The MINRES method can be used for a full or for a sparse matrix $\mathbf{C}$. For a sparse matrix with a large fraction of zero off-diagonal elements the memory demand can be reduced saving only the non-zero elements of the matrix and a pointer to store its position [48].

4.2.2 Hierarchical alignment via linear constraints

The CMS tracker has a hierarchical structure, partially introduced in section 3.2.2, which is mainly oriented at the mechanical support structures. A complete scheme for the pixel and strip detector hierarchy levels is shown in figures 4.2. With respect to track-based alignment introducing different hierarchy levels has several advantages. First, the determination of alignment corrections of larger hierarchy structures requires less data than a complete alignment of the lowest hierarchy level. Thus fast feedback can be given for example after changes in the run conditions like temperature or magnetic field which might lead to deformations or displacements of the tracker structures. In the special case of the CMS tracker the hierarchy can also be exploited to pass on information from the 2d-modules in the strip detector to the 1d-modules

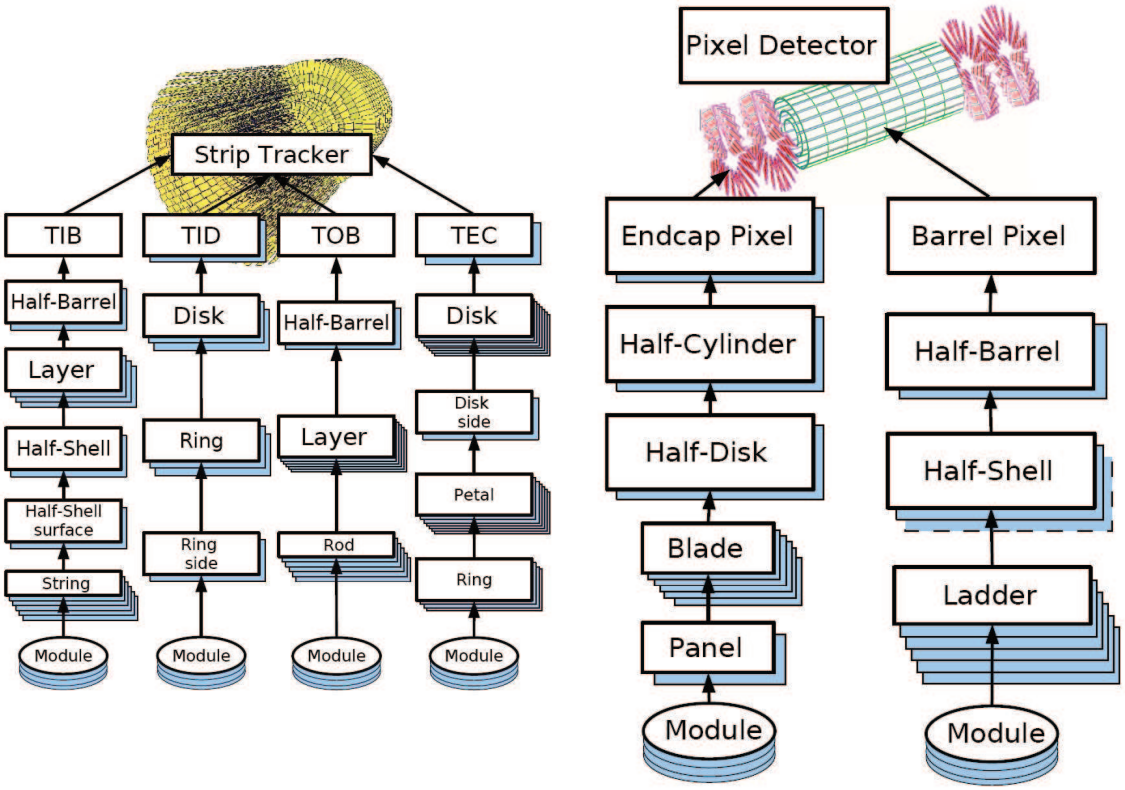

Figure 4.2: CMS tracker hierarchy [5]

via aligning a higher level structure containing both. In addition, the higher level structures allow to constrain the sum of all translations and rotations of the next lower level to be zero, as the parameter of the higher level are more accurately defined than the parameters of the sub-level. Therefore, equality constraints are added to the problem using the Lagrange multiplier method for linear constraints, in which for each single constraint an additional parameter λ is introduced. Equation 4.7 is extended to

$$\mathbf{C}'\mathbf{a} + \mathbf{A}^{\mathbf{T}}\lambda = \mathbf{b}' \tag{4.9}$$

where $\mathbf{A}$ has to fulfil the constraint equation

$$\mathbf{A}\ \mathbf{a} - \mathbf{m} = 0 \tag{4.10}$$

This system of two equations can be combined into one matrix equation

$$\left(\begin{array}{c|c} \mathbf{C}' & \mathbf{A}^{\mathbf{T}} \\ \hline \mathbf{A} & \mathbf{0} \end{array}\right) \times \left(\begin{array}{c} \mathbf{a} \\ \hline \lambda \end{array}\right) = \left(\begin{array}{c} \mathbf{b}' \\ \hline \mathbf{m} \end{array}\right) \tag{4.11}$$

Apart from the constrains given by the CMS tracker hierarchy, an overall reference frame needs to be defined in order to prevent the tracker of being translated

or rotated in space by the algorithm. This can be achieved by fixing the overall movement of the pixel half-shells for example.

4.2.3 Outlier rejection and iterations

Although from the mathematical point of view the matrix equation 4.7 can be solved in a single step, there are some reasons to perform a certain number of iterations. First of all potential inaccuracies in the solution of the large linear system like rounding errors in case of a large number of global parameters might require iterations. In addition, the treatment of outliers turns the linear to a non-linear problem. Hence, iterations are necessary, especially if the alignment is started from a largely misaligned detector geometry. In that case the initial global parameters may be far from optimal and, therefore, large residuals may occur even for non-outlier data. Thus removing large outliers before the global parameter determination can bias the result. Therefore, only huge outliers are removed automatically in every iteration while large outliers are rejected with decreasing cut values for the track χ^2 starting at the first iteration. The first two cut values can be chosen freely, after the second iteration the square root of the former cut value is taken.

4.3 Weak Modes

As shown in the previous section introducing a fixed reference system constrains an overall movement of the tracker in space, which would not influence the χ^2 minimised in the track-based alignment. Still there might be certain non-linear deformations that hardly affect the χ^2. These deformations are referred to as weak modes. They depend on the track topology and thus may differ for different kinds of tracks. Figure 4.3 shows an elliptical detector distortion. While for tracks from the collision point the track χ^2 using the original track parameters would be worse for the elliptically distorted detector geometry, a new set of parameter can be found resulting in the same χ^2 as for the non-distorted detector geometry and the original track parameters. Thus an elliptical distortion is a possible weak mode for collision tracks. Tracks from cosmic rays, though, would disfavour an elliptically distorted geometry since there is no set of parameters which results in the same track χ^2 for the elliptically distorted geometry. This example stresses the importance of tracks from cosmic rays for the detector alignment, since they connect the upper and lower part of the detector. Figure 4.4 shows a categorised summary of possible weak modes. The actual sensitivity has to be tested for the individual alignment strategy as it depends on the tracks used and the parameter selection.

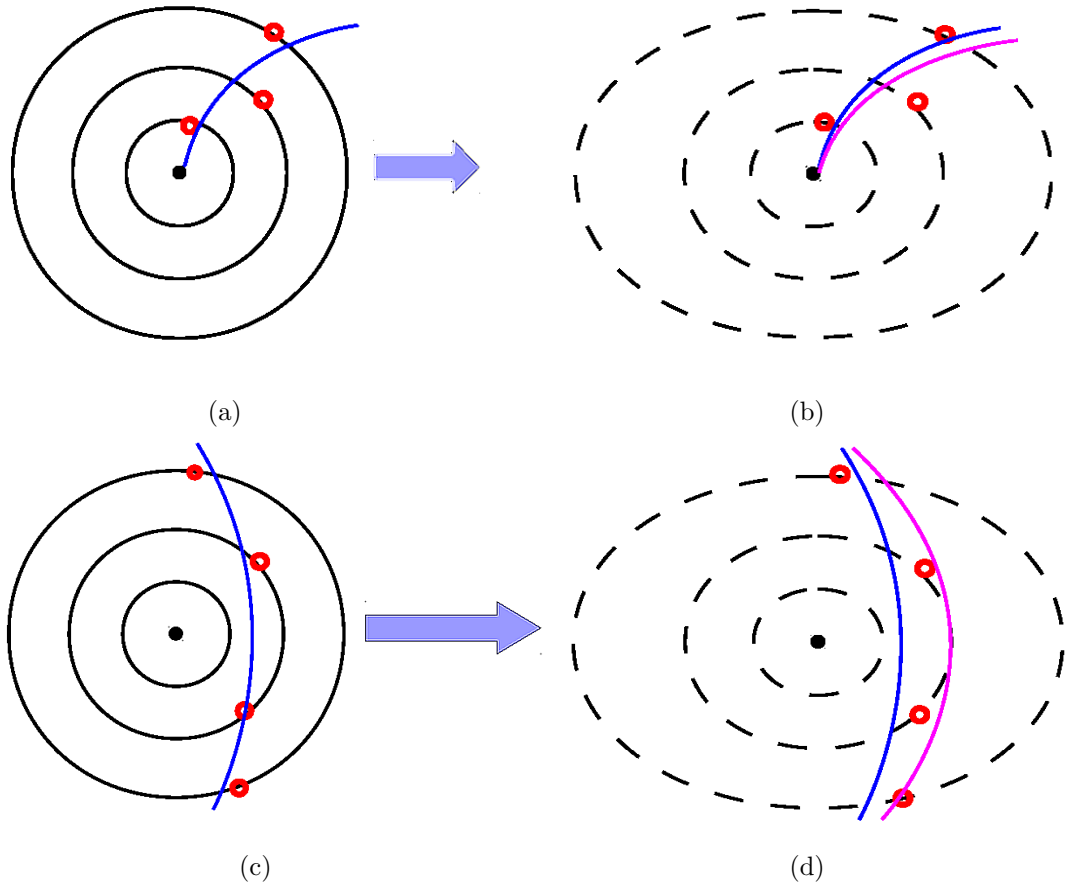

Figure 4.3: Influence of correlated detector distortion on track parameters for collision tracks (a, b) and for tracks from cosmic rays (c,d) [6].

4.3.1 Pre-sigmas and regularisation

Weak modes find their mathematical expression in small eigenvalues of matrix **C**' from equation 4.7, which means that even a small change in **b**' can result in a large change in **a**. **C**' is called *ill-conditioned*. The standard method to stabilise an ill-conditioned matrix is the usage of a priori knowledge on the accuracy. For every alignment parameter l an a-priori accuracy referred to as pre-sigma σ_l^{pre} can be defined and the resulting diagonal matrix $\mathbf{V}_{pre}$ is used to stabilise the ill-conditioned matrix by increasing the small (and all other) eigenvalues by the numbers chosen for the pre-sigmas [46]:

$$\begin{aligned} \mathbf{V}_{pre,ij} &= \delta_{ij}\sigma_{pre,i}\sigma_{pre,j} \\ \rightarrow \mathbf{C}' * \mathbf{a} = \mathbf{b}' &\iff \mathbf{C}' + \mathbf{V}_{pre}^{-1}\,\mathbf{a} = \mathbf{b}' \end{aligned} \tag{4.12}$$

The usage of pre-sigmas limits the step width per iteration towards the final solution, the global minimum. Nevertheless after a certain number of iterations the

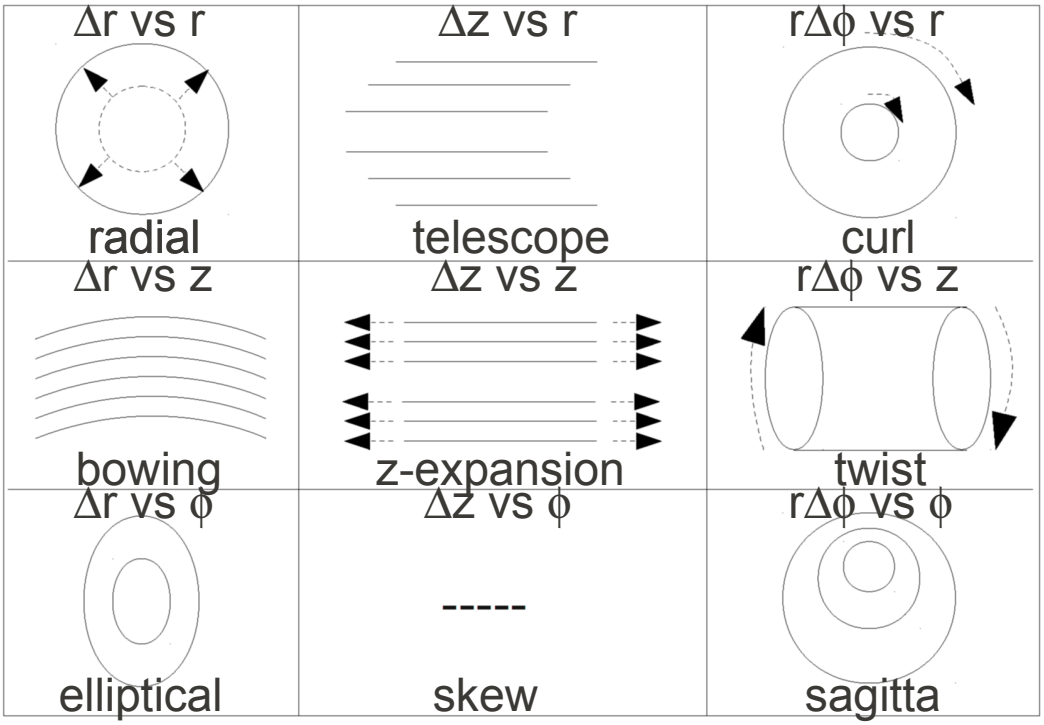

Figure 4.4: Possible detector deformations [6].

solution will be the same and a possible systematic deformation in the geometry might still be introduced.

Another attempt to suppress the contribution from weak modes is the so-called regularisation. The basic concept is to control the norm of the residuals and the norm of the solution vector **a** simultaneously by introducing a regularisation factor ω as shown in detail in [46]:

$$\chi'^2(\mathbf{a})_\omega = \chi^2(\mathbf{a}) + \omega(\mathbf{a})^T \mathbf{V_{pre}}^{-1}(\mathbf{a}) \tag{4.13}$$

translating into the matrix equation:

$$\mathbf{C} + \omega \cdot 1 \; \mathbf{a} = \mathbf{b} - \omega \mathbf{a} \tag{4.14}$$

Even though not necessarily solved via diagonalisation, the effect of the regularisation can be best seen for this solution method as only linear combinations with small eigenvalues λ are suppressed by the filter factors $f_j = \frac{\lambda_j}{\lambda_j + \omega}$

$$\mathbf{x} = \sum_{j=1}^{n} f_j \frac{1}{\sqrt{\lambda_j}} c_j u_j \qquad \text{with} \qquad c_j = j \frac{1}{\sqrt{\lambda_j}} (b^T u_j). \tag{4.15}$$

While the effect of the pre-sigmas depends on the number of iterations, the bias introduced by the regularisation is independent of the number of iterations. Millepede allows either to set one unique value for ω or to take the a-priori accuracies defined for each module group by adding the pre-sigmas. Both methods need careful studies to determine the correct pre-sigma values to be applied depending on the specific starting geometry. Too small values for the pre-sigmas might prevent the algorithm from converging to the final and actual position whereas too large values will not help in preventing the geometry to get distorted.

4.3.2 Track models used with Millepede

In section 3.4.1 basic principles of the reconstruction of the particles trajectory through the detector was already described. While the standard tracking within the CMSSW framework is using the Kalman filter technique as described in section 3.4.1.2, the simultaneous fit to all hits of a track as done in Millipede excludes such an iterative technique as it requires independent measurements. Thus for the accumulation step of the data alternative track models are needed to calculate the necessary values and derivatives to perform the global fit. The simple model of a helical trajectory description (see section 3.4.1.1) is in use for the initial track prediction, regardless of the trajectory model used in the fit. It can also be used for all following internal track refits, which have to be performed after every internal Millepede iteration to update the track parameters using the calculated global alignment parameters. As Millepede assumes independent measurements and thus a diagonal covariance matrix, the negligence of the off-diagonal elements, needed to take into account multiple scattering in the helix model, leads to a non-optimal trajectory description. The error assigned to the trajectory predictions is increased with every step along the predicted trajectory. To counteracted the effect of having small errors only for the innermost hit and large once for those further out each track can be used three times, propagating it once from the innermost hit, once from the outermost hit and once from a hit in the middle of the trajectory to both sides. Still the description will not follow the path of the real track accurately. Thus the helix model was extended via the introduction of break points and scatters, allowing to take into account multiple scattering. The implementation of the so-called *Broken Lines* are an equivalent description of the tracks compared to the Kalman filter.

4.3.2.1 Broken Lines Trajectory

The idea of the Broken Lines trajectory description is to take into account the material budget and thus multiple scattering by introducing scatters to the track model and fit additional offset parameters [49].
Multiple scattering of charged particles traversing material is mainly caused by Coulomb scattering from nuclei. Its effect after the traversal of a homogeneous medium of thickness x can be parametrised by two orthogonal, uncorrelated angles Θ and Ψ as drafted in figure 4.5 [2]. For a small deflection angle Θ a Gaussian

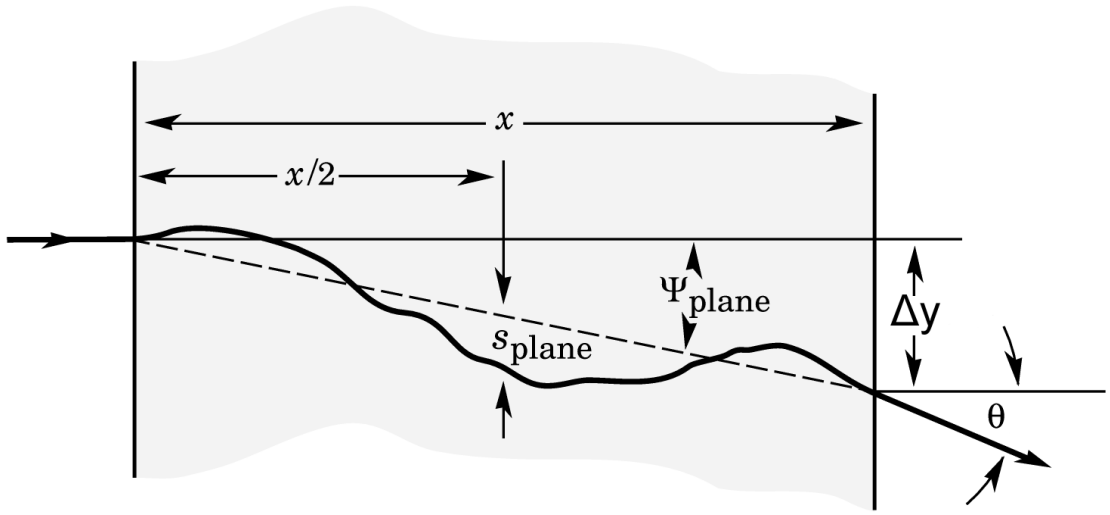

Figure 4.5: Multiple scattering of a particle traversing through matter of thickness x [2].

approximation is sufficient to describe the scattering with variance [2] :

$$V[\Theta] = \Theta_0^2 = \left(\frac{13.6MeV}{\beta pc}\right)^2 z\sqrt{(x/X_0)}[1 + 0.038\ln(x/X_0)]^2 \tag{4.16}$$

where p is the momentum of the particle, βc its velocity, z denotes the charge number of the particle and x/X_0 marks the thickness of the scattering medium in radiation lengths. For thin scatterers, like the silicon modules of the CMS tracker, Δy in figure 4.5 becomes zero and the multiple scattering can be simply parametrised by Θ_0.

The general description of the Broken Lines model is depicted in figure 4.6. Several thin scatterers (n_{scat}) are introduced in between the measurement planes - one thick scatterer is represented by two consecutive thin scatterers with similar mean and root mean square. For each scatterer a 2d-offset $\mathbf{u}_i$ is defined in the curvilinear system of the track and a prediction $\mathbf{u}_{int}$ for the measurement plane is interpolated by two adjacent scatterers using the curvilinear Jacobian [50] [51]. The resulting new residuals to be minimised are then $\mathbf{r}' = \mathbf{r} - \frac{\partial \mathbf{r}}{\partial \mathbf{u}} \cdot \mathbf{u}_{int}$. Furthermore, $u_{scat} - 2$ pseudo measurements of the 2d-kink-angles β_i with expectation value zero and variance according to the central scatterer $V[\Theta]_{central}$ is added to the fit, which are constructed by three consecutive scatterers, see figure 4.6. For the CMS tracker the description becomes simpler as the complete material is assigned to the measurement planes, meaning that measurement plane and scattering plane are the same. The initial trajectory and thus the residuals $\mathbf{r}$ are obtained by extrapolating the five helix parameters of a Kalman pre-fit at the first hit, assuming deterministic energy loss and no multiple scattering. The complete

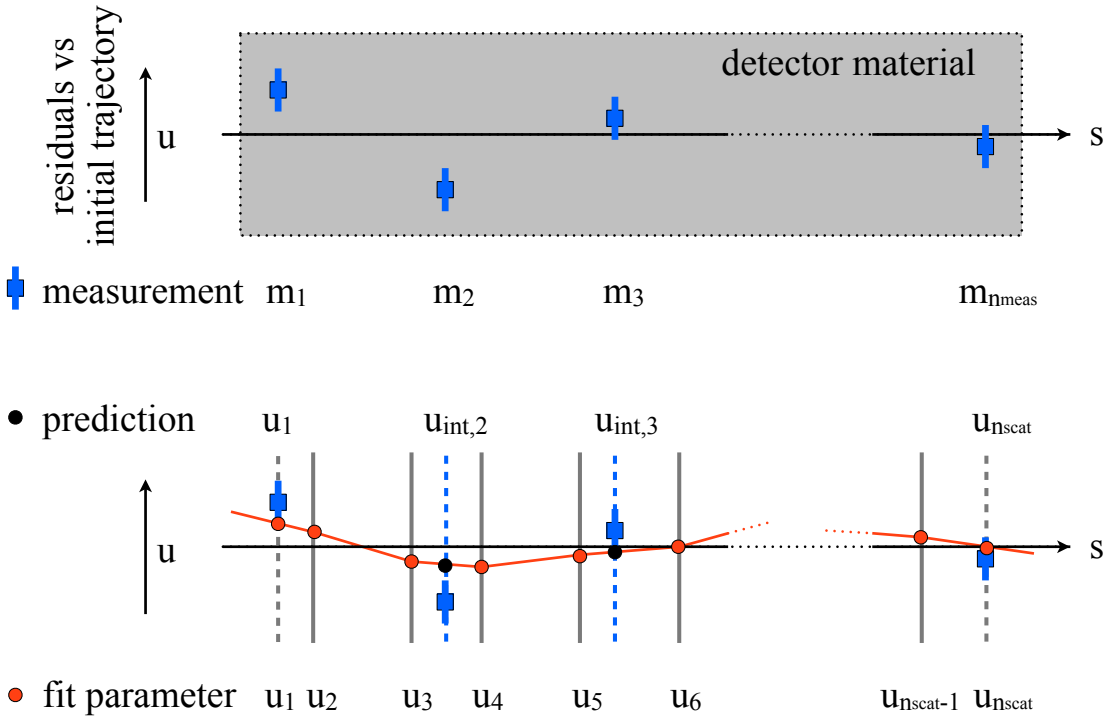

Figure 4.6: Treatment of scatterers within the Broken Lines trajectory description [7].

χ^2-function to be minimised can be formulated:

$$\chi^2\left(\kappa, \mathbf{u}_1, ..., \mathbf{u}_{nscat}\right) = \sum_{i=1}^{nmeas} \left(\mathbf{r}_i - \mathbf{P}_i \cdot \mathbf{u}_{int,i}\right) \mathbf{V}_{meas,i}^{-1} (\mathbf{r}_i - \mathbf{P}_i \mathbf{u}_{int,i})^t + \sum_{i=2}^{nscat-1} \beta_{\mathbf{i}}(\kappa, \mathbf{u}) \mathbf{V}_{\beta,i}^{-1} \beta_{\mathbf{i}}(\kappa, \mathbf{u})^t \tag{4.17}$$

where $\mathbf{P} = \frac{\partial \mathbf{r}}{\partial \mathbf{u}}$ is the projection of the offset defined in the curvilinear system to the measurement plane and $\mathbf{V}_{\beta,i}^{-1} = \begin{pmatrix} 1/\theta_0^2 & 0 \\ 0 & 1/\theta_0^2 \end{pmatrix}$. To get the corresponding linear equation system, the derivatives of $\mathbf{u}_{int}$ and the pseudo-measurement β with respect to the track parameters, which are common to all predictions, and after the $u_{i,scatterer}$ are needed, see Appendix D. As $\mathbf{u}_{int}$ and β only depend on 2 and 3 adjacent scatterers, respectively, the single matrices with the derivatives only have a small number of non-zero entries, namely those for $\frac{\partial}{\partial u_{i-1}}$, $\frac{\partial}{\partial u_i}$ and $\frac{\partial}{\partial u_{i+1}}$. The equation system $\mathbf{C} \cdot \mathbf{a} = \mathbf{b}$ to be solved can again be derived from setting the derivative of the objective function 4.17 to zero as shown in Appendix B. The matrix elements are given by:

$$c_{ij} = \sum_{k=1}^{n_{meas}} \frac{\partial \mathbf{r'}_\kappa}{\partial q_i} \frac{1}{\sigma_{m,k}^2} \frac{\partial \mathbf{r'}_\kappa}{\partial q_j} + ... \tag{4.18}$$

with $q(\kappa, u_1, u_2, u_3, ..., u_n)$. As each measurement is only depending on κ and another three $u_i$the resulting matrix is a bordered band matrix of width $w \leq 3 \times \dim(u) - 1$.The border size b is given by the number of track parameters which are common to the u_{int} – in this case only common track parameter is the curvature κ, meaning $b = 1$. Equation 4.19 illustrates the structure of the resulting matrix for the case of one dimensional u_{int}.

$$\left(\begin{array}{c|cccccccc} c_{00} & c_{01} & c_{02} & c_{03} & c_{04} & \dots & \dots & \dots & c_{0n} \\ \hline c_{10} & c_{11} & c_{12} & c_{13} & & & & & \\ c_{20} & c_{21} & c_{22} & c_{23} & c_{24} & & & & \\ c_{30} & c_{31} & c_{32} & c_{33} & c_{34} & c_{35} & & & \\ c_{40} & & c_{42} & c_{43} & c_{44} & c_{45} & c_{46} & & \\ \vdots & & & & \ddots & & & & \\ \vdots & & & & & \ddots & & & \\ \vdots & & & & & & \ddots & & \\ c_{n0} & & & & & & c_{n(n-2)} & c_{n(n-1)} & c_{nn} \end{array}\right) \tag{4.19}$$

The bandwidth of the matrix is here w=2, meaning all entries c_{ij} with $|i - j| > 2$ are zero [7]. It can be solved fast using root free Cholesky decomposition [52]. The computing time is proportional to $n \cdot w^2$.

4.4 Alignment parametrisation

The CMSSW convention for the alignment parameters is uniform for all different types of silicon sensors. So far the modules are described as rigid bodies with the translation direction along u,v and w and the rotations angles α, β and γ as depicted in figure 4.7. For the strip sensors the parameter u perpendicular to the strips is

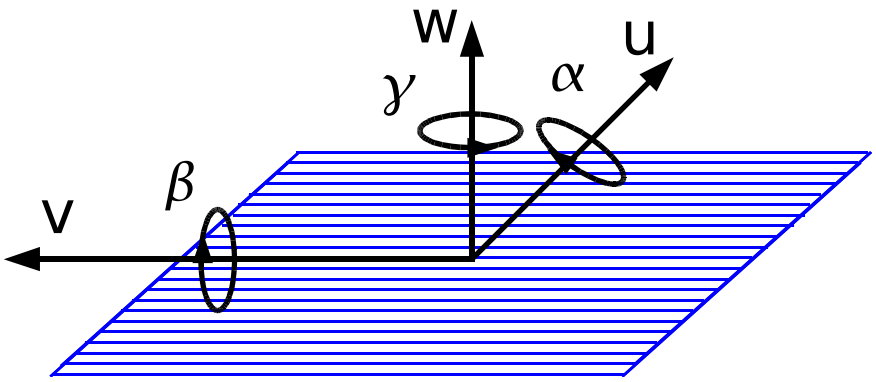

Figure 4.7: Alignment parameters convention for a strip modules.

the most sensitive coordinate and corresponds to the global $r\phi$-measurement in the

strip barrel detector and global ϕ in the strip endcaps, respectively. While the pixel modules provide similar precision for u and v, the v coordinate is not well defined for the strip modules. Only the stereo modules, described in section 3.2.2 provide a measurement in global z in the barrel and global r in the endcaps.

4.5 Millepede Integration into the CMSSW framework

Millepede is a standalone software package usable for any optimisation problem. The accumulation of the data and the solution method are split, the first part is referred to as 'mille' step, the latter as 'pede' step. The usage of Millepede II within the CMS collaboration is depicted in figure 4.8 [53].

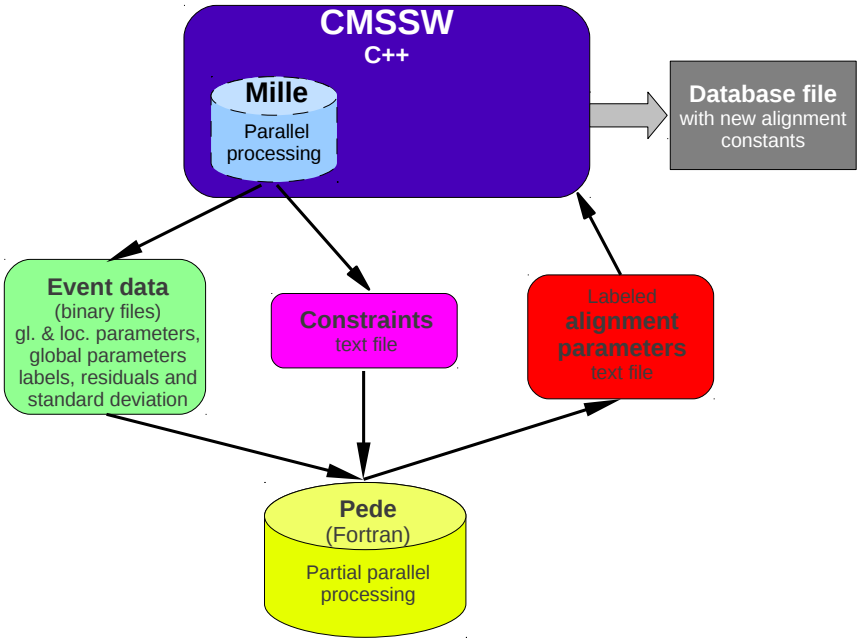

Figure 4.8: Schematic alignment process with the 'mille' step within the CMSSW framework, defined interfaces and the 'pede' process as external package.

The mille step is performed within the C++ written CMSSW software framework, while the pede step is defined in an external package which is written in Fortran and publicly available under [54].

In the mille step, the alignment parameters are selected and unambiguously labelled. For each measurement the following information is written to binary files which are passed on to the pede program:

m_{lc} = number of local parameters	array : $\left(\frac{\partial f}{\partial \tau_k}\right)_{p_0}$
n_{gl} = number of global parameters	array : $\left(\frac{\partial f}{\partial p_l}\right)_{p_0}$; label-array l
$z =$ residual ($\equiv y_i - F(x_i, \tau_\mathbf{0}, \mathbf{p_0})$)	σ = standard deviation of the measurement

The mille step can be easily parallelised as the track quantities are calculated event by event and the labels are fixed. The labelling follows a key which is related to the tracker hierarchy levels. In addition to the track-based input data, a text file with constraints can be passed on to pede. The pede program was made as parallelised as possible to reduce the time needed for one alignment circle. Apart from the reading of the input binary files and the creation of a list containing the selected alignment labels ($\propto n_{global}$), all loops within pede are parallelised. The number of threads to be used can be selected by the user. Each thread writes small update matrices for its processed records, the local track fits, to a write-cache which is read out in parallel to update the large matrix [55].
As a regular alignment with Millepede II requires to read the data from the binary files, a faster data handling could reduce the time needs drastically, but a parallel reading of the data files is only beneficial in terms of time, if the data is not read in from hard disc, because otherwise the disk speed limitation of about 40 MB/s is preventing a faster data handling. If the machine provides enough memory to read all data into the cache, the parallelisation can result in a read speed of 1 GB/s [55].
The calculated corrections to the module positions are added to the initial geometry, such that the constants written to the offline database (see section 3.3.1) contain the absolute positions and orientations of the modules which are used in the reconstruction of the tracks within the CMSSW framework. The constants to be used in the reconstruction are identified via a string referred to as tag, and assigned according to the run numbers of the event being processed. The complete sets of consistent alignment and calibration constants are summarized in the so-called global tags. The expert user can overwrite the constants defined by the global tag to investigate changes or differences between different sets of constants.

Chapter 5

CMS tracker alignment 2010

Before LHC started its physics program, the CMS experiment already took data from cosmic rays to commission the detector and collect experience in the operation of the several subdetectors. Furthermore, this data was used to perform first alignment and calibration exercises. The first global detector operation - with all subdetectors participating - was performed during autumn 2008. The detector recorded data with the magnetic field on, resulting in about 3.2 million tracks of secondary particles from cosmic rays used for a first alignment of the complete silicon tracker. The results can be found in [56]. Two further similar data taking periods took place in 2009 and 2010, each providing new alignment and calibration constants for the individual detectors to account for changes in the geometry induced by minor cooling incidents in the strip tracker and general changes in position due to the opening and closing of the detector. The strategy described in [56] only changed marginally for the repeated alignments in 2009 and 2010. First collisions at reduced centre of mass energy (900 GeV and 2.36 TeV) were recorded at the end of 2009, but the amount of data was not sufficient for a full tracker alignment. Only tests of the alignment workflows could be pursued with this data. Since March 2010, LHC has been providing collisions at a centre of mass energy of 7 TeV with a continuously increasing number of bunches per beam and thus increasing luminosity as shown in figure 3.1. In the following chapter, the alignment strategy using combined information of tracks from cosmic rays as well as minimum bias events from pp-collisions at a centre-of-mass energy of 7 TeV will be presented. In addition, the key methods to validate the alignments will be presented.

5.1 Data selection

With the startup of the LHC, two different types of data sources were available for the alignment that will be described in more detail in the following sections:

Dataset	**Data taking period & setup**
CRAFT10	data from cosmic rays taken in Feb. 2010, tracker in peak mode
- - - - - - -	- -
CDC2010	data from cosmic rays taken during collisions (dc), March till October 2010, tracker in deconvolution mode
MinBias	pp-collisions at $\sqrt{s}$ =7 TeV, March till October 2010, tracker in deconvolution mode

As described in chapter 4, tracks from cosmic rays are an essential input for the alignment since their different track topologies with respect to collision tracks help to constrain possible weak modes. Due to the limited number of tracks from cosmic rays crossing the forward direction of the detectors, tracks from collision events are added. The corresponding hit maps can be found in Appendix G. In the following sections, the main features of the two data samples used for the alignment will be described, highlighting the main differences and complementary information they provide.

5.1.1 Selection of muon tracks from cosmic rays

The phase space covered by muon tracks from cosmic rays is different from those of collision tracks. The muon does not traverse the detector from the collision point outwards but starts in the outermost layer of the detector and propagates through the detector into all possible directions. This has consequences for the tracking as described in section 3.4.1. For the track-based alignment, these events are essential as they connect different parts of the detector and thus help to constrain degrees of freedom which are only weakly or not at all sensitive to tracks originating from the collision point. The muon tracks also hit the module surface under all possible impact angles which results in different systematics. They are, for example, more sensitive to deviations from the assumed module flatness.

The momentum and angular spectra of cosmic muons reconstructed in the CMS tracker volume are shown in figure 5.1. The track parameters are defined at the point of closest approach to the CMS nominal interaction point, considering all particles traversing CMS from top to bottom. The asymmetry about $\phi = -1.5\,\mathrm{rad}$[1] is due to the excess of positive over negative cosmic ray particles entering CMS (see section 2.5) and the bending of charged tracks in the magnetic field of the solenoid. Positively charged cosmic rays tend to peak just above 90° whereas negatively charged cosmic

---

[1] In the CMS convention the track ϕ-value is defined from 0 to $(-)\pi$ for tracks directing into the upper(lower) hemisphere of the detector.

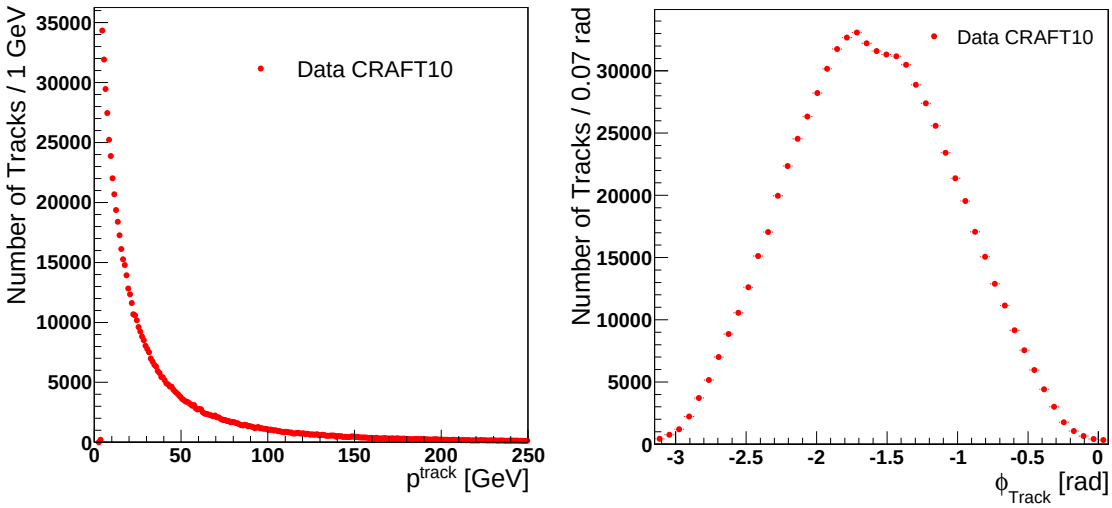

Figure 5.1: Momentum p (left) and azimuthal angle ϕ (right) spectra of muons from cosmic rays reconstructed in the CMS tracker volume based on the selection criteria described in the text. Vertical cosmic ray tracks correspond to $\phi = \theta = 90°$ [56].

rays tend to peak just below 90°. The asymmetry about $\theta = 90°$ is mainly due to the asymmetric location of the cavern shaft above the detector.

The tracks from cosmic rays which were considered for the alignment presented in this thesis were taken in peak mode as described in section 3.2.2.2. To provide good quality tracks usable for alignment without drastically reducing the size of the sample, the following criteria were applied. Each track was required to have

- at least eight hits,
- a signal-to-noise ratio larger than 18 in the silicon strip modules,
- a probability of the pixel hit matching the template shape [57] of at least 0.001 (0.01) in the local u (v) direction
- a momentum greater than 4 GeV,
- at least two hits on either pixel or stereo strip modules, allowing a measurement of the polar angle θ.

Hits were also rejected if the track angle, relative to the local uv plane, was less than 20°. In total, about 2 million tracks from cosmic rays were selected for alignment, out of which about 3.5% had at least one hit in the pixel detector.

The track reconstruction used the Alignment Position Errors (APE), the estimated initial uncertainty on the module position in the three global coordinates, which were

added in quadrature to the hit errors during the pattern recognition and track fitting procedure [58]. This allowed efficient track reconstruction in the presence of misalignment and a reasonable pull distribution of track parameters.

5.1.2 Track selection from minimum bias events

The majority of proton-proton-collisions taken place at the LHC are soft interactions, without any hard scattering of the partonic constituents of the proton [17]. The particles traversing the detector after these elastic and inelastic scatterings are mainly hadrons - pions and protons - and thus differ not only from the track topology but also in terms of energy loss and multiple scattering from the muon tracks described in the previous section. Due to rapidly changing trigger settings in the beginning of LHC operations, it was decided to require one good reconstructed vertex with

- number of degrees of freedom >= 4
- distance of the position in global $z <= 15\,\text{cm}$ with respect to the beam spot
- radial distance from the beam spot $\rho <= 2\,\text{cm}$

instead of changing 'quality' trigger[2] to ensure that only good quality events from collisions were selected. Analogue to the track selection for cosmic rays each track was required to have

- at least eight hits,
- a signal-to-noise ratio for the strip modules of 12,
- a probability of the pixel hit matching the template shape for collisions data [57] of at least 0.001 (0.01) in the local u (v) direction
- a particle momentum larger 3 GeV,
- a transverse momentum p_T larger than 0.65 GeVand
- at least two hits either on pixel or stereo strips

The signal-to-noise ratio for the strip modules is decreased compared to the selection of cosmic ray tracks since the tracker is read-out in deconvolution mode during LHC operations (see section 3.2.2.2). The requirement for hit rejections in case of a very small incidence angle relative to the local uv-plane was lowered to 10° in order to keep the tracks passing the innermost pixel barrel layer at large $|z|$-values. Tracks with a momentum below 3 GeVare heavily influenced by multiple scattering and are thus not useful for alignment. In total, about 8 million tracks from minimum bias events have been used for the alignment, distributed over the whole run range with a slight

[2] At the beginning of LHC operation, the technical trigger bit 0 was set when all detector systems were operating well.

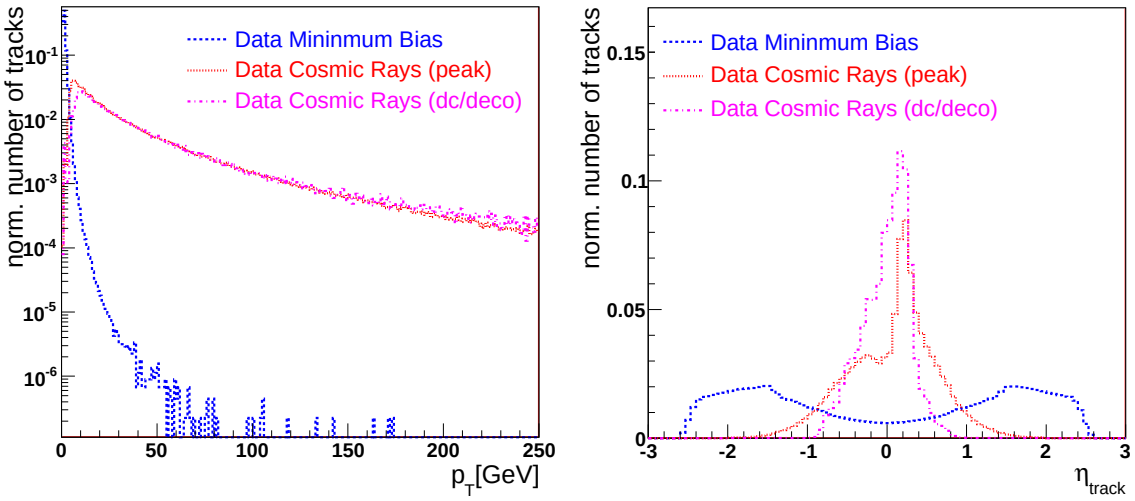

Figure 5.2: Transverse momentum and η spectra for tracks from minimum bias collisions (blue, dashed line) and for tracks from cosmic rays taken in peak mode (red, dotted line) and during collisions (dc) taken in deconvolution mode.

imbalance towards the later run periods because of the larger number of tracks per events with increasing luminosity.

The transverse momentum and η-distribution for tracks from minimum bias events, in comparison to tracks from cosmic ray events, are shown in figure 5.2. Minimum bias events have mainly low momentum tracks but these tracks illuminating the forward region of the detector with $|\eta| > 1.4$.

5.1.3 Tracks from cosmic rays during collisions

In addition to the data taken from cosmic rays before the start of LHC operations, there are also tracks from cosmic rays recorded during collision data taking. The track selection is almost the same as for tracks from cosmic rays during off beam operations but as the detector is operated in deconvolution mode, the calibration constants differ as additional corrections have to be applied, see Appendix F. The resolution of the tracks from cosmic rays taken in deconvolution mode is slightly degraded compared to tracks from cosmic rays taken in peak mode independent of the alignment as indicated in figure 5.3. Shown is the width of the residuals as defined in section 4.1 estimated[3] by the root-mean-squared (RMS) for the TOB. Since the RMS is quite sensitive to outliers, the residual distributions were only considered if they had more than 50 entries.

The RPCs used to trigger muons in the muon system are divided into 5 wheels from W-2, over W-1, W0, W1 to W2, each consisting of 12 sectors. The trigger used

[3]A detailed description of the track based validation is given in section 5.4.1. The plot shows the width of the residual distribution of the local u' coordinate.

to select these data is the L1 technical trigger bit 25 which requires a top-bottom coincidence of opposite muon sector triggers as illustrated in figure 5.4. The trigger logic is designed in a way that mainly muons passing the inner tracking volume are selected [8]. The setup also allows the combination of triggers from different wheels (inter-wheel logic) within the following combinations:

- W-2 ⊠ W-1
- W-2 ⊠ W0
- W-1 ⊠ W0
- W-1 ⊠ W+1
- W-1 ⊠ W+2
- W0 ⊠ W0
- W+1 ⊠ W0
- W+2 ⊠ W0

This selection leads to a restricted η-coverage up to ± 1 of the recorded tracks from cosmic rays as shown in the right plot of figure 5.2.

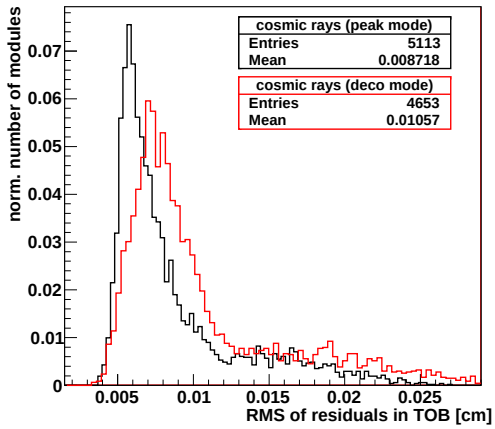

Figure 5.3: Distribution of the RMS of the residuals for modules in TOB for tracks from cosmic rays taken in peak and deconvolution mode.

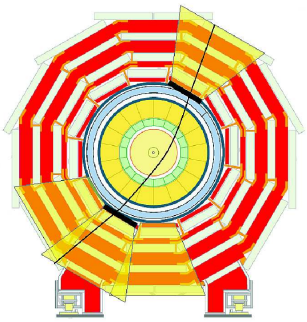

Figure 5.4: Top-bottom coincidence in muon triggers for cosmic rays during collisions [8].

5.2 Alignment Strategy

Careful monitoring of the pixel geometry indicated movements of the pixel half shells along global z over the data taking period in 2010. A detailed description of the validation procedure will be presented in section 5.4.3. The resulting changes in the geometry created the need for different alignment constants for seven identified run ranges listed in table 5.1.

period	run range	time range
(A1 cosmic rays)	127333 - 131510	[2010.02.11-2010.03.20]
A1	132440 - 133928	[2010.03.30-2010.04.26]
A2	133929 - 139964	[2010.04.26-2010.07.11]
B	139965 - 140399	[2010.07.11-2010.07.19]
C	140400 - 143487	[2010.07.19-2010.08.21]
D	143488 - 146427	[2010.08.21-2010.09.22]
E	146428 - 148126	[2010.09.22-2010.10.18]
F	148127 - 149509	[2010.09.18-2010.11.03]

Table 5.1: Intervals of validity for the alignment constants.

Performing separate alignments for the different run ranges to account for the changes observed in the pixel half-shell positions would prohibit to profit from the cosmic ray data taken before LHC started operations. Since data from cosmic rays represents an essential input for alignment, the possibility of a simultaneous alignment of different hierarchy levels with a global approach was exploited. It accounts for the changes of the pixel half-shell positions over time but still allows the usage of all data from cosmic rays taken in 2010 to determine the module positions with respect to the larger hierarchical structures to the best possible precision.
Therefore, run range dependent constants were determined for all six degrees of freedom of the pixel barrel layers and pixel forward half-discs, while all other parameters were considered stable over the whole run range. That way all data taken for the alignment was used to determine the module positions with respect to the large structures and only the pixel layers and discs were allowed to move time dependently. All six degrees of freedom were determined for the large hierarchy structures :

- pixel barrel layers and pixel forward half-discs
- TIB and TOB half-shells
- TID and TEC end-caps.

The sum of the movement of the two TOB half-shells was constrained to zero in order to define a reference frame and prevent an overall movement of the tracker in

space since an overall translation or rotation is not defined by the χ^2-minimisation problem, see section 4.3.1. The single modules were aligned in three to five degrees of freedom depending on the subdetector. The 2d-modules in the strip detector were treated separately as single rϕ and stereo modules, and, since the v coordinate along the strips was not aligned, there is only little sensitivity in global z direction from the stereo modules.

- pixel modules: u,v,w and γ
- TIB modules: u,w,α,β and γ
- TOB, TID and TEC modules: u,w and γ

Due to the expected shifts of the pixel half-shells, no pre-sigmas and regularisation were used to ensure that the corrections of the pixel layer and half-disc movements were not damped. Thereby the final positions were reached within four internal Millepede iterations. Millepede was configured to use the Broken Lines track model for the local track fits as described in section 4.3.2.1. The treatment of outliers was dealt with by using a progressive cut, related to the χ^2-value corresponding to three standard deviations; for example χ^2=9 for one degree of freedom, χ^2=26.9 for ten degrees of freedom. The cut value to be configured is then the multiplication factor for the χ^2-value. To ensure that modules which were not aligned in previous alignments using tracks from cosmic rays only - especially in the pixel forward detectors - the initial cut value was chosen to be rather loose. It was set to 30 in the initial loop, lowered to 6 in the second and further to the square-root of the value of the preceding loop until it reached the termination condition of 1 after the fourth iteration. In this last iteration about 9% of tracks were rejected by the χ^2-criterion, the majority being tracks from cosmic rays. Among other reasons, this is due to the known deficiency of the silicon module description as flat sensors as described at the end of section 3.4.1.2. In principle, the final alignment result is independent of the starting geometry if enough iterations were performed to counteract the influence of outliers or other non-linear effects. Nevertheless, the starting geometry can influence the final position in terms of weak modes as described in section 4.3. Because of the decision to waive the usage of pre-sigmas or regularisation to ensure the correction of the pixel position, weak modes have to be monitored with special care. The starting geometry for the alignment was artificially distorted in order to correct for an observed weak mode as will be discussed in detail in section 6.2. The final constants uploaded to the database were labelled as *TrackerAlignment_GR10_v4_offline* and used for the reprocessing of the data taken in 2010 that took place in April 2011. This combined geometry will be referred to as ***GR10_v4*** in the following.

5.3 Realistic misalignment scenario for Monte Carlo simulations

For most physics analyses, the comparison between data and simulation is an essential ingredient to develop analysis strategies, test methods and, if not otherwise determinable, to estimate efficiencies or background contributions. The misalignment scenarios used for this purpose were supposed to represent the situation of the alignment precision in data after the collection of $10\,pb^{-1}$, $100\,pb^{-1}$ and $1\,fb^{-1}$ of collision data. The residuals were simply smeared out using Gaussian and uniform distributions assuming average module displacements between 50 and 250 μm depending on the subdetectors [59]. The number of tracks from cosmic rays and first collisions was expected to allow only an alignment of detector structures larger than the single modules, with an accuracy for the disc/layer level in the pixel detector of roughly 10 μm and for the corresponding hierarchy levels in the strip with an accuracy of 100 μm.

Due to the delay of LHC operation and the possibility to record over three million tracks from cosmic rays and use them to align the tracking detector, these estimated scenarios were no longer a good representation for the detector performance at the beginning of collision data taking. Therefore, a realistic description of the detector was needed to have similar performance in simulation and data. In order to incorporate not only diced misalignments but also systematic deformations arising from weak modes that might have been introduced in an alignment with tracks from cosmic rays only, the alignment corrections obtained on data using tracks from cosmic rays only were added to the design detector geometry and considered a start misalignment scenario in the simulation. Then a full alignment following the same alignment strategy as in the data was performed [56]. The resulting geometry was uploaded to the database as *TrackerAlignment_CRAFT08Realistic_mc* and used for event simulation in the first half of 2010. Starting from this realistic geometry representing the conditions at LHC startup fairly well, a second alignment following the strategy described in the previous section was performed using simulated events from cosmic rays and collisions to include the complementary information of collision tracks in the misalignment scenario for the simulation. The results can be considered as an estimate of the remaining misalignment in data and provide a misalignment scenario for studies using simulated events close to the realistic conditions in data. The scenario was tagged as *TrackerAlignment_2010Realistic_mc* and was used for the production of simulated events in autumn 2010 and spring 2011. It will be referred to as ***2010Realistic*** in the following.

The drawback of the strategy is that modules which did not get aligned in data, remained at the starting geometry which is the designed position in the simulation. While these modules probably have a strong misalignment in data and thus result in a larger normalized χ^2, the same modules are at the optimal position for the 2010Realistic-scenario and thus do not broaden the distribution of the normalized χ^2 in a representative way.

5.3.1 Known differences between data and simulation and their consequences for alignment

Due to the not yet completely understood nature of minimum bias events, there were some differences observed between the simulated events and the corresponding data. A qualitative comparison of collision events can be taken from a study analysing recorded minimum bias events at a centre-of-mass energy of 900 GeV end of 2009 [9]. Observed differences in some basic tracking quantities between data and simulation are shown in figure 5.5. In the data the number of tracks per event was slightly higher than in the simulation. The number of short tracks with less than ten valid hits was also larger in data; there were more tracks with smaller transverse momenta and the number of tracks in the central region was higher in data as well [9]. The observed differences are mainly due to deficiencies in the simulation of soft QCD processes.

Since the track selection for alignment required a transverse momentum larger than 0.65 GeV and the number of hits per track must exceed 8, most of the differing region is excluded. Nevertheless, when discussing differences between the alignment precision in data and simulation, especially systematic effects, the qualitative differences should be kept in mind. A further difference concerns the module description itself. While in the simulation the modules were assumed to be flat, the studies mentioned in section 3.4.1.2 indicated a non-negligible bow of the sensors in reality, such that the data compatibility for tracks from cosmic rays and minimum bias events in a combined alignment strategy was much larger in simulation than in data. The number of tracks rejected due to a large χ^2 was smaller in the simulation such that it was hardly possible to run on exactly the same composition of tracks from cosmic rays and collisions in data and in simulation. In addition there was no time dependence of the pixel half-shell positions simulated.

5.4 Alignment results

To validate the quality of the achieved alignment, several validation methods have been developed. In the following section these validation results will be shown going from low level quantities like the residuals themselves to higher level validation results which judge the quality of the alignment on the basis of track parameters or even invariant mass distributions.

5.4.1 Track based validation

A basic check of the quality of the aligned detector geometry is the comparison of the track residuals which have been minimized in the alignment procedure. The validation has been done using tracks from minimum bias events applying the same track selection as for the alignment (see section 5.1.2). To guarantee statistical independence of the data used for the validation, only runs with odd numbers have been chosen while

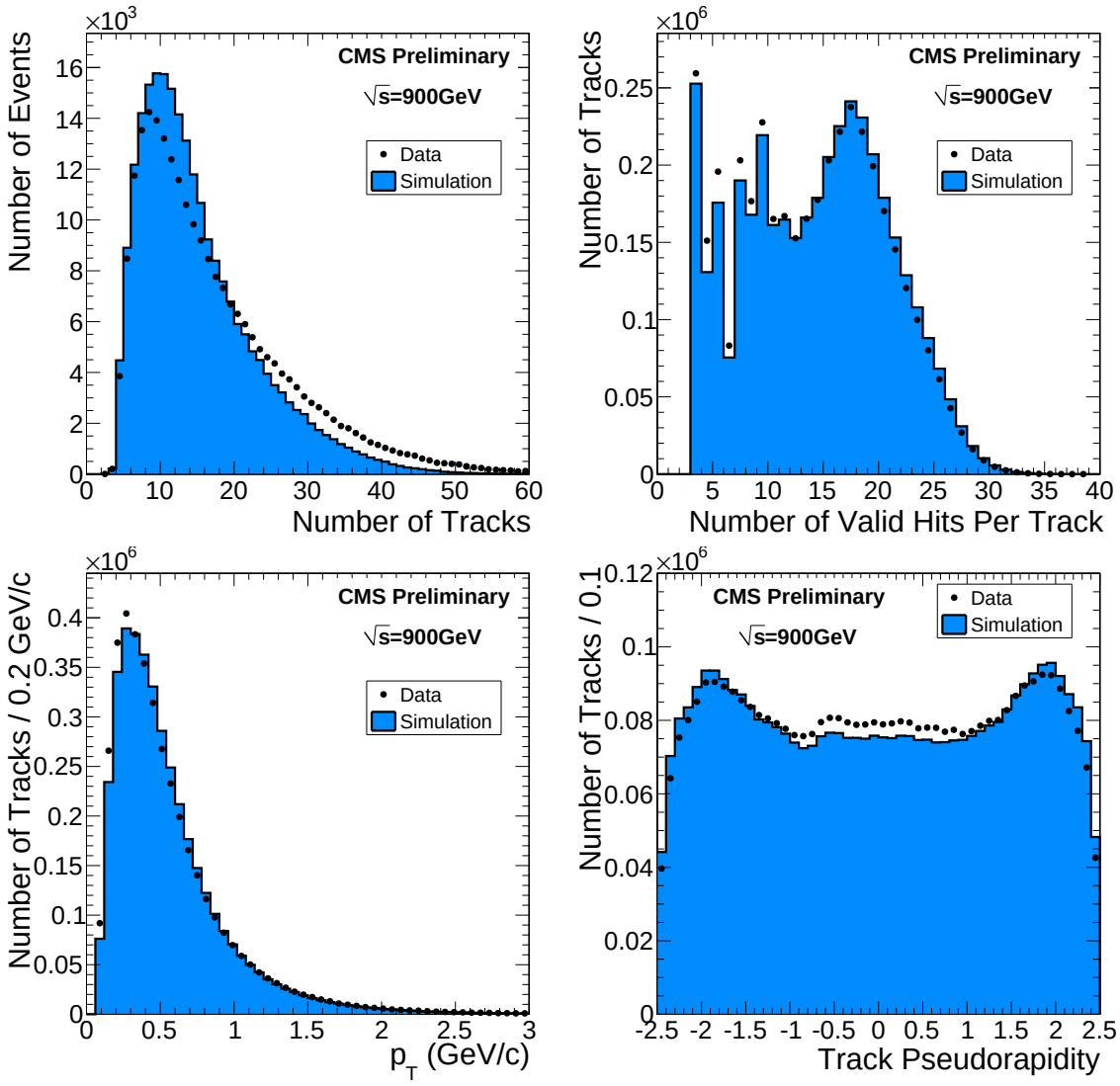

Figure 5.5: Comparison between simulation and data for MinBias events at a centre-of-mass energy of 900 GeV: number of tracks per event (top left), number of valid hits per track (top right), transverse momentum spectrum (bottom left) and pseudorapidity η of tracks (bottom right) [9].

for the alignment only runs with even numbers have been used.

For all modules, the unbiased residual between measured and predicted hit position in local u and v (see section 4.4) has been calculated where unbiased means that the information of the hit under consideration has not been used for the track prediction. Instead of directly plotting the local u and v residuals, local coordinates u' and v' are considered in the track based validation. They are defined such that they are parallel to u and v, but the direction is always chosen to be in positive ϕ, z, or r directions, irrespective of the orientation of the local coordinate system. For the TID and TEC

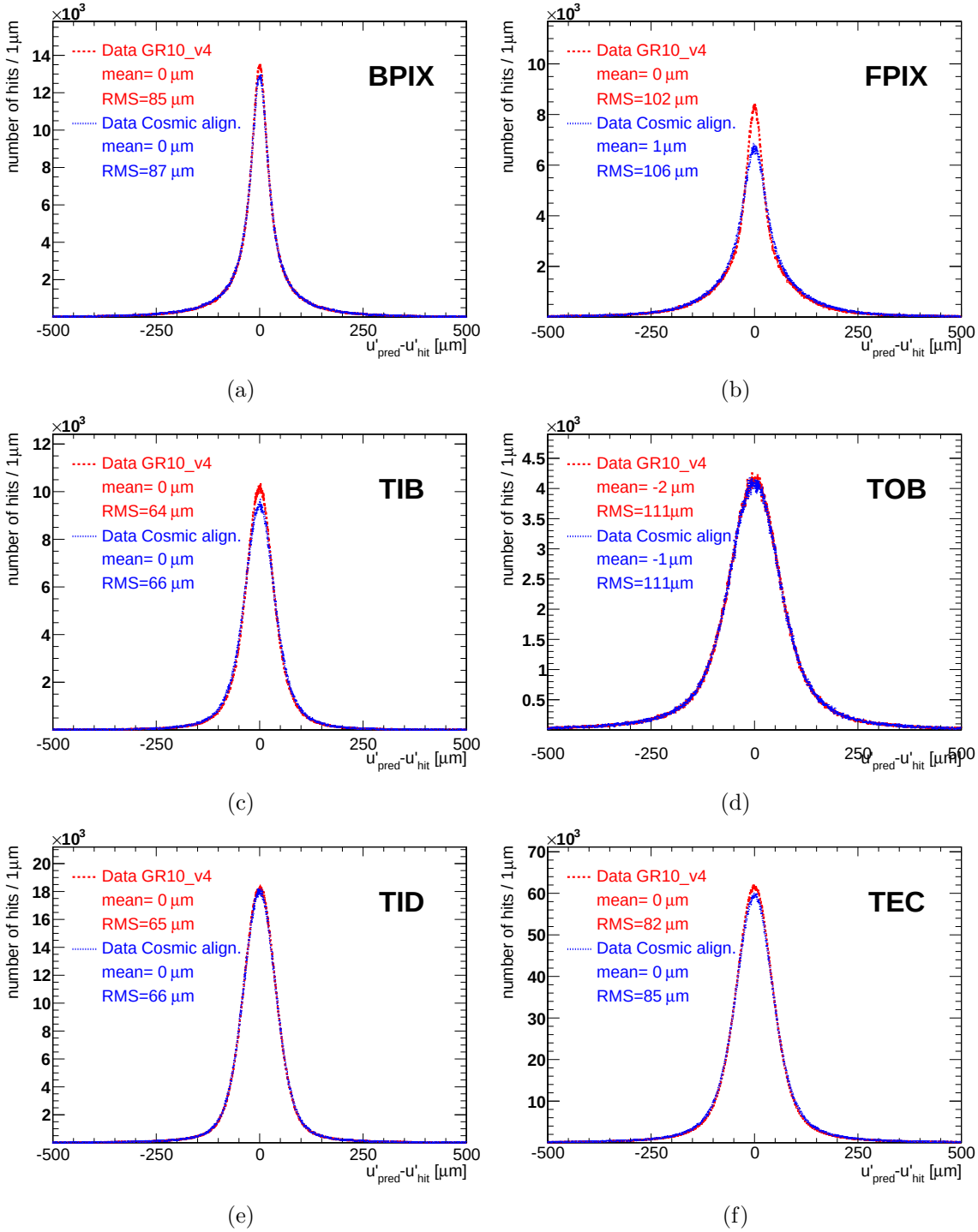

Figure 5.6: Residual distributions of the local u' coordinate for an alignment using tracks from cosmic rays only (blue dashed line) and the combined 2010 alignment *GR10_v4* using tracks from cosmic rays and collision data (red dotted line) validated on MinBias events.

wedge-shaped sensors, where the topology of the strips is radial, the u'- and v'-axes change direction across the sensor such that v' is always directed along the strips and, therefore, u' corresponds to the global rϕ-coordinate. In addition to the individual residual distributions on module level, the distributions are also summed up and stored for the different hierarchy levels, to enable both a detailed validation of single modules and an overall performance comparison for the different subdetectors [9]. Figure 5.6 shows the summary histograms of the residual distributions in local u' for the individual subdetectors, comparing the data aligned using the combined strategy *GR10_v4* described in section 5.2 to the previous geometry based on an alignment using only tracks from cosmic rays.

Since the residual distributions are already dominated by random effects like multiple scattering, the width of the residual distribution itself is not a meaningful measure of the alignment precision. Therefore, the median of the residual distribution is used to judge and compare the quality of different alignments. Figure 5.7 and 5.8 show the distributions of the median of the residuals (DMR) on module level for each subdetector.

The quoted mean value can be interpreted as the average shift or displacement of the module positions – for a well aligned detector it is supposed to be zero. The width of the distribution (here the root mean squared (rms)) gives an estimate on the achieved alignment precision. They are summarised in table 5.2.

Subdetector	**DATA Cosmic align. RMS [μm]**	**DATA GR10_v4 RMS [μm]**	**Simulation Design RMS [μm]**
BPIX u'	5.2	1.2	1.0
BPIX v'	18.5	3.9	2.3
FPIX u'	20.8	3.6	1.5
FPIX v'	22.8	4.3	2.1
TIB u'	6.6	2.8	3.2
TOB u'	8.9	8.1	7.3
TID u'	6.0	2.2	2.2
TEC u'	13.6	5.2	3.8

Table 5.2: RMS values of the distribution of the median of the residuals validated on minimum bias events in data and simulation.

These distributions show the strong impact of collision data on the alignment precision in the forward region of the detector, comparing the *GR10_v4* alignment to the one based on tracks from cosmic rays only. The latter can be demonstrated more explicitly by plotting the rms values of the median distributions depending on the η-range. Figure 5.9 shows the improvement of the alignment precision from the non-aligned detector to an alignment using cosmic rays only and finally to the combined 2010 alignment *GR10_v4*. The largest improvement between the two alignments can be found in the high η region where the tracks from collisions had the strongest impact.

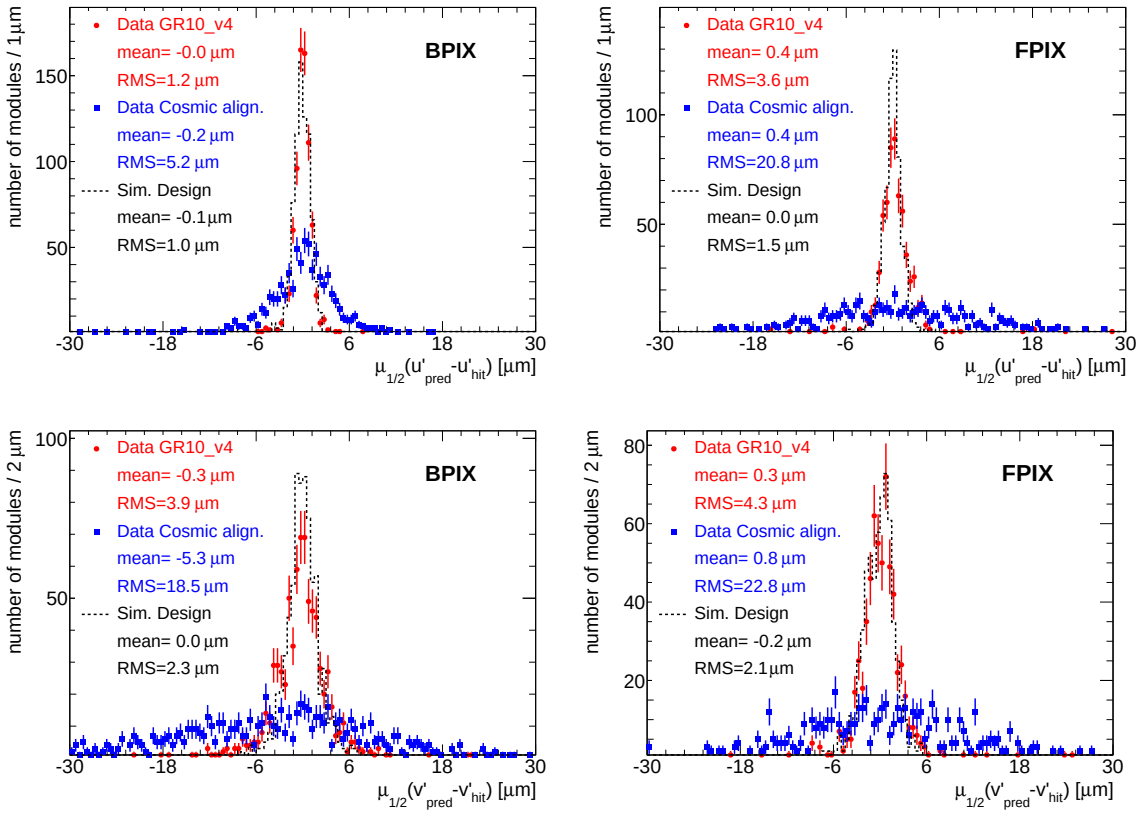

Figure 5.7: Distribution of the median $\mu_{1/2}$ of the residuals in local u' and v' for the pixel detector comparing the data using the run range dependent alignment *GR10_v4* (red dots) and an alignment based on the usage of tracks from cosmic rays only (blue rectangles) to the simulation using design geometry (dashed black) validated on MinBias events.

The forward region was also the region where the alignment precision has not yet reached the ideal conditions in simulation. Apart from remaining misalignment, this might be an effect of the improper surface description within the CMSSW software. The modules in the forward direction were hit under a larger impact angle from the tracks from the collision point and were thus more influenced by the deviation from the module flatness and the corresponding improper error assignment (see section 3.4.1.2). The same argument holds for the TOB although it only covers an η range up to 1.2. Figure 5.10 shows that the alignment precision in the barrel region of the TOB already reached the design performance after the alignment with tracks from cosmic rays only and for large values of η the inclusion of tracks from collisions could not improve the alignment precision further.

Besides the pixel detector, the TEC profited most from the combined alignment using collision tracks in addition to the tracks from cosmic rays. The usage of tracks from cosmic rays allowed an alignment precision of about 10 μm, due to the poor

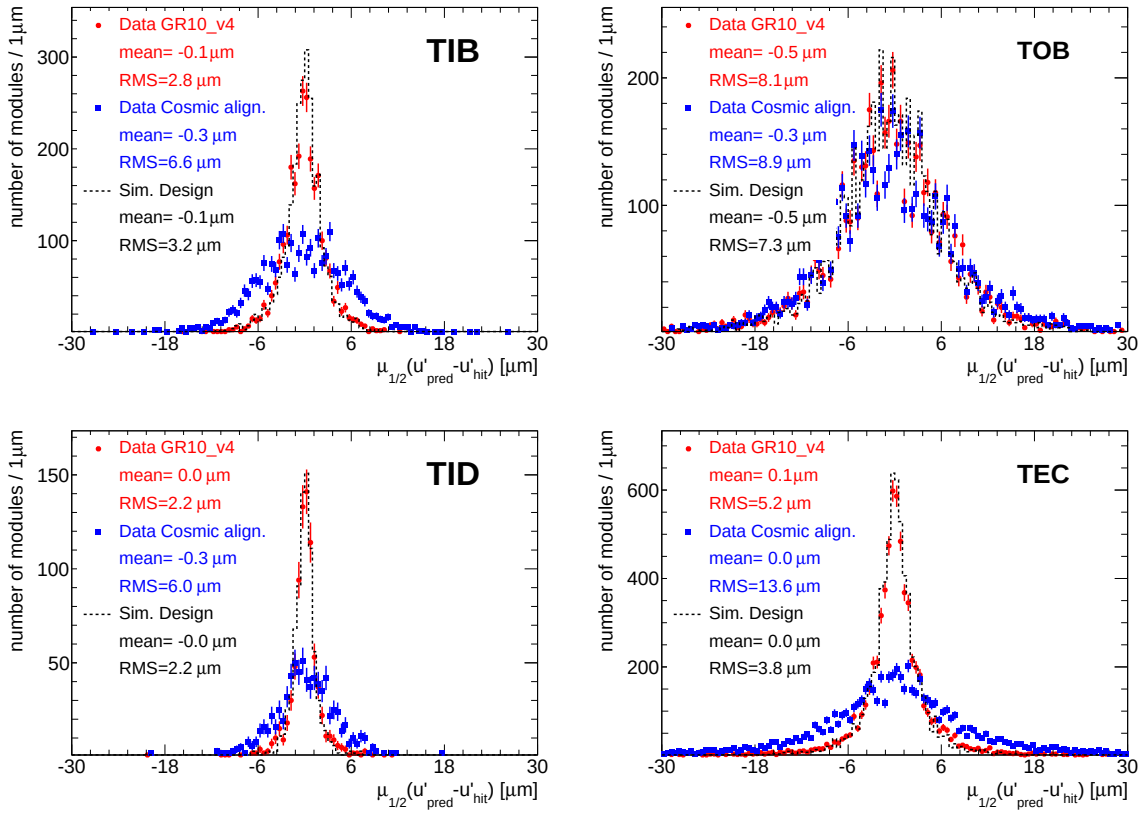

Figure 5.8: Distribution of the median $\mu_{1/2}$ of the residuals in local u' for the strip tracker comparing the data using the run range dependent alignment *GR10_v4* (red dots) and an alignment based on the usage of tracks from cosmic rays only (blue rectangles) to the simulation using design geometry (dashed black) validated on MinBias events.

illumination and the small impact angle of tracks mainly passing the detector horizontally. Including the tracks from collisions the precision could be further reduced to be compatible with the design precision achieved in simulation.

Overall the alignment precision after 2010 is no longer limited statistically and further alignments will concentrate on on the constraint of weak modes that might have been introduced artificially in former alignments. Since weak modes influence the track parameters in a correlated way but not affect the individual residual distributions, the validation presented so far would not be sensitive to detect them.

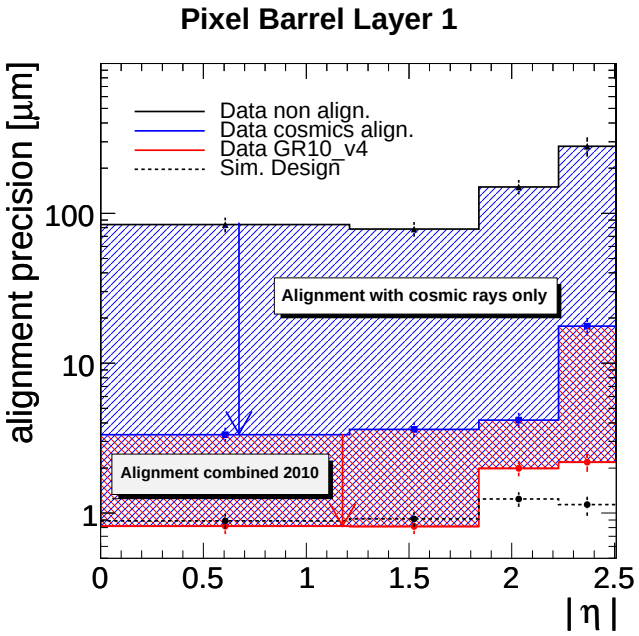

Figure 5.9: Improvement due to alignment on the width (rms) of the median distribution of the residuals in local u' as function of $|\eta|$ for pixel barrel layer 1 for an alignment basing on cosmic rays only, the combined 2010 alignment *GR10_v4* and a perfectly aligned detector in the simulation validated on MinBias events.

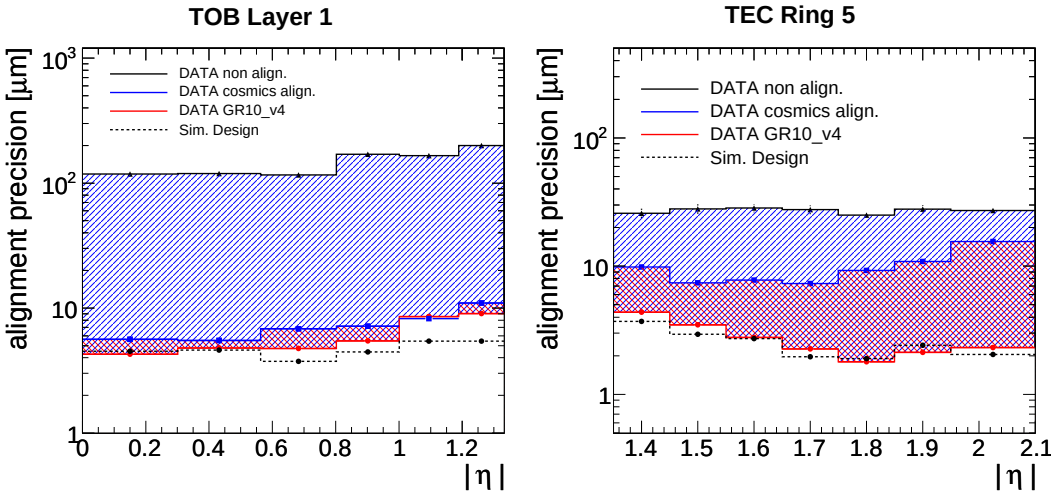

Figure 5.10: Improvement due to alignment on the width (rms) of the median distribution for local u' as a function of $|\eta|$ for the rϕ-modules of TOB layer 1 and TEC ring 5 for an alignment basing on cosmics only, the combined 2010 alignment *GR10_v4* and a perfectly aligned detector in the simulation.

5.4.2 Track splitting validation

In addition to the validation of the local alignment precision based on the residual distributions as discussed in the previous section, the track quantities as seen and used by physics analyses need careful validation. They can help to spot weak modes which hardly change the tracks χ^2. Therefore, the track parameter resolutions have been validated by selecting long tracks from cosmic rays that get split into an upper and lower leg. After an independent reconstruction of the two legs with the geometry under consideration, the track parameters at the point of closest approach to the nominal beamspot are compared. To mimic the topology of collision events, the upper and lower track segments must have at least three pixel hits [56]. Figure 5.11 shows the differences between the track parameters of the upper and lower track segment measured at the point of closest approach to the beamspot and scaled by $1/\sqrt{2}$. While the difference of the impact parameter in the transverse direction Δd_{xy} shows the same performance for the two curves in data, the impact of the pixel half-shells movement that is not covered by the alignment using tracks from cosmic rays only is clearly visible for the distribution of the impact parameter difference in longitudinal direction Δd_z which is broadened with respect to the distribution for *GR10_v4*. The movement also results in an overall shift of $\Delta\theta$-distribution while the difference in the track azimuthal angle $\Delta\phi$, in the transverse momentum Δp_T and the related curvature $\Delta 1/p_T$ are not affected.

Apart from the absolute differences seen in the track parameters the resolution of the parameters is of interest. The normalised track parameter distributions can be used to judge on the quality of the errors assigned to the alignment position (APE).

For the alignment using tracks from cosmic rays only, the assignment of the corresponding errors was mainly driven by the different illumination of the modules depending on the subdetector. Only for TIB and TOB the errors were assigned layerwise. The same value r_0 for all three spatial direction was chosen and each module was given the radius $r_{sphere} = r_0/\sqrt{N_{entries}}$ representing the APE. For those modules with only few or no entries the value for r_{sphere} has been restricted to a reasonable value corresponding to a precision compatible to survey and assembly measurements [56]. Due to track topology of cosmic rays, the resulting APE values showed a ϕ-dependence as with larger values for modules around $\phi = 0$ and $\phi = \pi$.

For the time dependent alignment using cosmic rays and collision tracks, the smallest APE value per layer was assigned to all modules in the barrel of the tracker since tracks from the collision point are ϕ symmetric. In the forward region the APE values remained unchanged and thus dependent on the illumination of cosmic rays. For the pixel endcaps a fixed value of 30μm was chosen [60]. The tuning of alignment positioning errors was performed with the aim of having normalized residual distributions centred around zero and with a width of one for the correct errors assignment. Figure 5.12 shows that this is only partially fulfilled. Δd_z and Δd_{xy} are primarily sensitive to the pixel. While the new errors lead to an improvement of the normalized Δd_z-distribution, they slightly underestimate the errors in the transverse plane such

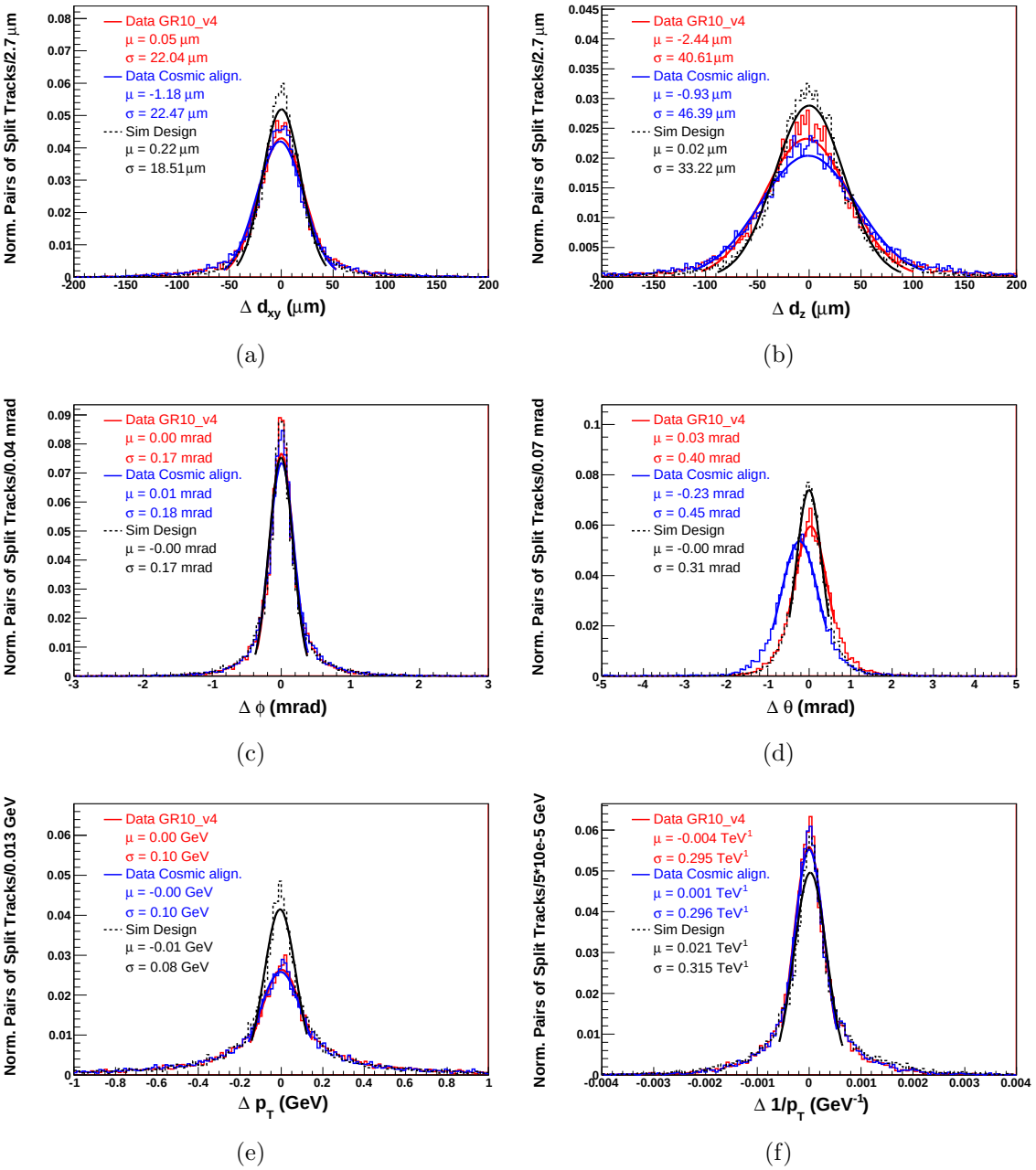

Figure 5.11: Track parameters are shown for three geometries: realistic misalignment scenario in simulation (solid black), data aligned with cosmic rays only (red solid line), data using the combined 2010 alignment *GR10_v4* (dashed purple line) validated on tracks from cosmic rays taken during collisions.

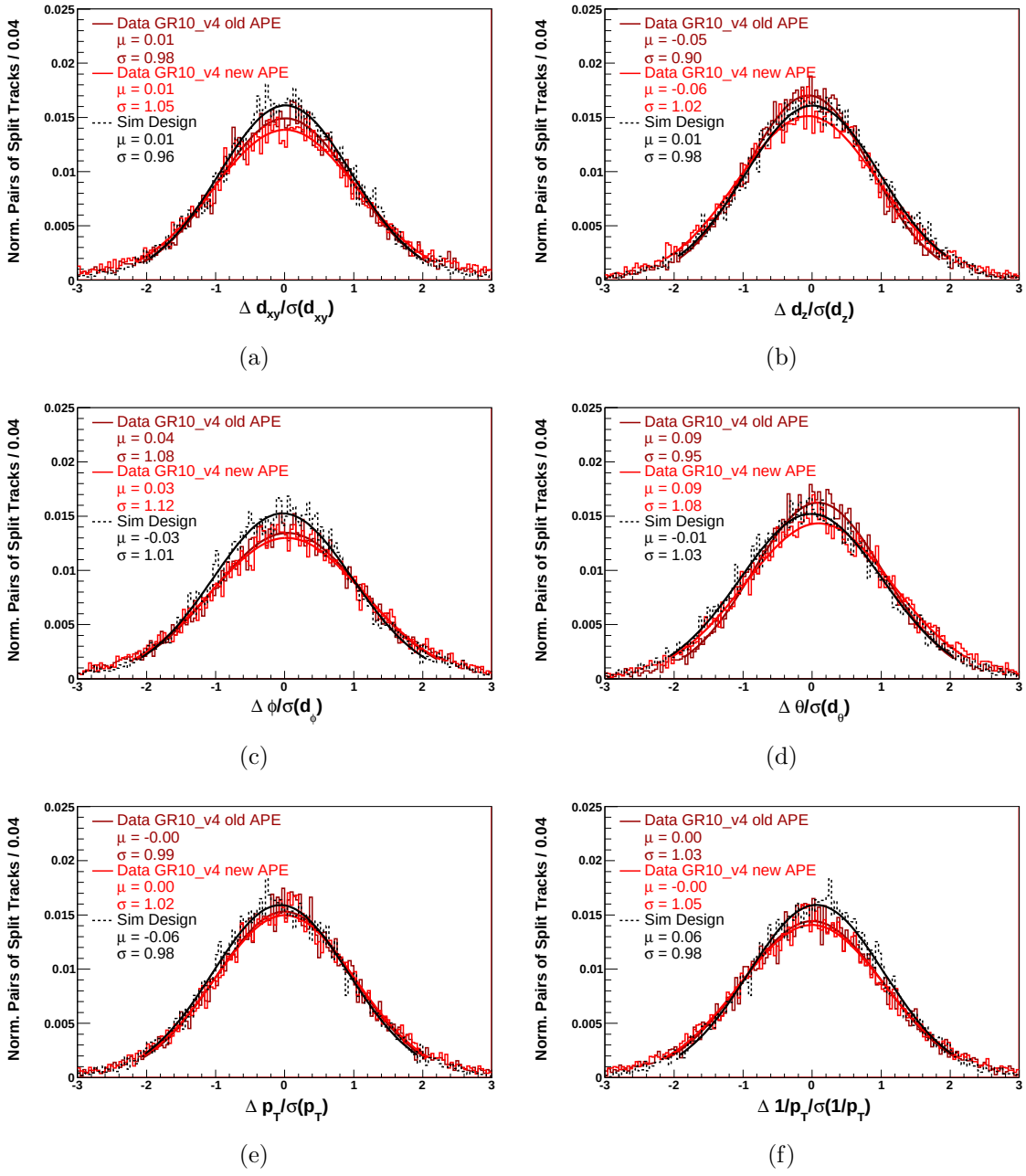

Figure 5.12: Normalised track parameters distributions shown for GR10_v4 with old APE (dark red), GR10_v4 with new APE (red) and ideal geometry in simulation (dashed black)

that the width of the Δd_{xy}-distribution becomes slightly broader than one whereas a comparison with the design specification in simulation shows that the width is slightly smaller than one. By combining tracks from cosmic rays and collision the alignment becomes so precise that non-alignment related effects begin to dominate the errors and the module deviation from flatness has a non-negligible impact. Thus further tuning of the APEs requires a proper description of the modules including kinked and bowed sensors.

5.4.3 Data quality monitoring over time: Primary vertex validation

To monitor the alignment quality in the pixel detector over time, a validation procedure based on the primary vertex (PV) location is used. For all tracks originating from a PV, the PV is refitted using all tracks except one probe track as illustrated in figure 5.13. Residuals are evaluated with respect to the unbiased refitted PV and plotted versus the probe track parameters in different bins of η, ϕ and the transverse momentum to spot degradations of the alignment. Figure 5.14 shows the distribution for data and for an artificially distorted pixel geometry with the half-shells moved apart by $\pm 30\,\mu$m (black solid dots) along z as an example. The pixel half-shell movement in the simulation has no impact on the transverse impact parameter d_{xy} as a function of ϕ but the longitudinal impact parameter d_z as a function of ϕ is strongly affected. The red curve also shown in these plots corresponds to the validation in data using the geometry aligned with tracks from cosmic rays only, validated on the first

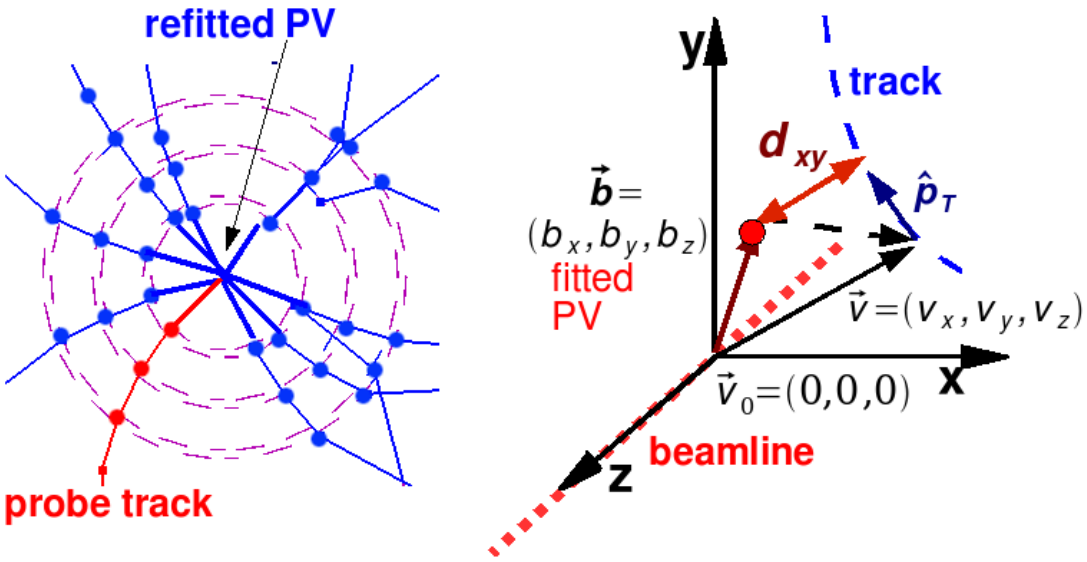

Figure 5.13: Left: The primary vertex is refitted including all tracks except the probe track. Right: Residuals of the probe track parameters with respect to the unbiased vertex [58].

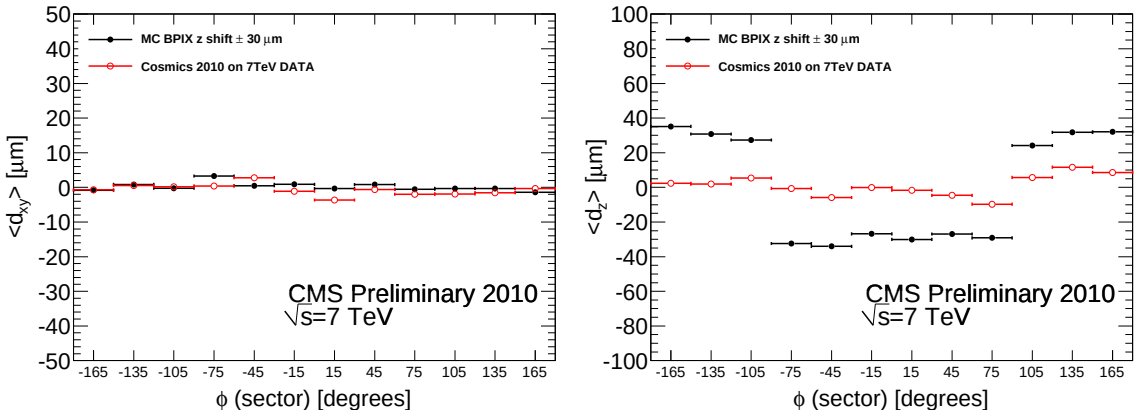

Figure 5.14: Primary vertex validation: Mean of the residuals of the track parameter d_{xy}/d_0 (left) and d_z (right) in bins of η_{track} for first collision data (red open circles) and simulated data with manipulated detector geometry [58].

collision events taken at a centre-of-mass energy of 7 TeV. Since there are no effects visible for the data, the pixel geometry has been stable between February 2010 and the beginning of collision data taking end of March 2010.

The PV validation is run on a daily bis and the only severe time dependence observed has been a relative movement of the two pixel half-shells along z. It has occurred several times with total differences of the z positions of the two pixel half-shells between 20 and 70 μm. Figure 5.15 shows the PV validation for two random dates within the data taking period in 2010. For the data taken on August 9, 2010 there is no separation visible, while the data taken on October 28,2010 shows a clear separation of the pixel half-shells. A connection with the cooling can not be excluded and would deliver an explanation for the sign flip after each technical stop as the pixel was cooled down to $-10°$ during each technical stop but operated at higher temperatures during LHC operation.

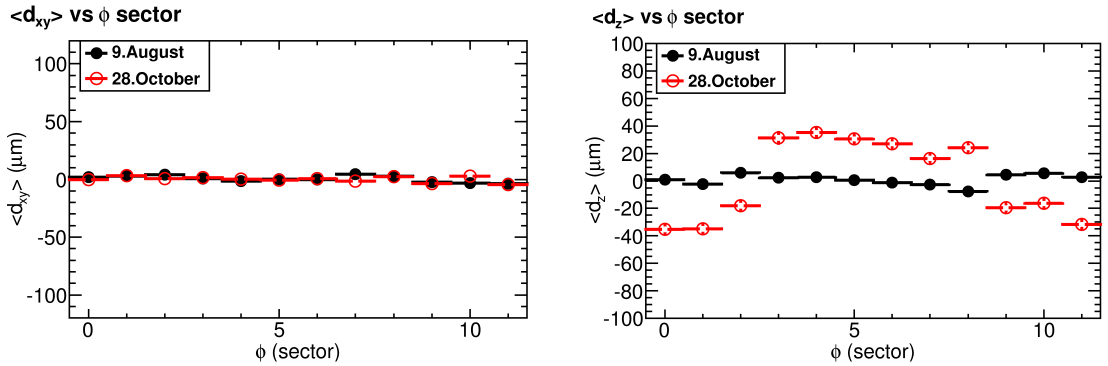

Figure 5.15: Primary vertex validation: Mean of the residuals of the track parameter d_{xy}/d_0 (left) and d_z (right) in bins of η_{track} for data taken at 9.August (black dots) and 28.October (red open circles).

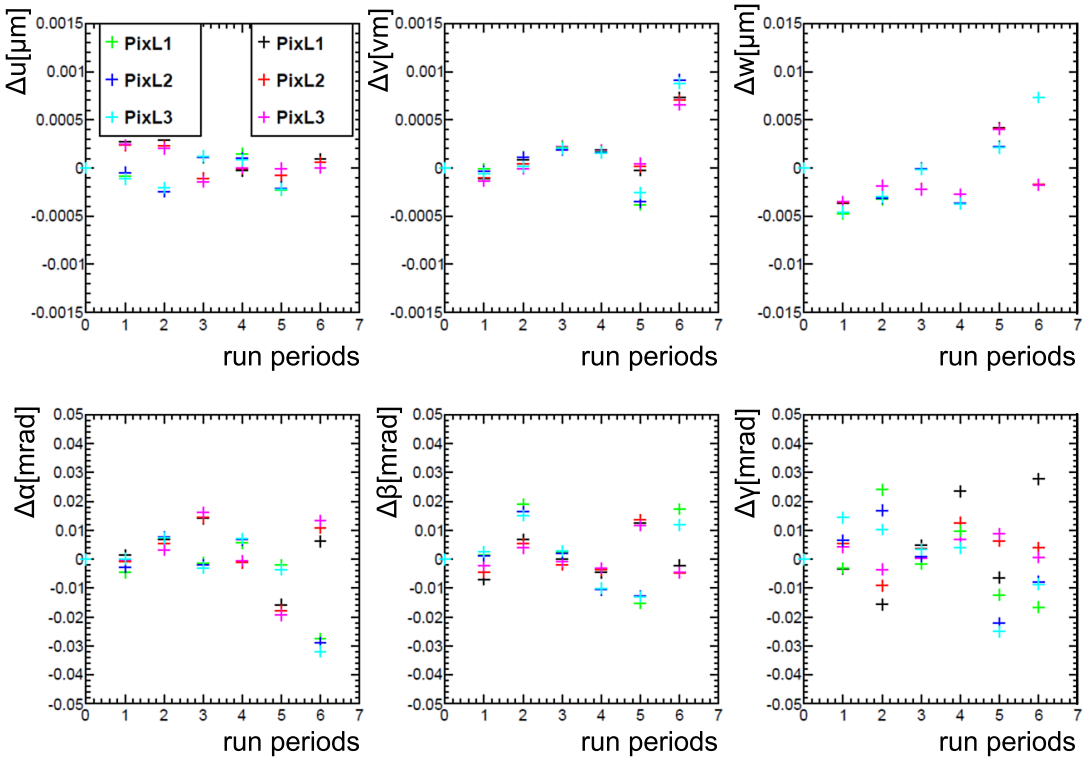

Figure 5.16: Difference of the alignment corrections for all 6 degrees of freedom determined by Millepede for the pixel half-layer.

Figure 5.16 shows the differences between the parameters determined by Millepede for the pixel half-layers for all six degrees of freedom. The w parameter corresponds to a correction in global z direction and is one order of magnitude larger than the corrections for the other translations in u and v. In v the layers of the pixel half shells move almost coherently while for the other coordinates, especially for the γ-angle, the corrections per layer differ up to 20 μrad.

To summarise the z-separation of the pixel half-shells over the whole run range in 2010 a trend plot has been extracted from the daily validation by fitting a constant function to the distribution of d_z as a function of ϕ for each half-shell; the difference has been displayed as a function of time. Figure 5.17 has been produced using an alignment 'Summer 10 Tk Geom.' that does not correct the pixel movement and the alignment presented in this thesis *GR10_v4* which is referred to as 'Fall 10 TK Geom.'in the plot [61].
A comparison between the results before and after alignment shows that the separation in z-direction of the two pixel half shells has been corrected for the seven run ranges. The remaining separation between the two pixel half-shells within the defined run intervals scatters within a range of 15 μm.

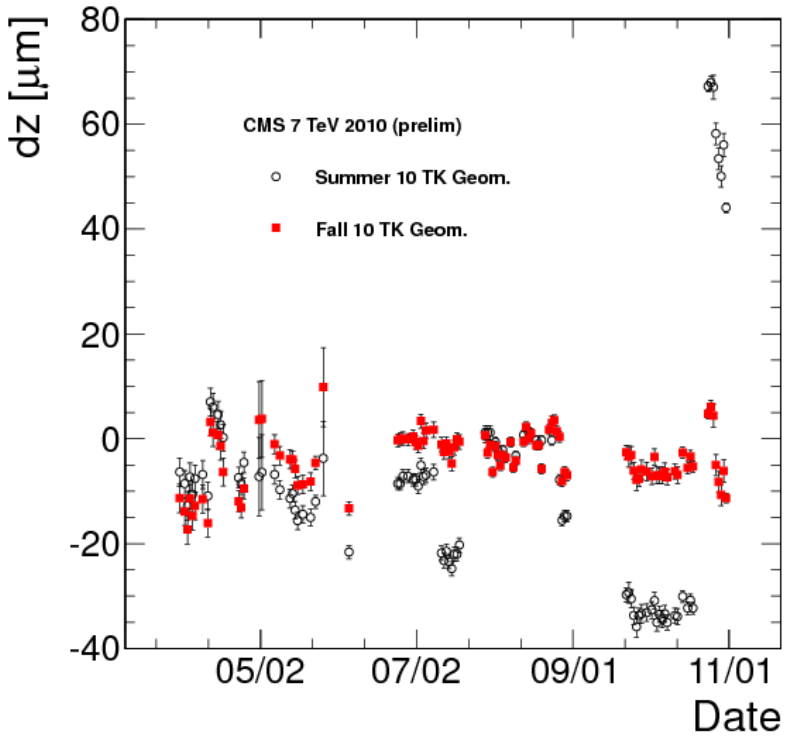

Figure 5.17: Trend plot of the z-separation of the pixel half-shells taken from the primary vertex validation over the run period [61] before (black open circles) and after alignment (red solid dots).

5.5 Summary of the alignment results

The overall local alignment precision achieved with the combined alignment *GR10_v4* using tracks from cosmic rays and collision tracks meets the design specifications for most regions of the CMS tracker. The width of the median of the residual distributions per all subdetector is within 1μm to the design performance for the most sensitive coordinate u. With the precision achieved, the validation methods presented so far become sensitive to non-alignment related effects. In addition, movements of detector substructure over time have been monitored and corrected.

To study the impact of alignment related effect on physics variables, three studies will be presented in the next chapter. First the impact of the observed pixel half-shell movements on the b-tagging performance will be investigated to estimate whether the differences in Δz have been sufficiently corrected or whether even finer time intervals need to be chosen for which the pixel positions have to be determined.

In a second part the impact of weak modes on the physics performance will be discussed using the Z boson resonance.

Chapter 6

Impact of alignment on physics performance

As shown in the previous section, the alignment precision achieved with the combined alignment in 2010 using tracks from cosmic rays and collisions reaches the design precision in simulation in most parts of the detector. In the first part of this chapter the impact of the observed movements of the pixel barrel half-shells on the b-tagging performance are investigated using simulated events in order to study whether the achieved precision of the large structures in the pixel is sufficient.
Besides the monitoring of the alignment stability over time, future alignment activities will concentrate on correlated detector distortions, which are not or only weakly influencing the overall χ^2. In order to detect these distortions external information is needed, for example from known particle mass resonances. In the second part of this chapter, the sensitivity of the reconstructed Z boson mass to correlated detector distortions is investigated in data as well as in the simulation.

6.1 B-tagging: Performance and sensitivity studies with respect to misalignment

Due to the long lifetime and hard fragmentation of B hadrons, the jets originating from b quarks can be distinguished from those jets originating from gluons or lighter quarks like u,d and s - the distinction with respect to jets from c quarks is not that pronounced [62]. Within the CMSSW software framework, several algorithms have been implemented to identify jets originating from b quarks, the so-called b-tagging algorithms. They range from simple and robust methods making use of the high fraction of leptons within b quark fragmentation processes up to complex multi-variant techniques extracting lifetime and kinematic information from displaced vertices [62]. After a short introduction of the b-tagging algorithms, the b-tagging performance between data and simulation is compared. The realistic misalignment scenario described in the previous chapter is then used for further studies concerning the impact

of misalignment on the b-tagging performance as a follow-up of the studies presented in [62]. In addition, basic studies concerning the impact of the systematic movements observed in data for the pixel barrel half-shells are presented.

6.1.1 B-tagging algorithms

All b-tagging algorithms produce a single output value that is used to discriminate b jets from other jets. There is no fixed discriminator value to unambiguously tag a b jet, but the value can be chosen depending on the need for efficiency and purity of a specific analysis. Nevertheless there is a common definition of the standard working points for each algorithm defined by the fraction of non-b jets which contaminate the b jet sample estimated from simulation. The working points are labelled: L:(*loose*, 10%) , M:(*medium*, 1%) and T:(*tight*, 0.1%), respectively [11]. The algorithms considered most sensitive to the alignment of the inner tracking system are those relying on the information related to the vertices reconstructed in an event.

6.1.1.1 Impact parameter

One powerful observable in this context is the distance between a track and the primary vertex at their point of closest approach: the impact parameter. Figure 6.1 illustrates the main characteristics of a B hadron decay within a jet. The long lifetime of B hadrons, about τ_B ∼1.6 ps, allows the hadron to propagate a typical length of $c \cdot \tau_B$ ∼500 μm (for $\gamma\beta = 1$) before it decays. The charged particles produced in this decay have tracks with large impact parameters (IP) with respect to the primary vertex [10]. The impact parameter can either be computed in the transverse plane or in all three dimensions. In both cases the computation starts from the particle trajectory parameters at the innermost measurement point. While the extrapolation to the point of closest approach with respect to the vertex can be done analytically and thus in one step for the transverse impact parameter, the extrapolation in three dimensions has to be performed iteratively. Figure 6.2 illustrates the main steps performed to compute the impact parameter. In the first step, the point S of closest approach of the track to the jet axis is extracted and a tangent to the trajectory curve at this point is projected. This linear extrapolation allows the computation of the minimal distance of the track to the primary vertex (V), the impact parameter. The distance VQ from the vertex to the point Q, which lies on the jet axis and is closest to the track, is an approximation of the flight path of the B hadron before it decayed. Hence, it is referred to as *decay length* [10].

The impact parameter can either be signed positive or negative, depending on the scalar product between impact parameter and jet direction. As the jet direction approximates the flight direction of the B hadron, a positive sign means that the decay occurred downstream the jet, a negative sign that it occurred upstream. Therefore, the impact parameter for tracks from a b decay are expected to be positive. However, poorly measured track parameters, badly reconstructed jet directions or primary vertices can lead to a sign flip of the impact parameter [10].

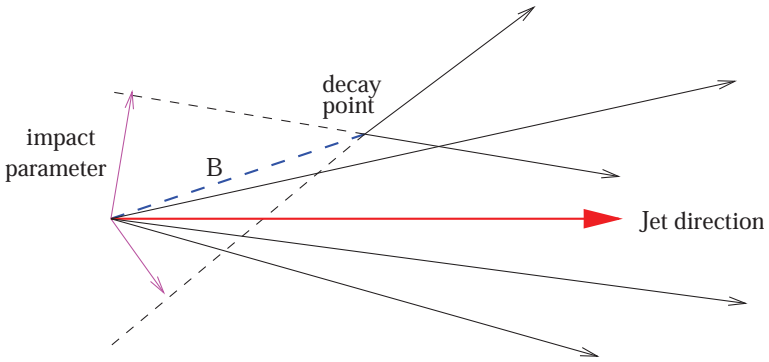

Figure 6.1: Characteristic topology of a jet originating from b quark [10].

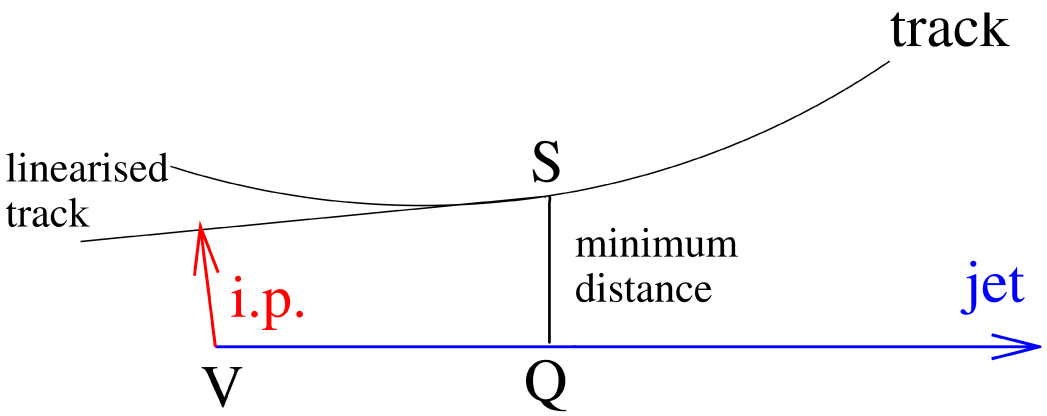

Figure 6.2: Schematic of the impact parameter computation [10].

The distribution of the impact parameter of tracks originating from the primary vertex is thus supposed to be centred symmetrically around zero.
Given that the uncertainty on the impact parameter varies with the number of measurements and that this uncertainty can be of the same order of magnitude as the impact parameter itself, the impact parameter significance $\frac{IP}{\sigma_{IP}}$ is chosen as a more reliable observable. For tracks from the PV it should approximately follow a Gaussian distribution with width 1.

6.1.1.2 Validation of b-tagging Observables in Early Data

The two algorithms mainly based on the information of the impact parameter significance are the track counting approach (TC) and the jet probability algorithm.

The track counting algorithm flags a jet as b jet if it contains at least N tracks exceeding the parameter significance S. Therefore, the tracks associated with the jet are ordered in decreasing significance and, depending on the need for efficiency or purity, the discriminator value is either the significance S of the second or third track. If it is the significance of the second track, the algorithm is referred to as *track counting high efficiency* (TCHE). If the significance of the third track is chosen, it is referred to as *track counting high purity* (TCHP) [11].

The *jet probability* algorithm also uses the parameter significance as observable. In contrast to the track counting algorithm the discriminator value is not based on the significance of a single track but on the combined information of all tracks associated to the jet. From a sample of tracks with a negative impact parameter value, a probability density function for a track originating from the primary vertex is extracted and then used as input for a likelihood method to calculate the combined probability for all tracks associated to the jet to originate from the primary vertex. Another variant of this algorithm is the *jet b probability* which instead of taking into account all tracks associated to the jet, calculates the probability of the four most displaced tracks to originate from the primary vertex [10] [11].
The third algorithm considered in the following discussion is the *simple secondary vertex* algorithm (SSV). Instead of estimating how likely it is that all tracks within a jet originate from the primary vertex, at least one secondary vertex is explicitly required which naturally limits the maximal efficiency to identify a b jet to the probability of finding a secondary vertex in a weak b decay which is about 60-70% [63]. The three dimensional flight distance or decay length VQ in figure 6.2 serves as discriminator, again defined for a high efficiency version (SSVHE) where two tracks have to be associated to the secondary vertex, and for a high purity version (SSVHP) where three tracks are required [11].
Figure 6.3 shows the comparison of the discriminator values for the different b-tagging algorithms between the first data ($15\,\mathrm{nb}^{-1}$ integrated luminosity) and the simulation using the realistic misalignment scenario at startup described in section 5.3. Differences between data and simulation are small. Even at highest significance, at the 10^{-5}-level of all tracks, data and simulation differ by less than 10% [11].

The good agreement between the performance in data and in simulation concerning the realistic misalignment scenario allows the usage of simulated events to study b tag efficiencies and the estimate of uncertainties arising from movements of the pixel half-shells.

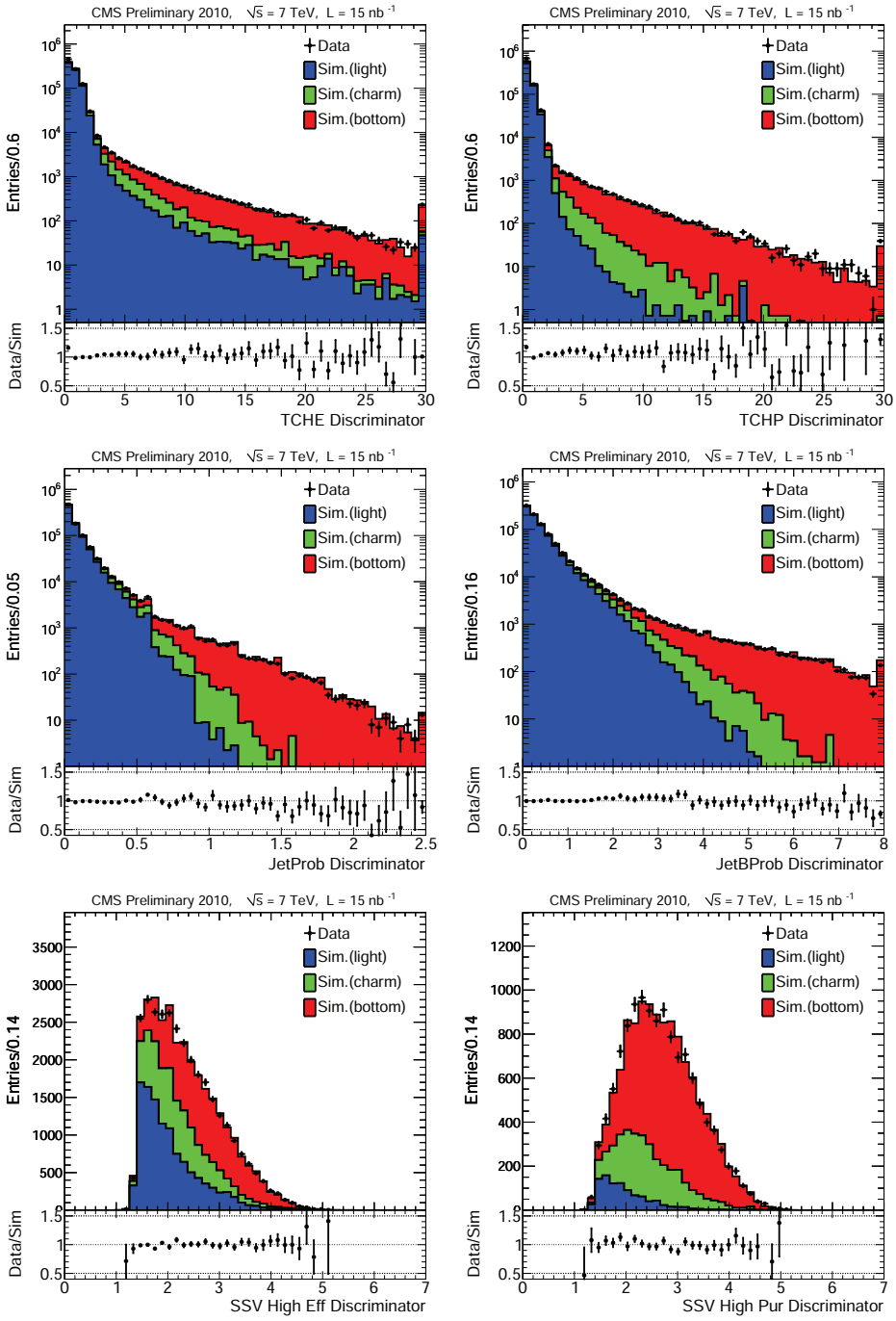

Figure 6.3: Comparison between data and simulation for the b-tagging discriminators: Track Counting High Efficiency (upper left); Track Counting High Purity (upper right); Jet Probability (middle left); Jet B Probability (middle right) and Simple Secondary Vertex High Efficiency (lower left); Simple Secondary Vertex High Purity(lower right) [11].

6.1.2 B-tagging Efficiency Studies in Simulation

The performance of the different b-tagging algorithms is usually displayed as the misidentification rate versus the b-tagging efficiency. To classify the performance of the achieved alignment in data, the corresponding realistic misalignment scenario is compared to the former misalignment scenarios expected to be present after $10\,\mathrm{pb}^{-1}$, $100\,\mathrm{pb}^{-1}$ of data collected by CMS (see [62]) and to a perfectly aligned detector in order to classify the quality of the current alignment. Therefore, the tracks have been refitted with the different tracker geometries and the vertex has been reconstructed with the new track collection as input. The association between tracks and b jets has been repeated as well, mapping the refitted tracks to the particle flow jets before running the standard b-tagging validation sequence. The misidentification rate shown in figure 6.4 only covers jets originating from light quarks u, d and s. Since jets from c quarks are harder to distinguish from jets originating from b quarks, their tagging efficiency behaves similar under changes of geometry and is thus not as useful for this kind of study. Still the corresponding misidentification rates for c quarks can be found in Appendix H.

In [62] the b-tagging performance was studied for different misalignment scenarios to estimate the contribution to the uncertainty on the b-tagging efficiency. Here the study has been repeated using 1.37 million $t\bar{t}$ events simulated with madgraph/Pythia 6, including the developed realistic misalignment scenario *2010Realistic*, next to the $10\,\mathrm{pb}^{-1}$, $100\,\mathrm{pb}^{-1}$ scenarios of former studies. Figure 6.4 shows that independent of the b-tagging algorithm, the performance for the realistic misalignment scenario is equivalent to that of a perfectly aligned detector. The statistical precision of the current alignment in data can thus be considered fully sufficient for efficient b-tagging and uncertainties arising from remaining misalignment are negligible when compared to other effects influencing the b-tagging performance like jet energy scale corrections. Even though this result could be expected as the alignment precision shown in the last chapter was close to the design precision, the study shows that possible biases, introduced, for example, by tracks from cosmic rays and their non-uniform ϕ-distribution, do not have a significant impact on the b tag efficiency. Further studies quantifying the impact of systematic misalignments in data, using, for example, a tag and probe method are beyond the scope of this thesis.

6.1.3 B tagging Sensitivity to Pixel Half-shell Movements

In section 5.2 it was shown that during the run period 2010, the pixel half-shells moved independently of each other along the global z direction, leading to separations of the two half-shells in Δz of up to $70\,\mu$m. Even after the alignment of the pixel half-shells for the different run periods separations of up to $15\,\mu$m are visible. To study the impact of these separation on the b-tagging performance, the design detector geometry was taken and the pixel half-shells were moved apart along the global z direction by $\pm\,10\,\mu$m, $\pm\,20\,\mu$m, $\pm\,40\,\mu$m and $\pm\,80\,\mu$m. The large values were chosen to test the impact on the b-tagging efficiency in the prompt reconstruction, where

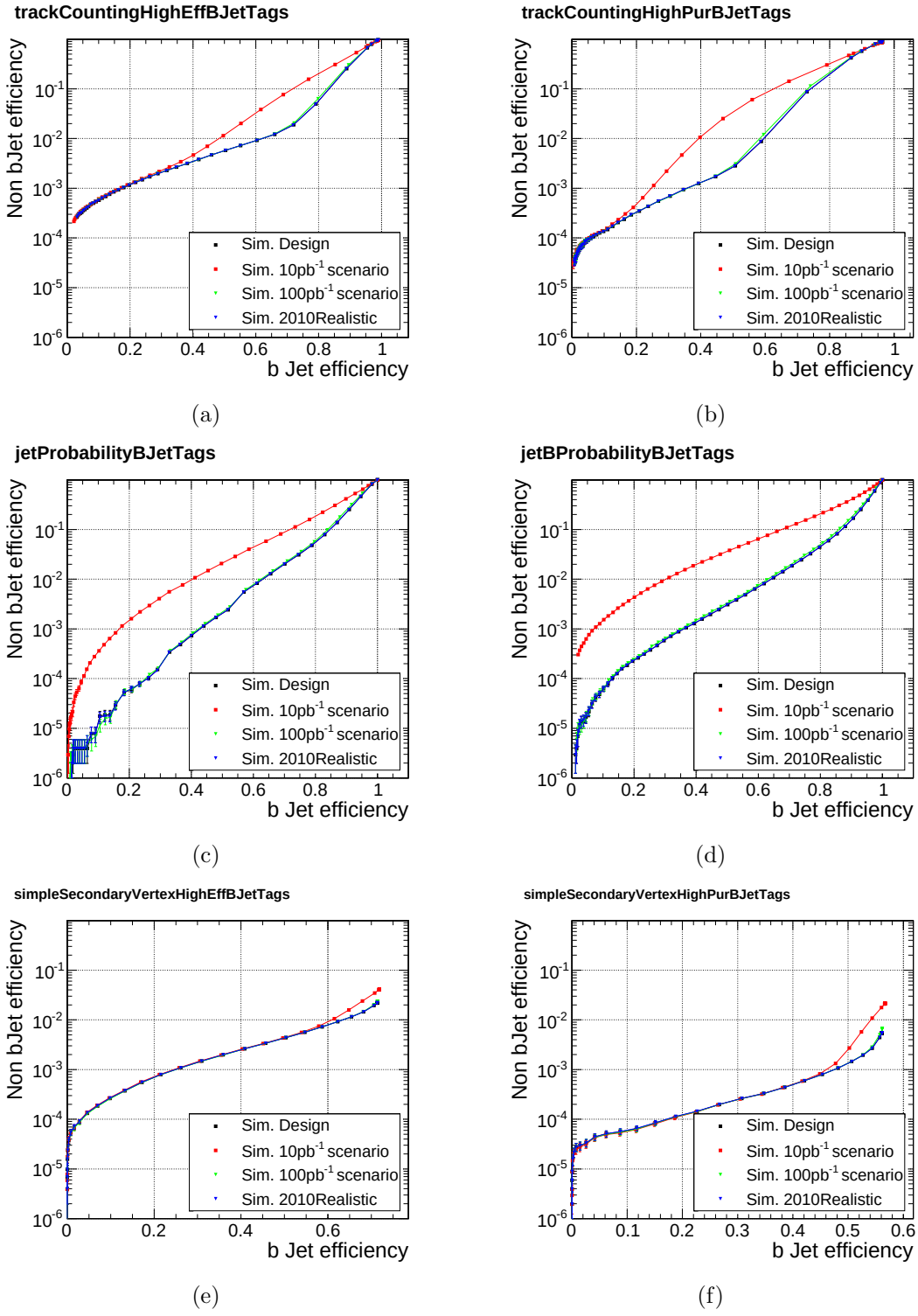

Figure 6.4: Mistag vs b-tagging efficiency for TCHE (a), TCHP (b), jet probability (c), jet b probability (d), SSVHE (e) and SSVHP (f) for different misalignment scenarios.

Geometry \ Algorithms		IDEAL	$\pm 10\mu$m	$\pm 20\mu$m	$\pm 40\mu$m	$\pm 80\mu$m
TCHE	L	0.82	0.82	0.82	0.81	0.77
	M	0.67	0.67	0.66	0.65	0.57
	T	0.19	0.19	0.19	0.19	0.19
TCHP	L	0.73	0.73	0.73	0.71	0.68
	M	0.60	0.60	0.59	0.56	0.49
	T	0.43	0.43	0.43	0.42	0.34
jetBProb	L	0.87	0.87	0.86	0.85	0.76
	M	0.66	0.66	0.65	0.63	0.47
	T	0.42	0.42	0.41	0.39	0.23
jetProbB	L	0.85	0.85	0.84	0.83	0.77
	M	0.64	0.64	0.63	0.62	0.52
	T	0.43	0.43	0.43	0.42	0.31
SSVHE	L	–	–	–	–	–
	M	0.63	0.63	0.63	0.63	0.63
	T	0.25	0.25	0.25	0.25	0.25
SSVHP	L	–	–	–	–	–
	M	–	–	–	–	–
	T	0.48	0.48	0.48	0.48	0.48

Table 6.1: B tag efficiencies at working points for displaced pixel half-shells.

$\pm 40\,\mu$m is a realistic value since total separations of Δz=70 μm have been observed in data already (see the last run period in figure 5.17); $\pm$ 80 μm is a very pessimistic choice. The corresponding b-tagging efficiency is shown in figure 6.5. Compared to the previous plots in figure 6.4, the y axis is zoomed in covering the working points explained in section 6.1.1. A significant impact can only be observed for displacements of the pixel half-shells of at least 40μm. The b-tagging performance for a geometry with a separation of the pixel half-shells in Δz of about $\pm 10\,\mu$m as it was still observed in data for the first data taking period after the time dependent alignment of the pixel half-shells (see figure 5.17) is compatible with the performance gained when using the design geometry. The impact on the performance for displacements of the pixel half-shells of $\pm 40\,\mu$m and $\pm 80\,\mu$m differed for the different b-tagging algorithms. The most robust b-tagging algorithm concerning the pixel movements is the simple secondary vertex algorithm as shown on the bottom of figure 6.5. Since the tracks pointing to the secondary vertex are coherently moved as long as they point into the same half-shell, no sensitivity is expected even for large separations in Δz. The TCHE approach shows a larger sensitivity to the pixel half-shell displacements for the loose working point at 1% mistake rate, while the medium and tight working points are almost unchanged.

Table 6.1 shows the quantitative comparison of the b-tagging efficiency at the three working points L, M and T for the different geometries with displaced pixel

half-shells along z. Below a displacement of $\pm 20\,\mu$m, there is no impact on the b-tagging efficiency. Even the most sensitive algorithm, the jet probability approach, only shows an efficiency drop of 1-2% (2-9%) for a separation of the pixel half shells of $\pm 40\,\mu$m ($\pm 80\,\mu m.$).

The study shows that the remaining displacements in Δz of the pixel barrel half-shells in data after the run dependent alignment shown in figure 5.17 of up to $15\,\mu$m should not influence the b-tagging performance. For the sake of completeness the movements in the other five coordinates, shown in figure 5.16 which were also free alignment parameters, could be added. Still, there might be additional effects in data, for example, due to a worse vertex reconstruction in the presence of pile-up which was not generated in the simulation used for the studies presented above, that might influence the efficiencies.

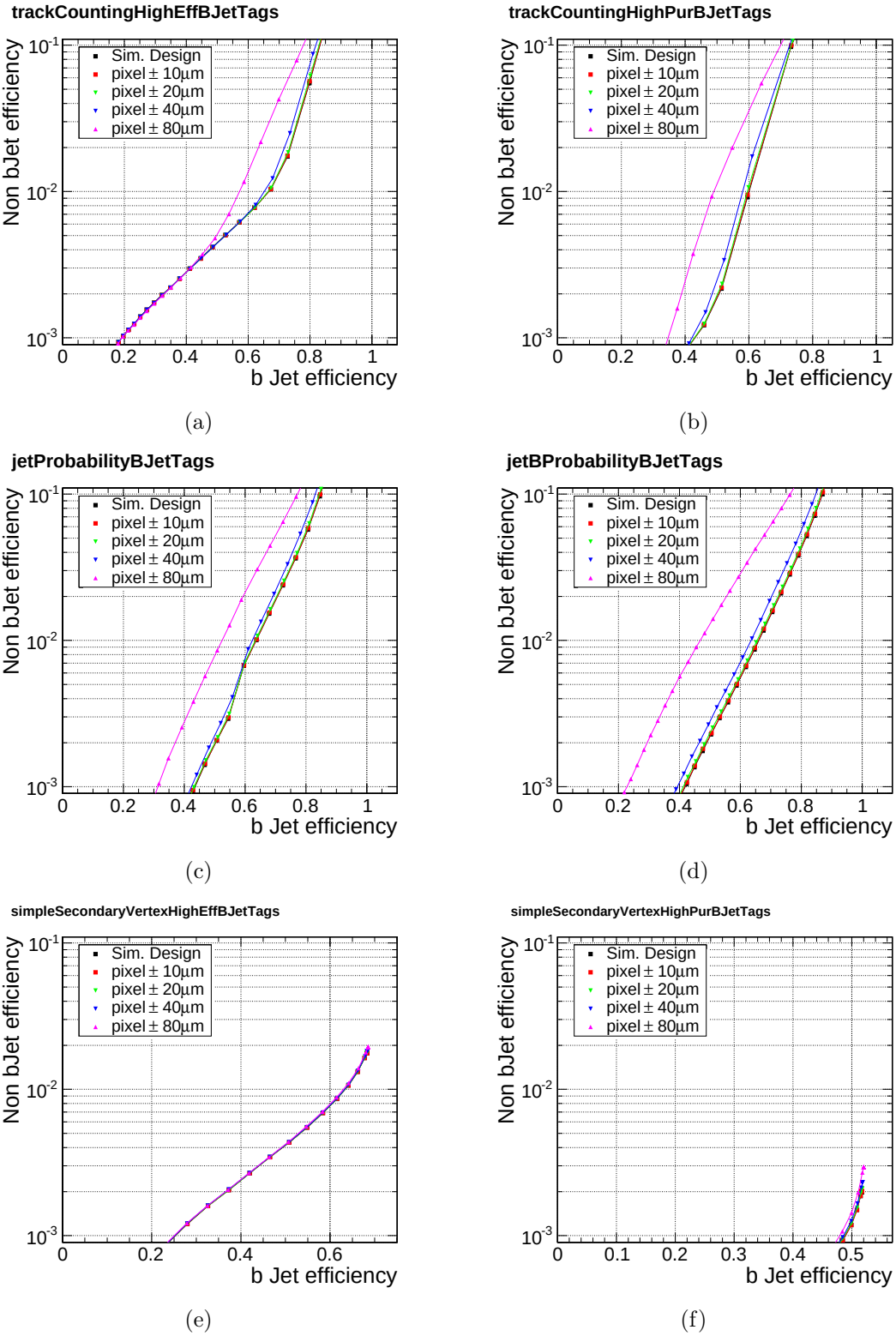

Figure 6.5: Mistag vs b-tagging efficiency for TCHE (a), TCHP (b), jet probability (c), jet b probability (d), SSVHE (e) and SSVHP (f) for geometries with different displacements of the pixel barrel half-shells.

6.2 Weak Mode Studies Using the Z Boson

Weak modes, as discussed in section 4.3.1, will form the dominant challenge in terms of alignment for the upcoming periods of CMS operations. As shown in the previous sections 5.2 and 6.1.2, the achieved local module precision is almost reaching design conditions. Biases that might have been introduced have little effects on the vertex related tracking parameters used in most b-tagging algorithms. Nevertheless, the usage of tracks from cosmic rays and minimum bias events bares the risk of introducing correlated detector deformations that bias the track momentum. Here tracks with high transverse momentum are most sensitive, such that the Z boson decaying into two muons is a good candidate to test for biases in the reconstructed mass caused by correlated detector distortions. Due to the relatively large mass of the Z boson, the resulting muons have sufficiently high momenta and thus are only minimally affected by multiple scattering. In addition, the moderate boost of the Z boson leads to muons leaving the detector in different directions while the decay products of lower mass resonances like the K_0 or J/Ψ usually point into the same direction. Thus a bias on the reconstructed mass would cancel due to the opposite bias on the momentum. The reconstructed mass of the Z boson can then be displayed differentially versus η and ϕ of the muon tracks to check for biases in the reconstructed Z boson mass in different regions of the detector. In the following sections, the reconstruction of the Z boson mass will be briefly introduced following the standard selection described in [64]. The analysis presented here is performed for different geometries in data and simulation and observed biases were assigned to possible weak modes.

6.2.1 Selection Criteria and Reconstruction of the Z Boson Mass

Since the study is performed in order to compare different aligned geometries, all quantities concerning the muon momentum and direction are determined using the tracker information only. Nevertheless the selected muons are required to have a track matched to a muon reconstructed in the muon system. All muon candidates must fulfil the following requirements [65]:

- $p_T > 20\,\mathrm{GeV}$,
- $|\eta| < 2.1$,
- number of valid hits in the tracker > 10,
- transverse impact parameter with respect to the primary vertex $d_{xy} < 0.2\,\mathrm{cm}$,
- and an absolute tracker isolation $I_{trk} < 3\,\mathrm{GeV}$

where the isolation is defined as the sum of all transverse momenta of those tracks in a cone smaller $\Delta R < 0.3$ around the muon and with a momentum larger $p_T > 1.5\,\mathrm{GeV}$:

$$I_{trk} = \sum_{\substack{\Delta R<0.3 \\ p_T>1.5\,\mathrm{GeV}}} p_T \tag{6.1}$$

Due to the continuously increasing luminosity provided by LHC during the data taking period in 2010, the high level trigger requirements have changed for Run2010B starting with the single non-isolated muon trigger requiring the muon momentum to exceed 9 GeV (*HLT Mu9*) for the first set of runs (146428-148058). From run 148822 on the momentum cut has been increased to 15 GeV and the trigger (*HLT Mu15*) was used. The events considered in the following are required to have at least two muons with opposite charge fulfilling the requirements above, and their invariant mass needs to be in a window between 60 GeV $< m_{\mu\mu} <$ 120 GeV.

While the pure decay width of the Z mass is described by the Breit-Wigner distribution, the resulting mass resonance also reflects the detector resolution. Folding a Breit-Wigner distribution with a Gaussian gives a Voigtian distribution which is parametrised within the used analysis toolkit RooFit [66] as:

$$V(x; M_Z, \sigma, \Gamma) = \frac{1}{(x - M_Z)^2 + \frac{1}{4}\Gamma^2} \otimes \exp(-(x - M_Z)^2/2\sigma^2) \tag{6.2}$$

where x is the invariant mass of the two muons, σ the resolution from the Gaussian distribution and M_Z and Γ the mean and decay width of the Breit-Wigner distribution. Figure 6.6 shows the reconstructed and fitted invariant mass of the two isolated muons for two different geometries in data compared to the realistic misalignment scenario in the simulation. The data agrees well with the simulation, still both show a slightly asymmetric peak such that the fitted Voigtian function does not perfectly describe the reconstructed Z masses. This effect arises from the decreasing nature of the parton distribution functions with growing x as described in section 2.3 which is folded with the Z boson cross section.

All three distributions peak slightly below the nominal Z mass of 91.1876±0.0021 GeV [2]. Since the resolution and the width are correlated in the Voigtian fit, the width of all three fits is found to be about 1.5 times larger than the nominal Z boson width of 2.4952±0.0023 GeV [2]. The precise values obtained in the fit can be found in table 6.2. While the peak values and decay widths are very similar for all three curves, the resolution quoted in the last column improves slightly for the geometry aligned with tracks from both cosmic rays and collisions with respect to the one aligned with tracks from cosmic rays only. The values for the resolution obtained in the simulation for the realistic misalignment scenario are, within the quoted statistical uncertainties, in agreement with the data.

Apart from the exact knowledge of the module position influencing the resolution, the mass peak of the Z boson can also be used to spot detector deformations which do not influence the resolution but affect the track parameters, for example, the transverse momentum which would lead to a broadening of the decay width.

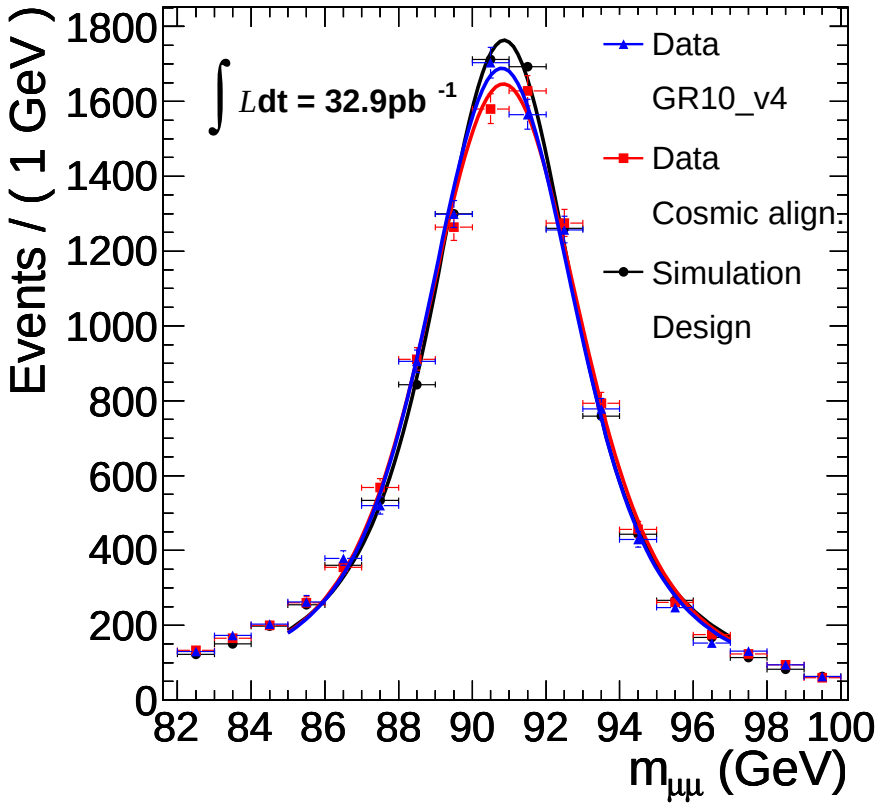

Figure 6.6: Voigtian function fitted to the Z boson mass for alignment gained with tracks from cosmic rays only (red rectangles), run range dependent alignment GR10_v4 (black triangles) and realistic misalignment in simulation (blue dots).

Geometry	$< M_Z >$ [GeV]	Γ [GeV]	σ [GeV]
Data - aligned using tracks from cosmic rays only	90.80 +/- 0.03	3.49 +/- 0.13	1.17 +/- 0.09
Data - aligned using tracks from cosmic rays and collision GR10_v4	90.76 +/- 0.03	3.57 +/- 0.13	1.02 +/- 0.09
Simulation - 2010Realistic misalignment	90.83 +/- 0.03	3.50 +/- 0.12	0.96 +/- 0.09

Table 6.2: Fit parameters of the Voigtian distribution to the Z mass peak.

6.2.2 Influence of Systematic Detector Distortions on Reconstructed Z Mass

With the analysis presented in the following, a twist of the tracker geometry was identified to be a weak mode (see section 4.3) of the alignment procedure presented in section 5.2. Applying the identical alignment procedure to the same set of data, but starting from different initial geometries, leads to different final module positions in global ϕ versus z. Geometry GR10_v3 was obtained by applying the same strategy as for geometry GR10_v4, discussed in section 5.2, with the only difference being that the starting geometry for GR10_v4 was twisted by -330 μrad per meter in z compared to the starting geometry of GR10_v3. The left profile plot in figure 6.7 shows that the resulting geometries GR10_v3 and GR10_v4 still differ in $\Delta\phi$ by about 150 μrad per meter, but the local precision of the modules is identical such that the χ^2-distribution for both geometries is the same as shown in the right plot of figure 6.7. External information is needed to decide which geometry reflects the actual tracker position.

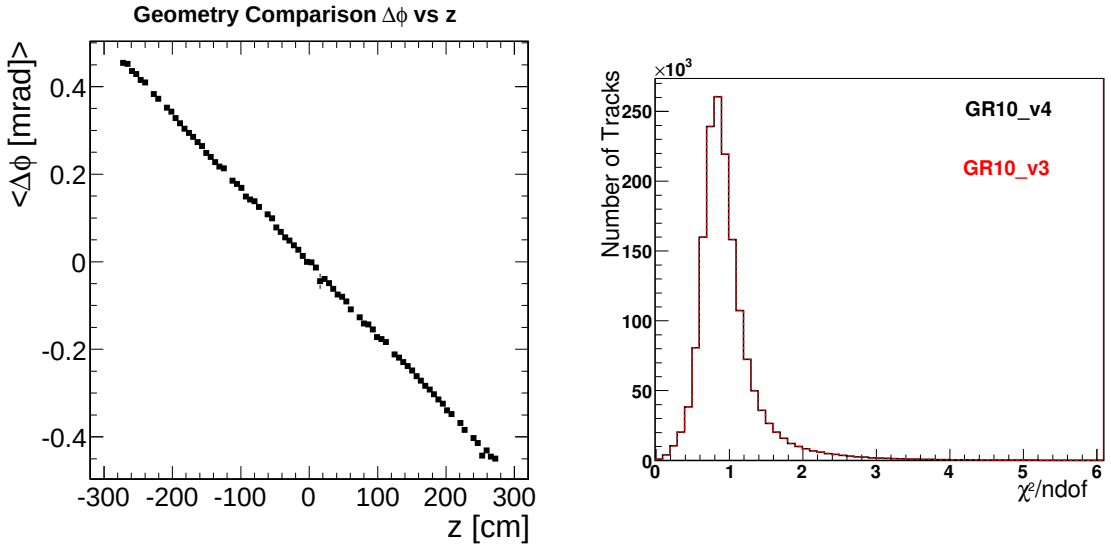

Figure 6.7: Mean difference in ϕ position of the modules as a function of z (left) between GR10_v4 and GR10_v3 do not affect their χ^2-distributions (right).

A twisted tracker geometry biases the track parameters in a correlated way. Depending on the charge of the reconstructed particle, the momentum is either biased towards larger values as illustrated in figure 6.8, or leads to a decreased momentum for a particle with opposite charge but same flight direction. Studies with low mass resonances like the K_0 were found not to be sensitive to the distortion described above as shown in Appendix I. The decay products are strongly boosted and thus mainly point in the same direction. Therefore, biases induced by momentum changing weak modes cancel out, and the reconstructed invariant mass is hardly sensitive to identify the bias. The Z boson, on the other hand, although not produced at rest at the LHC,

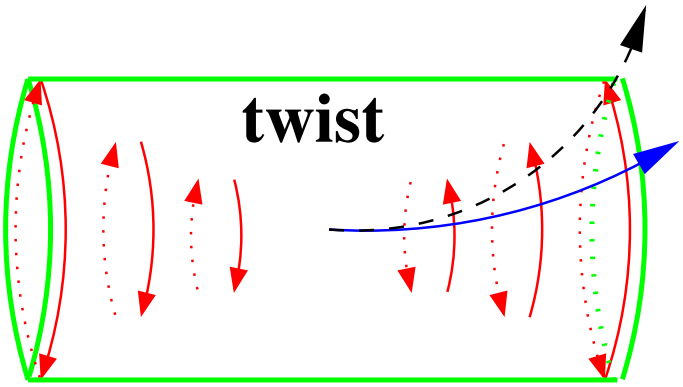

Figure 6.8: Impact of a twist in the tracker geometry on the track parameters [12].

is massive enough such that the decay products traverse through different parts of the detector. Hence, a bias in the reconstructed mass can be observed depending on the direction of flight of the decay products.

Figure 6.9 shows the reconstructed Z boson mass for the two geometries presented above. GR10_v3 shows a 20% degradation of the resolution as quoted in table 6.3 and fewer entries in the peak region.

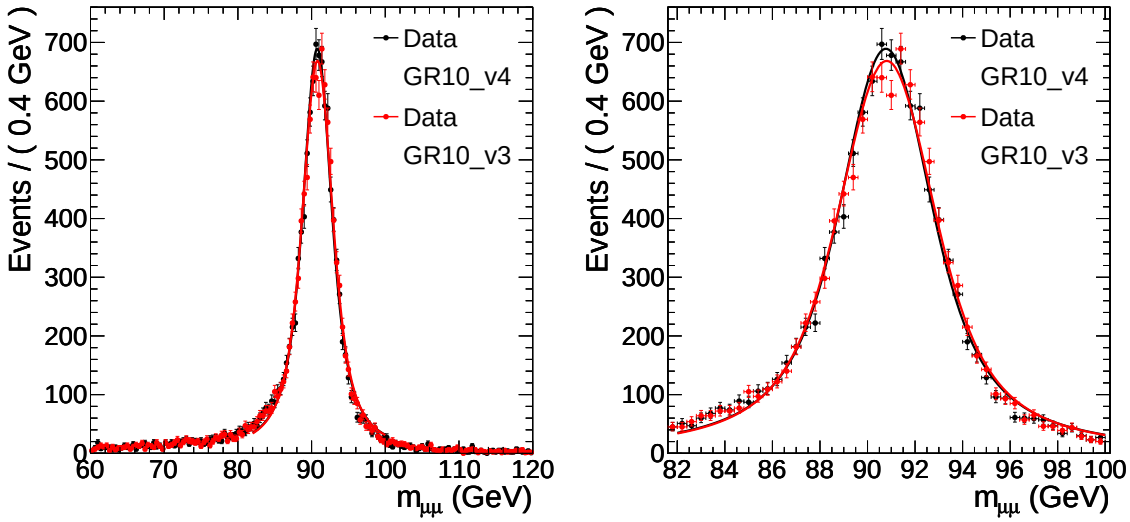

Figure 6.9: Voigtian function fitted to Z boson mass for GR10_v3 and GR10_v4, obtained with the same alignment strategy but started from different initial geometries for a mass window of 60-120 GeV(left) and zoomed in to the peak region (right).

As a function of η of the positively or negatively charged muon, the mean mass value $< M_Z >$ shows an almost linear dependence for geometry GR10_v3 in figure 6.10. The dependence on the charge of the muon is compatible with the behaviour expected for an overall twist of the tracker geometry as presented in figure 6.8. An independent study, using additional information from the calorimeter, which compared the mea-

Geometry	$< M_Z >$[GeV]	Γ[GeV]	σ[GeV]
GR10_v4	90.77 $\pm$ 0.03	3.60 $\pm$ 0.13	0.97 $\pm$ 0.09
GR10_v3	90.81 $\pm$ 0.03	3.47 $\pm$ 0.13	1.15 $\pm$ 0.09

Table 6.3: Fit parameters of the Voigtian distribution to the Z mass peak.

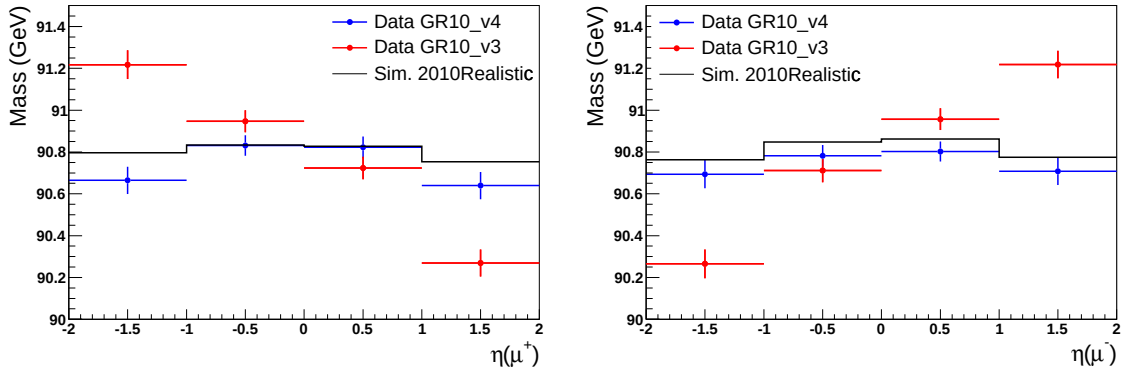

Figure 6.10: Fitted Z mass as a function of η of the positive and negative muon for different geometries.

sured energy of hadrons with the momentum measurement by the tracker, confirmed the twist seen for geometry GR10_v3 and quantified it to 127$\pm$ 13 μrad per meter [12]. The method also identified a bias for geometry GR10_v4 quantified to -16$\pm$ 13 μrad.

In addition to the bias observed in η, all geometries show a dependency of the fitted Z boson mass with respect to ϕ as shown in figure 6.11. As the bias is already visible for geometries aligned using tracks from cosmic rays only, a weak mode might have been introduced by tracks from cosmic rays which hit the modules under different average impact angles for the different regions in ϕ due to their origin outside the tracker volume. The change in phase of the modulation in ϕ for the different geometries is a strong indication for a weak mode. The bias is also present in simulation for the realistic misalignment scenarios which further substantiates the evidence for a weak mode rather than biases related to, for example, the bowed sensors which would not affect the simulation.

Applying an artificial distortion like the sagitta transformation shown in figure 4.4 parametrized by $r\delta\phi = c_1 cos\phi$ (here only the vertical coordinate is shifted) to the design geometry in the simulation changes the design geometry in such a way that it reproduces the modulation of the Z mass bias versus ϕ observed in data apart from the phase as shown in figure 6.12.

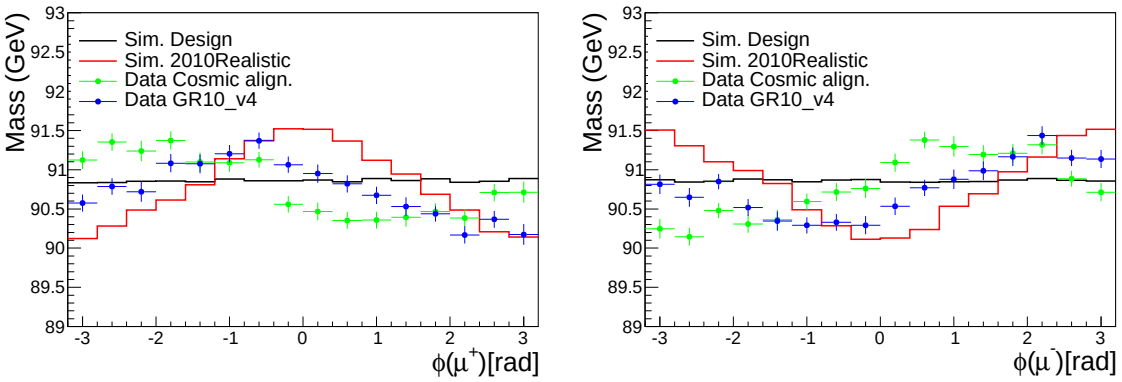

Figure 6.11: Fitted Z mass as a function of ϕ of the positively and negatively charged muon for different geometries in data and simulation.

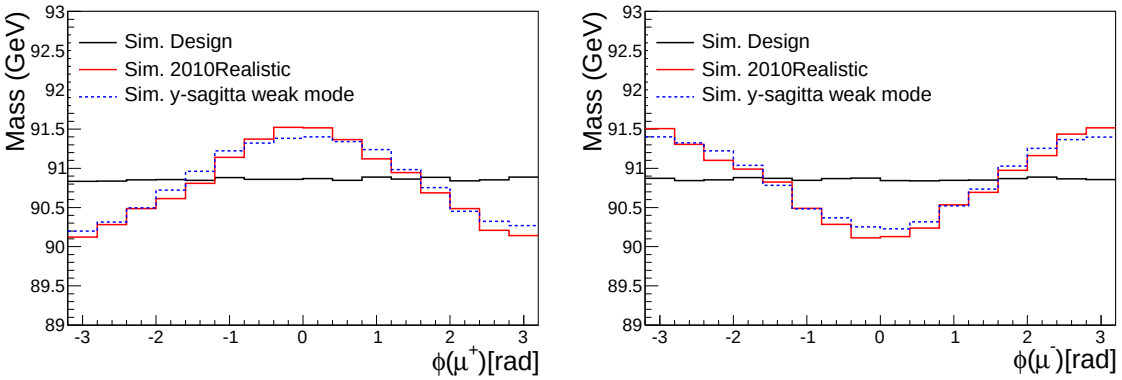

Figure 6.12: Fitted Z mass as a funtion of ϕ of the positively and negatively charged muon for artificially distorted geometry compared to the realistic misalignment scenario in simulation.

6.3 Possible Extensions to the Alignment Strategy

Current analysis relying on the muon momentum can correct the muon momentum scale for the observed biases presented above via a method described in [65]. Nevertheless, it would be preferable to avoid the biases in the first place. This section presents ideas on how to extend the alignment strategy to constrain the observed weak modes.

6.3.1 Constraining the Weak Modes

Since the Z boson mass is sensitive to the deformations of the tracker geometry, shown by the observed biases in η and ϕ, a possible solution to constrain the weak modes could be to use the Z boson mass itself as additional constraint in the global fit.

In [67] a parametrisation of trajectories stemming from a two-body decay is presented, which allows a compact representation of the trajectory as well as a direct estimation of the decay parameters. The momenta $\mathbf{p}^{\pm}$ of the secondary particles produced in a two-body decay are parametrized in the rest frame of the primary particle using the relativistic energy-momentum conservation:

$$\mathbf{p}^{\pm}_{c.m.} = \pm m\sqrt{(\frac{M}{2m})^2 - 1}\begin{pmatrix} \sin\theta\cos\phi \\ \sin\theta\cos\phi \\ \cos\theta \end{pmatrix}, \tag{6.3}$$

where m is the mass of the decay products and M the one of the primary particle. Choosing the convention for the coordinate system of the rest frame in such a way that the z-axis coincide with the momentum of the primary particle $\mathbf{p} = (p_x, p_y, p_z)^T$. X- and Y axis are derived by subsequent rotations around the z-axis by $\tan\gamma = p_y/p_x$ and around the y-axis by $\tan\beta = p_z/p_T$. Following this convention the momenta in the lab frame can be written as:

$$\mathbf{p}^{\pm}(p_x, p_y, p_z, \theta, \phi, M) = \begin{pmatrix} \frac{p_x p_y}{p_T p} & -\frac{p_y}{p_T} & \frac{p_x}{p} \\ \frac{p_y p_y}{p_T p} & \frac{p_x}{p_T} & \frac{p_y}{p} \\ -\frac{p_T}{p} & 0 & \frac{p_z}{p} \end{pmatrix} \begin{pmatrix} \pm m\sqrt{\alpha^2 - 1}\sin\theta\cos\phi \\ \pm m\sqrt{\alpha^2 - 1}\sin\theta\cos\phi \\ \frac{p}{2} \pm \frac{1}{2}\sqrt{\frac{\alpha^2 - 1}{\alpha^2}(p^2 + M^2)}\cos\theta \end{pmatrix} \tag{6.4}$$

Expressed as a function of the decay vertex, 9 parameters are needed to fully describe the decay trajectories:

- the position of the decay vertex $\mathbf{v} = (v_x, v_y, v_z)^T$,
- the momentum $\mathbf{p} = (p_x, p_y, p_z)^T$ of the primary particle in the lab frame,
- the polar angle θ and azimuthal angle ϕ in the rest framework, and
- the mass M of primary particle.

Due to the combined information content of the measurements and the superimposed physical constraints, the presented trajectory description is usable in track-based alignment.

Alternatively, tracks from cosmic rays taken without magnetic field and thus passing straight through the detector could be used to constrain a weak mode like the twist. First tests with data taken without magnetic field in spring 2010 show promising results [68]. Still, the sample is of limited size and compatibility and it is not foreseen to take data from cosmic rays at without magnetic field in 2011, which would be the only way to account for eventual movements of the tracker units during the shutdown and in 2011.

6.3.2 Pixel Half-shells Corrections

Although movements of the pixel half-barrels along the z axis do not show a severe impact on the b-tagging efficiency for the values observed in data so far ($\Delta z < 100 \mu m$), including the alignment of the pixel half-shells in the prompt calibration workflow should be considered since the sensitivity of the b-tagging algorithms might become enhanced with increasing pile up due to ambiguities in the vertexing. Depending on the available number of events, either an alignment with tracks from minimum bias or else isolated muons could be performed to determine the positions of the pixel half-shells either per day or even per run.

Chapter 7

Summary and Conclusions

With the start of operations of the LHC in 2010, a new energy regime has become accessible allowing unprecedented tests of the Standard Model of particle physics as well as first tests of possible extensions. Both precision measurements of standard model quantities as well as possible discoveries of new heavy particles require a careful calibration and thorough understanding of the detection devices. For the CMS detector, one of the challenges was seen in the reduction of the systematic uncertainty on the momentum measurement by the silicon tracker due to the limited knowledge of the silicon-module positions.

Since optical measurements are not sufficient to determine the modules position at the level of accuracy needed and the tracker volume is not accessible during operations, the measured trajectories of charged particles crossing the detector volume are used to determine the module positions. For the study presented in this thesis, the the Millepede II algorithm for track based alignment has been used in the context of the CMS software framework. Exploiting the distinction between 'local' track and 'global' alignment parameters, Millepede II can determine the latter in a single simultaneous fit of millions of tracks and about 50,000 alignment parameters while keeping all correlations between them.

To benefit from the complementary information provided by tracks from cosmic rays and minimum bias events from collisions at a centre-of-mass energy of 7 TeV, about three million tracks from cosmic rays and eight million tracks from collisions have been used to align the CMS tracker. With the alignment strategy presented in this thesis, the achieved local alignment precision meets the design specifications for most regions of the CMS tracker. The combination of tracks from cosmic rays, covering a different phase space than tracks from collisions, and minimum bias events which provide a good illumination of the forward direction of the detector, lead to an alignment precision, reflected in the distribution of the median of the residual distributions per subdetector, within 1μm to the design performance for the most sensitive coordinate.

Observed movements of the pixel half-shells with respect to each other of up to 70μm along the beamline during operations could be corrected for. Therefore the

alignment strategy has been adjusted in such a way that the positions of the pixel half-layer and half-disc are determined for seven identified intervals while the single module positions are calculated with respect to the high level structures utilising all information provided by the combination of tracks from cosmic rays and collisions.

Besides a variety of validation methods concerning the achieved local alignment precision, several studies of physics objects have been performed to test their sensitivity on alignment:

- identification efficiency of jets from b quarks
- reconstructed K_0 mass
- reconstructed Z boson mass

Tests in the simulation concerning the impact of the achieved alignment on b-tagging efficiencies have been performed. Independent of the algorithm under consideration the corresponding efficiency is no longer limited by the precision achieved. Even the influence of displacements of the pixel half-shells on the b-tagging performance have shown a rather moderate impact. However, the increasing amount of pile-up as well as other effects which might not be reflected in the simulation, could lead to larger effects in data. Hence, further studies in data should be performed to substantiate and quantify the arising uncertainties on the b-tagging performance. To provide immediate corrections for movements of higher level structures in the future, especially for the pixel, their alignment could become part of the prompt calibration done within a 48 h window between the data taking and its further reprocessing.

Keeping track of weak modes, i.e. deformations that bias the track parameters rather than influencing the overall χ^2-distribution, is an important task. Within this thesis, studies of the reconstructed Z boson mass have been presented. A twist of the tracker has been observed which is not constrained by the alignment strategy presented (weak mode), leading to a bias of the reconstructed Z mass as a function of η. In addition, a bias of the reconstructed Z mass as a function of ϕ has been identified and tests in the simulation suggest that a sagitta-distortion of the tracker could have caused the observed modulation. Such a distortion might arise from the special impact topology of tracks from cosmic rays which hit the modules on average under different angles depending on their ϕ-position.

Future alignment activities will concentrate on constraints of weak modes. Since the reconstructed Z boson mass has shown to be sensitive, the logical consequence would be to include the information in the alignment via a mass constraint. A possible trajectory parametrisation has already been implemented and since the LHC reached luminosities $> 10^{32} cm^{-2} s^{-1}$ end of 2010, a sufficient amount of data from Z boson decays is granted even in case of need for run range dependent alignments due to movements of detector substructures.
Alternatively, tracks from cosmic rays taken with the magnetic field off showed promising results in constraining a twisted tracker. But since cosmic rays at without mag-

netic field are not recorded on a regular basis, the Z mass constraint seems to be more appropriate.

Studies of uncertainties arising from misalignment using known physics processes or objects will continue to deepen the understanding of its impact in order to provide realistic uncertainty estimates for possible future discoveries or exclusions. Overall, the alignment of the CMS silicon tracker has reached a remarkable precision which locally meets the design specifications such that the tracking precision is not limited due to misalignment. The alignment results have provided vital information and feedback for the calibration of the tracker itself and in terms of intercalibration with other detector subsystems.

Appendix A

Group theory and gauge transformations

Group U(1) is the simplest case of the general unitary group U(n), consisting of $n \times n$ matrices with matrix multiplication as group operation. It is a subgroup of the general Lie group GL(n). U(1) is called rotation group and can be represented by all complex numbers with norm 1. Every rotation can be expressed as the product of many successive infinitesimal rotations. A rotation leaves the probability unchanged to find a system described by $|\psi\rangle$ in state $|\phi\rangle$

$$|\psi\rangle \rightarrow |\psi'\rangle = U\,|\psi\rangle \tag{A.1}$$

$$|\langle\phi|\psi\rangle|^2 = |\langle\psi'|\phi'\rangle|^2 = \left|\langle\phi\left|U^\dagger U\right|\psi\rangle\right|^2. \tag{A.2}$$

Therefore, U must be a unitary operator. Furthermore, the Hamiltonian is unchanged by the rotation operation

$$\langle\psi'|H|\psi'\rangle = \langle\psi|U^\dagger HU|\psi\rangle = \langle\psi|H|\psi\rangle\,. \tag{A.3}$$

This means that H commutes with the rotation operator

$$[U, H] = UH - HU = 0. \tag{A.4}$$

Group SU(2) is a subgroup of U(n) called special unitary group of unitary matrices with unit determinant. Its generators are proportional to the Pauli matrices and can be written as

$$J_i = \frac{1}{2}\tau_i \quad \text{with i} = 1, 2, 3 \tag{A.5}$$

where τ_i are the Pauli matrices[1]. The basis is conventionally chosen to be the column vectors $\begin{pmatrix} 1 \\ 0 \end{pmatrix}$ and $\begin{pmatrix} 0 \\ 1 \end{pmatrix}$ that are used to describe a particle with spin up $(+\frac{1}{2})$ and

[1] $\tau_1 = \begin{pmatrix} 0 & 1 \\ 1 & 0 \end{pmatrix}, \tau_2 = \begin{pmatrix} 0 & -i \\ i & 0 \end{pmatrix}, \tau_3 = \begin{pmatrix} 1 & 0 \\ 0 & -1 \end{pmatrix}$

spin down ($-\frac{1}{2}$).

Group SU(3) is formed by the set of unitary 3×3 matrices with $det\, U = 1$. The generators are eight linearly independent traceless hermitian 3×3 matrices, usually denoted λ_i with $i = 1, ..., 8$. Only two of them can be diagonal, for example

$$\lambda_3 = \begin{pmatrix} 1 & & \\ & -1 & \\ & & 0 \end{pmatrix}, \qquad \lambda_8 = \sqrt{\frac{1}{3}} \begin{pmatrix} 1 & & \\ & 1 & \\ & & -2 \end{pmatrix}. \tag{A.6}$$

For this choice the three colour charges of a quark (see 2.2.4) form a fundamental representation

$$R = \begin{pmatrix} 1 \\ 0 \\ 0 \end{pmatrix}, \quad G = \begin{pmatrix} 0 \\ 1 \\ 0 \end{pmatrix}, \quad B = \begin{pmatrix} 0 \\ 0 \\ 1 \end{pmatrix}.$$

Gauge symmetry can be best discussed in the framework of Lagrangian field theory. The Lagrangian from classical mechanics[2] is transformed into a Lagrangian density where the field ϕ itself is a function of the parameter x_μ

$$L\left(q_i, \dot{q}_i, t\right) \rightarrow \mathcal{L}\left(\phi, \frac{\partial \phi}{\partial x_\mu}, x_\mu\right). \tag{A.7}$$

and $L = \int \mathcal{L} d^3x$. The Euler-Lagrange equation for $\mathcal{L}$ becomes

$$\frac{\partial}{\partial x_\mu}\left(\frac{\partial \mathcal{L}}{\partial\left(\partial\phi/\partial x_\mu\right)}\right) - \frac{\partial \mathcal{L}}{\partial \phi} = 0\,. \tag{A.8}$$

The Dirac equation for free particles follows the Lagrangian formalism for

$$\mathcal{L} = i\bar{\psi}\gamma_\mu \partial^\mu \psi - m\bar{\psi}\psi\,. \tag{A.9}$$

The Lagrangian of a complex field, used to describe an electron for example, is invariant under a global phase transformation

$$\psi(x) \rightarrow e^{i\alpha}\psi(x)\,. \tag{A.10}$$

For an infinitesimal transformation this can be written as

$$\psi(x) \rightarrow (1 + i\alpha)\,\psi(x) \tag{A.11}$$

and from the invariance of the Lagrangian follows

$$0 = \partial\mathcal{L} = \frac{\partial \mathcal{L}}{\partial \psi}\delta\psi + \frac{\partial \mathcal{L}}{\partial\left(\partial_\mu \psi\right)}\delta\left(\partial_\mu \psi\right) + \delta\bar{\psi}\frac{\partial \mathcal{L}}{\partial \bar{\psi}} + \delta\left(\partial_\mu \bar{\psi}\right)\frac{\partial \mathcal{L}}{\partial\left(\partial_\mu \bar{\psi}\right)} \tag{A.12}$$

$$= \frac{\partial \mathcal{L}}{\partial \psi}\left(i\alpha\psi\right) + \frac{\partial \mathcal{L}}{\partial\left(\partial_\mu \psi\right)}\left(i\alpha\partial_\mu \psi\right) + \cdots \tag{A.13}$$

$$= i\alpha\left[\frac{\partial \mathcal{L}}{\partial \psi} - \partial_\mu\left(\frac{\partial \mathcal{L}}{\partial\left(\partial_\mu \psi\right)}\right)\right]\psi + i\alpha\partial_\mu\left(\frac{\partial \mathcal{L}}{\partial\left(\partial_\mu \psi\right)}\psi\right) + \cdots. \tag{A.14}$$

[2] $L = T - V$ where T denotes the kinematic energy term and V the potential energy term.

The first term in brackets and its analogon for $\bar{\psi}$ vanish as a result of (A.8). The remaining equation can only be solved for a conserved current

$$\partial_\mu j^\mu = 0 \tag{A.15}$$

where

$$j^\mu = \frac{ie}{2}\left(\frac{\partial\mathcal{L}}{\partial\left(\partial_\mu\psi\right)}\psi - \bar{\psi}\frac{\partial\mathcal{L}}{\partial\left(\partial_\mu\bar{\psi}\right)}\right) . \tag{A.16}$$

This global gauge transformation can be generalized to a local gauge transformation if α is allowed to differ from space-time point to point

$$\psi(x) \to e^{i\alpha(x)}\psi(x) . \tag{A.17}$$

Now the Lagrangian from (A.9) is no longer invariant under the phase transformation. The term $\partial_\mu\alpha$ of the derivative

$$\partial_\mu\psi \to e^{i\alpha(x)}\partial_\mu\psi + ie^{i\alpha(x)}\psi\partial_\mu\alpha \tag{A.18}$$

breaks the invariance of $\mathcal{L}$. To re-establish the invariance the derivative must be modified to transform covariantly under phase transformations

$$D_\mu \equiv \partial_\mu - ieA_\mu \tag{A.19}$$

where A is a vector field that transforms as

$$A_\mu \to A_\mu + \frac{1}{e}\partial_\mu\alpha . \tag{A.20}$$

It can be shown that by introducing this gauge field the Lagrangian of a free massless particle fulfils local gauge invariance.

Appendix B

Derivation of linear equation system

The χ^2-function to be minimized in the linear least squares fit

$$\chi^2 = \sum_j \sum_i r_{ij}^2(\tau, \mathbf{p}) \simeq \sum_j \sum_i \frac{1}{\sigma_i^2} \left(m_i - \left(y_i(\tau_{\mathbf{j0}}, \mathbf{p_0}) + \frac{\partial y_i}{\partial \mathbf{p}} \Delta \mathbf{p} + \frac{\partial y_i}{\partial \tau_j} \Delta \tau_j \right) \right)^2 \tag{B.1}$$

can be written in matrix equation:

$$\begin{aligned} \chi^2(\mathbf{x}) &= (\mathbf{y} - \mathbf{D} \cdot \mathbf{x})^T \mathbf{V}^{-1} (\mathbf{y} - \mathbf{D} \cdot \mathbf{x}) \\ &= (\mathbf{D} \cdot \mathbf{x})^T \mathbf{V}^{-1} (\mathbf{D} \cdot \mathbf{x}) + \mathbf{y}^T \cdot \mathbf{V}^{-1} \cdot \mathbf{y} - \mathbf{y}^T \cdot \mathbf{V}^{-1} (\mathbf{D} \cdot \mathbf{x}) - (\mathbf{D} \cdot \mathbf{x})^T \mathbf{V}^{-1} \cdot \mathbf{y} \\ &= \mathbf{x}^T \cdot (\mathbf{D}^T \mathbf{V}^{-1} \mathbf{D}) \cdot \mathbf{x} + \mathbf{y}^T \cdot \mathbf{V}^{-1} \cdot \mathbf{y} - \mathbf{y}^T \cdot (\mathbf{V}^{-1} \mathbf{D}) \cdot \mathbf{x} - \mathbf{x}^T \cdot (\mathbf{D}^T \mathbf{V}^{-1}) \cdot \mathbf{y} \end{aligned} \tag{B.2}$$

where $\mathbf{x}$ is the vector of n parameters and $\mathbf{Dx}$ is the linearised expression of the prediction $\mathbf{h}_{pred} = F(\mathbf{x})$. Setting the derivative of the objective function to zero, delivers the final matrix equation to be solved:

$$\begin{aligned} 0 &\simeq \frac{\partial F}{\partial \mathbf{x}} \\ &= \mathbf{x}^T \cdot \mathbf{D}^T \mathbf{V}^{-1} \mathbf{D} + (\mathbf{D}^T \mathbf{V}^{-1} \mathbf{D} \cdot \mathbf{x})^T - \mathbf{y}^T \cdot \mathbf{V}^{-1} \mathbf{D} - (\mathbf{D}^T \mathbf{V}^{-1} \cdot \mathbf{y})^T \\ &= 2(\mathbf{D}^T \mathbf{V}^{-1} \mathbf{D} \cdot \mathbf{x} - \mathbf{D}^T \mathbf{V}^{-1} \cdot \mathbf{y})^T \end{aligned} \tag{B.3}$$

using $\frac{\partial \mathbf{a}^T \mathbf{x}}{\partial \mathbf{x}} + \frac{\partial \mathbf{x}^T \mathbf{a}}{\partial \mathbf{x}} = \mathbf{a}^T$ and $(\mathbf{ABC})^T = \mathbf{C}^T \mathbf{B}^T \mathbf{A}^T$. From equation B.3 follows that the minimum is found if

$$\mathbf{D}^T \mathbf{V}^{-1} \mathbf{D} \cdot \mathbf{x} = \mathbf{D}^T \mathbf{V}^{-1} \cdot \mathbf{y}. \tag{B.4}$$

Thus the equation to be solved is

$$\mathbf{C} \cdot \mathbf{x} = b \tag{B.5}$$

with $\mathbf{C} = \mathbf{D}^T \mathbf{V}^{-1} \mathbf{D}$ and $\mathbf{b} = \mathbf{D}^T \mathbf{V}^{-1} \cdot \mathbf{y}$.

Appendix C

Matrix reduction

A matrix equation $Ca = b$ with a symmetric matrix can be partitioned (C_{11} and C_{22} are symmetric matrices):

$$\left(\begin{array}{c|c} C_{11} & C_{12} \\ \hline C_{21} & C_{22} \end{array}\right) \times \left(\begin{array}{c} a_1 \\ \hline a_2 \end{array}\right) = \left(\begin{array}{c} b_1 \\ \hline b_2 \end{array}\right) \tag{C.1}$$

In the case of a zero rectangular matrix C_{12} the result for the vector a_2 would be $C_{22}a_2 = b_2$, which is solved by $a_2^* = C_{22}^{-1}b_2$; this is called a local solution and corresponds to an improved least squares track fit. In the non-zero case for C_{12} the complete solution for the two vectors a_1 and a_2 can be written in the form

$$\left(\begin{array}{c} a_1 \\ \hline a_2 \end{array}\right) = \left(\begin{array}{c|c} B & -BC_{12}C_{22}^{-1} \\ \hline C_{22}^{-1}C_{12}^T B & C_{22}^{-1} - C_{22}^{-1}C_{12}^T BC_{12}C_{22}^{-1} \end{array}\right) \left(\begin{array}{c} b_1 \\ \hline b_2 \end{array}\right) \tag{C.2}$$

where the submatrix B is the inverse of the expression $(C_{11} - C_{12}C_{21}^{-1}C_{12}^T)$, called Schurs complement. The solution for vector a_1 can be obtained from the solution of the reduced matrix equation

$$(C_{11} - C_{12}C_{21}^{-1}C_{12}^T)a_1 = (b_1 - C_{12}a_2^*). \tag{C.3}$$

Appendix D

Derivatives for the Broken Lines Trajectory

The propagation from one scatterer/measurement plane to another is done using the curvilinear Jacobian as presented in [69]:

$$\frac{\partial curv}{\partial curv_0} = \frac{\partial(\frac{q}{p}, \lambda, \theta, x_\perp, y_\perp)}{\partial(\frac{q}{p_0}, \lambda_0, \theta_0, x_{\perp 0}, y_{\perp 0})} \tag{D.1}$$

For an initial offset $\Delta\mathbf{u}_0$, slope $\Delta\alpha_0$ and curvature $\kappa_0 = \Delta q/p_0$ the offset can be propagated as follows:

$$\Delta\mathbf{u} = \frac{\partial\mathbf{u}}{\partial\mathbf{u}_0}\Delta\mathbf{u}_0 + \frac{\partial\mathbf{u}}{\partial\vec{\alpha}_0}\Delta\vec{\alpha}_0 + \frac{\partial\mathbf{u}}{\partial\kappa_0}\Delta\kappa_0 = \mathbf{J}\Delta\mathbf{u}_0 + \mathbf{S}\Delta\vec{\alpha}_0 + d\Delta\kappa_0 \tag{D.2}$$

with

$$\frac{\partial\mathbf{u}}{\partial\mathbf{a}_0} = \frac{\partial\mathbf{u}}{\partial curv}\frac{\partial curv}{\partial curv_0}\frac{\partial curv_0}{\partial\mathbf{a}_0} \tag{D.3}$$

following the chain rule for all track parameters a_0 with

$$\frac{\partial\mathbf{u}}{\partial curv} = \begin{pmatrix} 0 & 0 & 0 & 1 & 0 \\ 0 & 0 & 0 & 0 & 1 \end{pmatrix} \tag{D.4}$$

and

$$\frac{\partial curv_0}{\partial\mathbf{u}_0}\begin{pmatrix} 0 & 0 \\ 0 & 0 \\ 0 & 0 \\ 1 & 0 \\ 0 & 1 \end{pmatrix}, \quad \frac{\partial curv_0}{\partial\vec{\alpha}_0}\begin{pmatrix} 0 & 0 \\ 0 & 1 \\ \frac{1}{cos\lambda_0} & 0 \\ 0 & 0 \\ 0 & 0 \end{pmatrix}, \quad \frac{\partial curv_0}{\partial\kappa_0}\begin{pmatrix} 1 \\ 0 \\ 0 \\ 0 \\ 0 \end{pmatrix} \tag{D.5}$$

Solving the equation for $\Delta\alpha$ gives:

$$\Delta\vec{\alpha}_0 = \mathbf{S}^{-1}\left(\Delta\mathbf{u} - \mathbf{J}\Delta\mathbf{u_0} - \mathbf{d}\Delta\kappa\right) \tag{D.6}$$

To calculate the kink angle a triplet of offsets is needed, u_-, u_0 and u_+, where u_- and u_+ can be formulated depending on u_0:

$$\begin{array}{rcll} \mathbf{u}_+ & = & \mathbf{J}_+\Delta\mathbf{u_0} + \mathbf{S}_+\Delta\vec{\alpha}_+ + \mathbf{d}_+\Delta\kappa & \mathbf{u}_- = \mathbf{J}_-\Delta\mathbf{u_0} + \mathbf{S}_-\Delta\vec{\alpha}_- + \mathbf{d}_-\Delta\kappa \\ \Delta\vec{\alpha}_+ & = & \mathbf{W}_+ = (\mathbf{u}_+ - \mathbf{J}_+\Delta\mathbf{u_0} - \mathbf{d}_+\Delta\kappa) & \Delta\vec{\alpha}_- = \mathbf{W}_- = (\mathbf{u}_- - \mathbf{J}_+\Delta\mathbf{u_0} + \mathbf{d}_-\Delta\kappa) \\ \mathbf{W}_+ & = & \mathbf{S}_+^{-1} & \mathbf{W}_- = \mathbf{S}_-^{-1} \end{array} \tag{D.7}$$

The difference between $\Delta\vec{\alpha}_+$ and $\Delta\vec{\alpha}_-$ gives then the kink angle β.

$$\vec{\beta} = \Delta\vec{\alpha}_+ - \Delta\vec{\alpha}_- \tag{D.8}$$

$$= \mathbf{W}_+\mathbf{u}_+ - (\mathbf{W}_+\mathbf{J}_+ + \mathbf{W}_-\mathbf{J}_-)\mathbf{u}_0 + \mathbf{W}_-\mathbf{u}_-(\mathbf{W}_+\mathbf{d}_+\mathbf{W}_-\mathbf{d}_-)\Delta\kappa \tag{D.9}$$

The get the interpolated offset u_{int} between two adjacent scatterers D.8 has to be solved for $u_0 = u_{int}$ and $\beta = 0$:

$$\begin{array}{rcl} \mathbf{u}_{int} & = & (\mathbf{W}_+\mathbf{J}_+ + \mathbf{W}_-\mathbf{J}_-)^{-1}(\mathbf{W}_+\mathbf{u}_+ - \mathbf{W}_-\mathbf{u}_-) \\ & & -(\mathbf{W}_+\mathbf{J}_+ + \mathbf{W}_-\mathbf{J}_-)^{-1}(\mathbf{W}_+\mathbf{d}_+ = \mathbf{W}_-\mathbf{d}_-) \cdot \Delta\kappa \end{array} \tag{D.10}$$

Appendix E

Impact of Lorentz angle calibration

In case of a non-optimal Lorentz angle calibration the corrections of the module positions will result in a different overall shift of the mean value of the track residuals for modules with different relative orientation between the solenoid and the drift field. In the 4 outermost TOB layers, the single sided modules are grouped in rods where the modules at inner radii are facing away from the beamline and thus the drift direction of the electrons is opposite to the modules at larger radii where the modules are facing towards the beam pipe. Figure E.1 shows the residual distributions for the 6 layers of the TOB validated with tracks from cosmic rays taken without magnetic field, once for an alignment also using tracks recorded when the magnetic field was off, referred to as CRUZET (Cosmic Run at Zero Tesla) and once for an alignment performed with tracks taken with the magnetic field at nominal strength of 3.8 T, referred to as CRAFT (Cosmic Run At Four Tesla). The latter is correcting for the non optimal Lorentz angle calibration and thus shifting the modules according to their orientation with respect to the beampipe in opposite direction which results in the double peak structures visible for layers three to six. Figure E.2 shows the same distributions including an alignment with correct Lorentz angle calibration, referred to as 'HIP[1] new LA'. The double peak is no longer visible.

[1]The 'Hit and Impact Position' is briefly described in section 4.1.

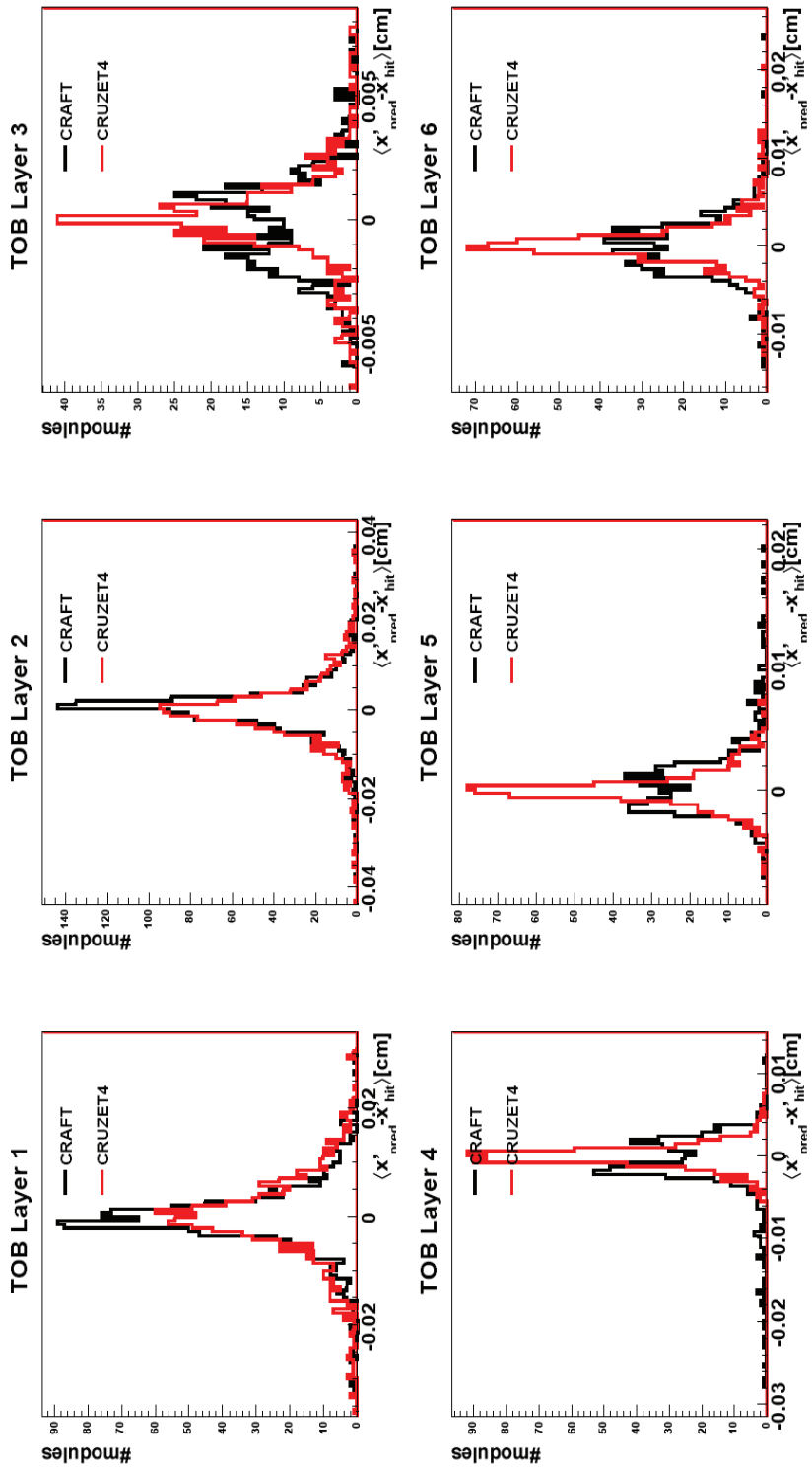

Figure E.1: Mean value of the residuals in x per layer in TOB for aligned geometry gained with incorrect Lorentz angle calibration validated with 3.8 T (CRAFT) and 0 T data (CRUZET).

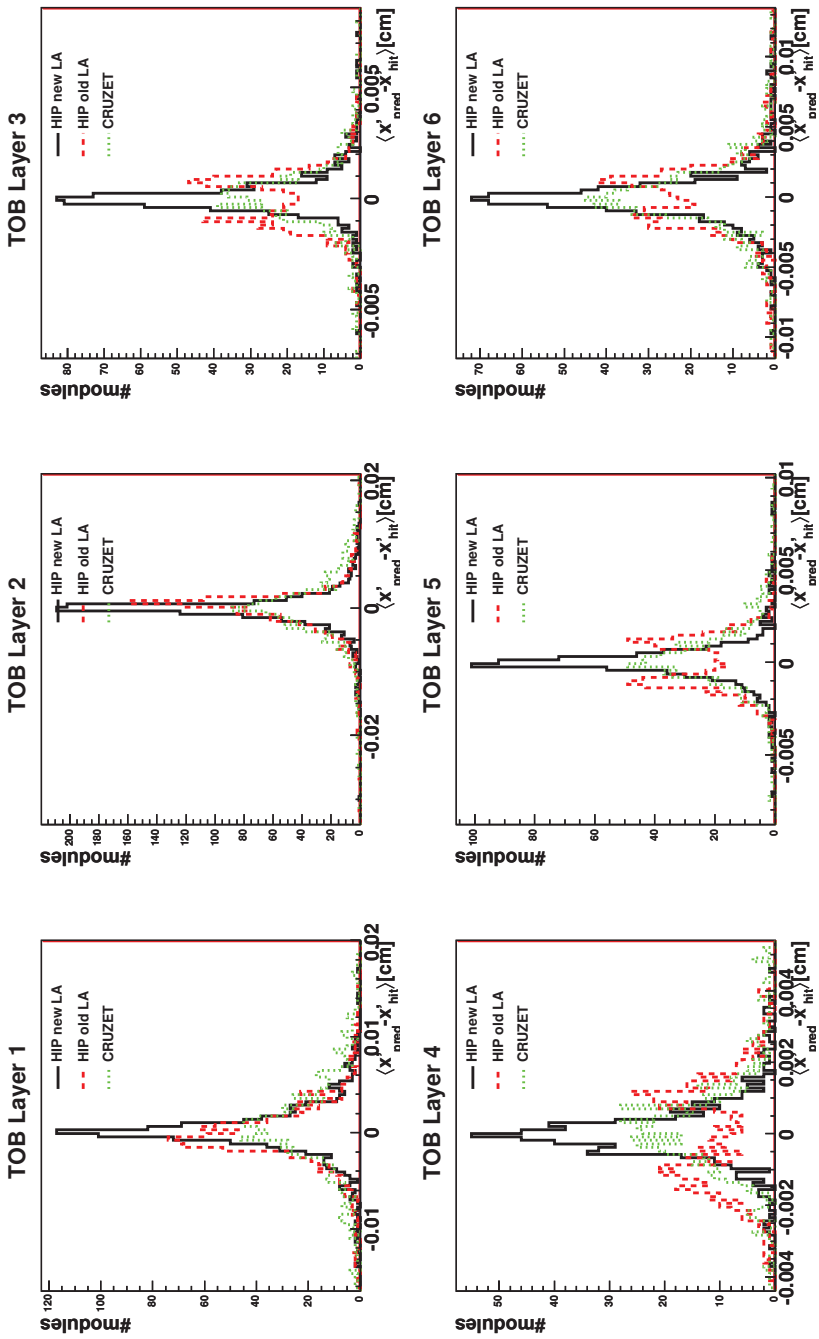

Figure E.2: Comparison of the mean value of the residuals in x per layer in TOB for aligned geometry with incorrect Lorentz angle calibration (HIP old LA), corrected Lorentz angle calibration (HIP new LA) and geometry obtained on tracks from cosmic rays taken at 0 T validated on tracks from cosmic rays taken 0 T .

Appendix F

Influence of tracker read out mode on alignment

While the tracker can be operated in peak mode during data taking of cosmic rays, it is necessary to shorten the read-out time during collisions to account for 25 ns between two bunch crossings. During collisions the tracker is read-out in deconvolution mode [34]. In 2009 cosmic rays have been recorded for both read-out modes. Alignment constants following the same strategy but using either tracks taken in peak or deconvolution mode showed different results in the local w-coordinate since the alignment performed with tracks taken in deconvolution mode corrected for a difference in the reconstructed w position of the modules. While the effect on the thin modules used in TIB was accounting to only a few micron, the thick modules used in the outermost four layers of the TOB showed a significant difference in Δw of about $20\,\mu$m as shown in figure F.1. In addition, a small shift related to the Lorentz angle (see appendix E) could be observed. Both effects can be explained by the so-called Venturi model [70], which describes differences of the charge collection for the two read out modes. Figure F.2 shows the ideal case of a charged particle traversing the silicon sensor. All charges drift to the strip plane of the sensor where they form a cluster that is read out. The cluster barycentre is extrapolated to the mid-plane of the sensor as the true reconstructed hit position. In the deconvolution mode where the readout time is shorter not all charge is collected as the drift time from the backplane of the module is too large. Hence, the reconstructed hit position extrapolated from the cluster barycentre is incorrect and the alignment is compensating this by shifting the module in w direction such that the reconstructed hit lies along the track path again(see figure F.3).

This simplified model neglects the interplay with the Lorentz angle that is causing a small shift in local u in addition. Due to the shorter integration time the charge collection in deconvolution mode also leads to a slightly smaller value of the apparent Lorentz angle. While for large integration times all charge is collected on one single primary strip, the charge is distributed among a primary and auxiliary strips for short charge integration time. Therefore, the apparent Lorentz angle is smaller than the

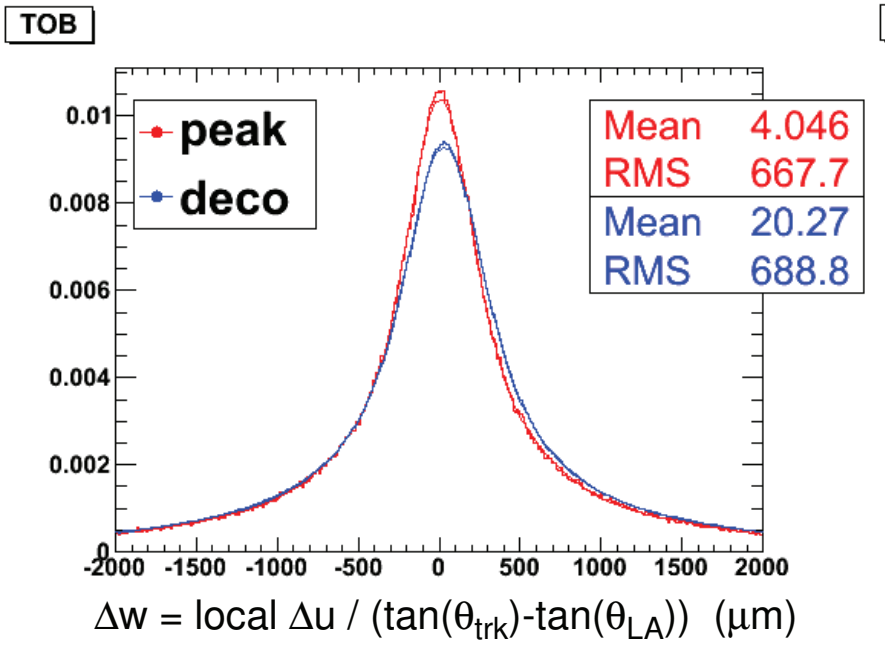

Figure F.1: Difference in Δ w for modules in TOB for peak and deconvolution mode [70].

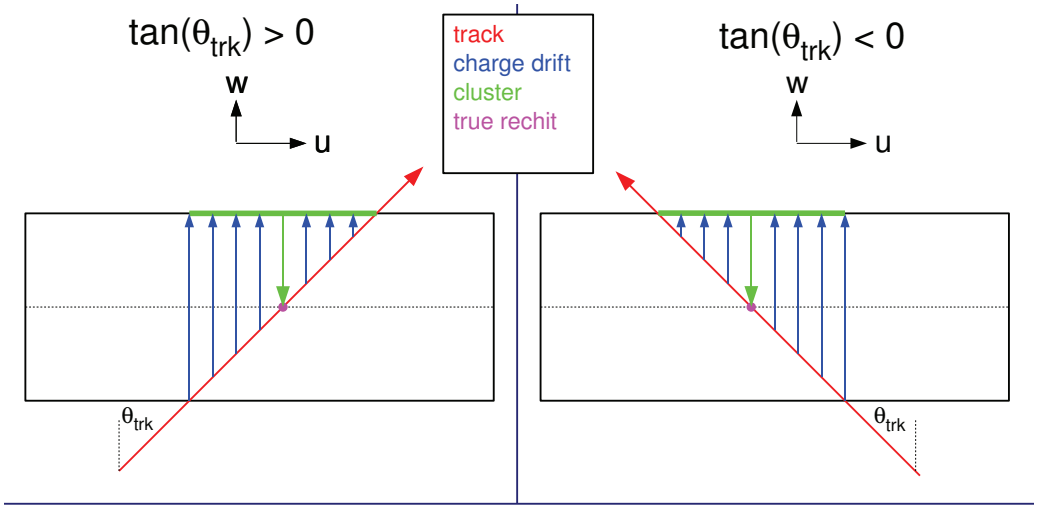

Figure F.2: Ideal case where all charges drift to the sensor plane where they are read out [70].

actual one as illustrated in figure F.4.

Figure F.5 shows the correction of the local u coordinate resulting from the charge loss. The term arising from the non collected charge of the backplane

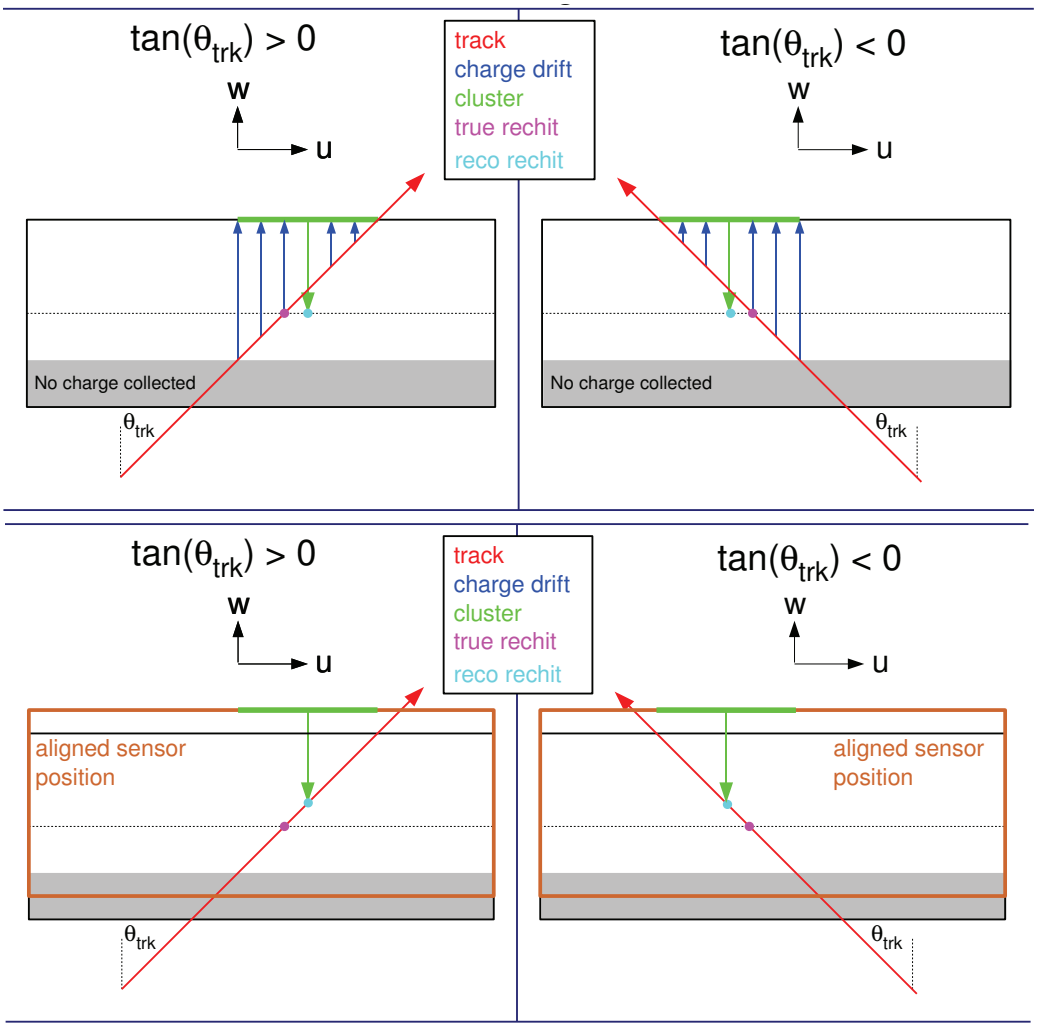

Figure F.3: In deconvolution mode not all charge is collected and the effective charge results in a bias of the reconstructed hit position extrapolated from the clusters barycentre [70].

$\Delta w(\tan\theta_{trk} - \tan\theta_{LA})$ is extended by the correction of a smaller effective Lorentz angle 'seen' at the drift length $H - \Delta w$. Both corrections need to be performed during the local reconstruction to provide unbiased clusters and thus unbiased reconstructed hit positions for the alignment. The correction values found for collision data taken in 2010 for TOB and TIB according to the model outlined are 0.05 μm and 0.034 μm for the backplane corrections Δw in TOB and TIB, respectively. A Lorentz angle correction is only necessary for the TOB as the shift is not significant in the thinner TIB modules. It is measured to be 0.013 rad [70].

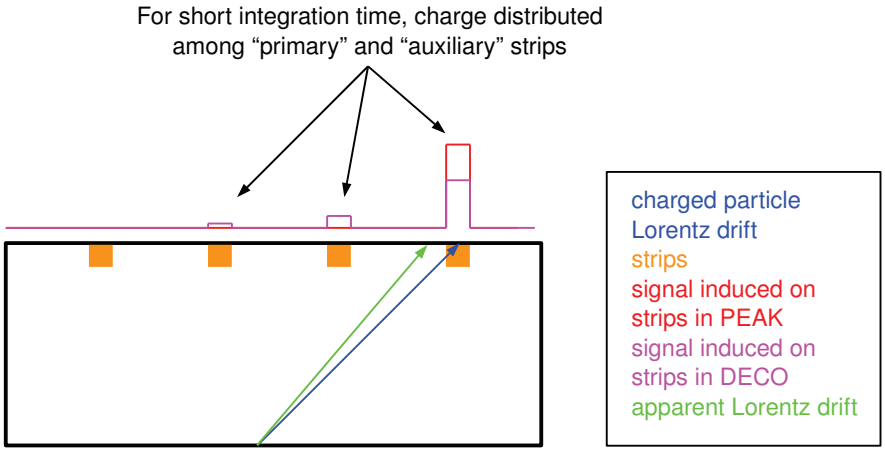

Figure F.4: Distributed charge collection in deconvolution mode leads to smaller effective Lorentz angle [70].

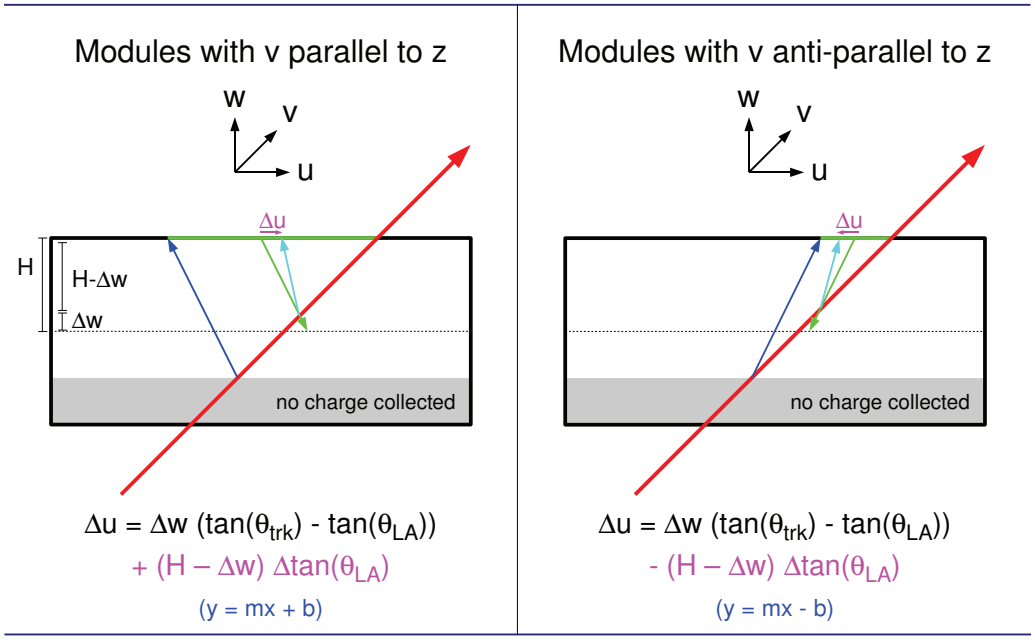

Figure F.5: Charge loss in deconvolution mode leads to an effective Lorentz angle that is smaller than the actual one [70].

Appendix G

Tracker Hit Maps

Figure G.1 shows the tracker maps for 1 Mio. events from cosmic rays taken during CRAFT10 before and after the alignment track selection. Figure G.2 shows the same tracker maps for minimum bias events taken during the first run period. Due to the higher track multiplicity only 200,000 events have been used.

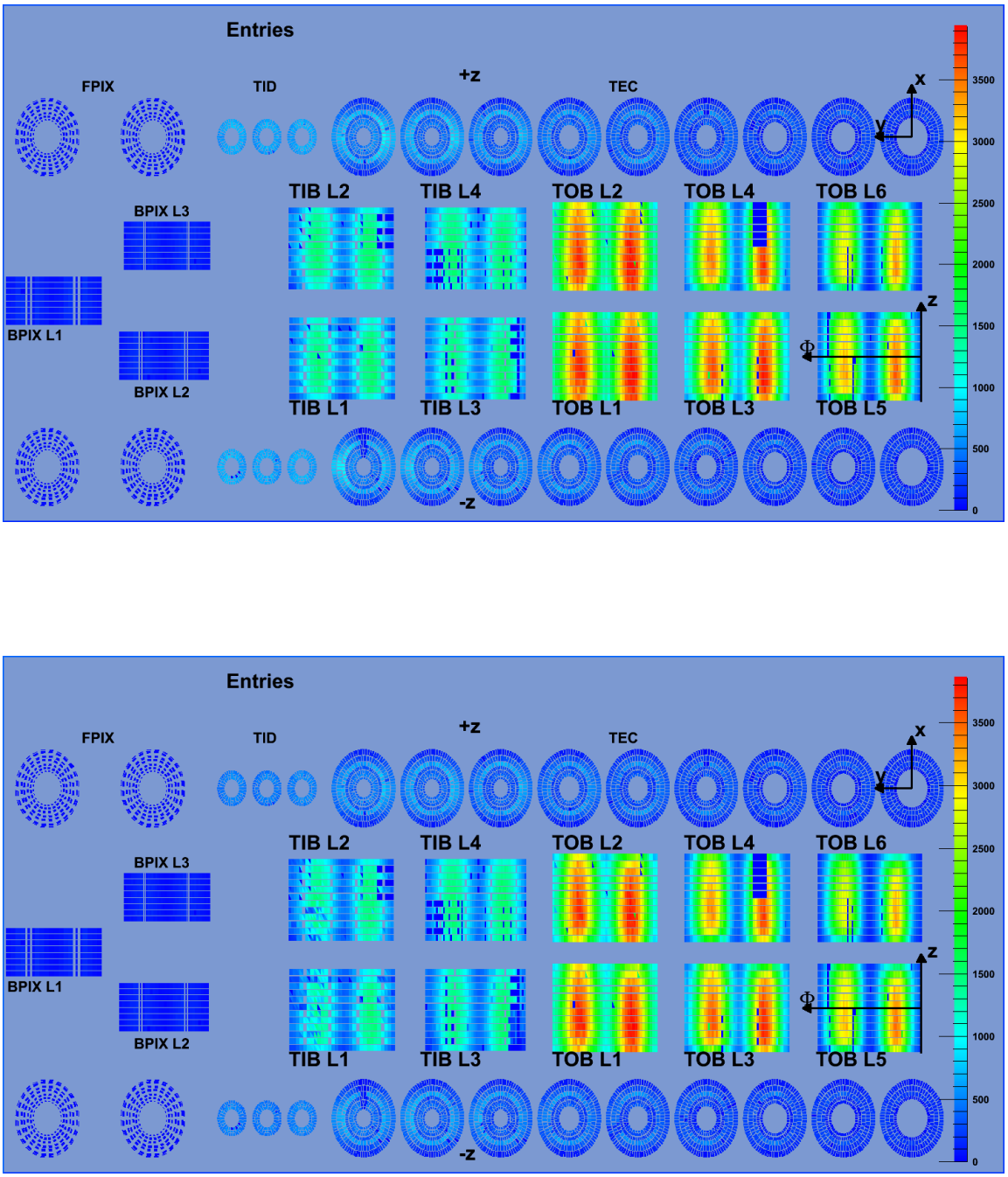

Figure G.1: Tracker map for tracks from cosmic rays before (top) and after (bottom) the alignment track selection.

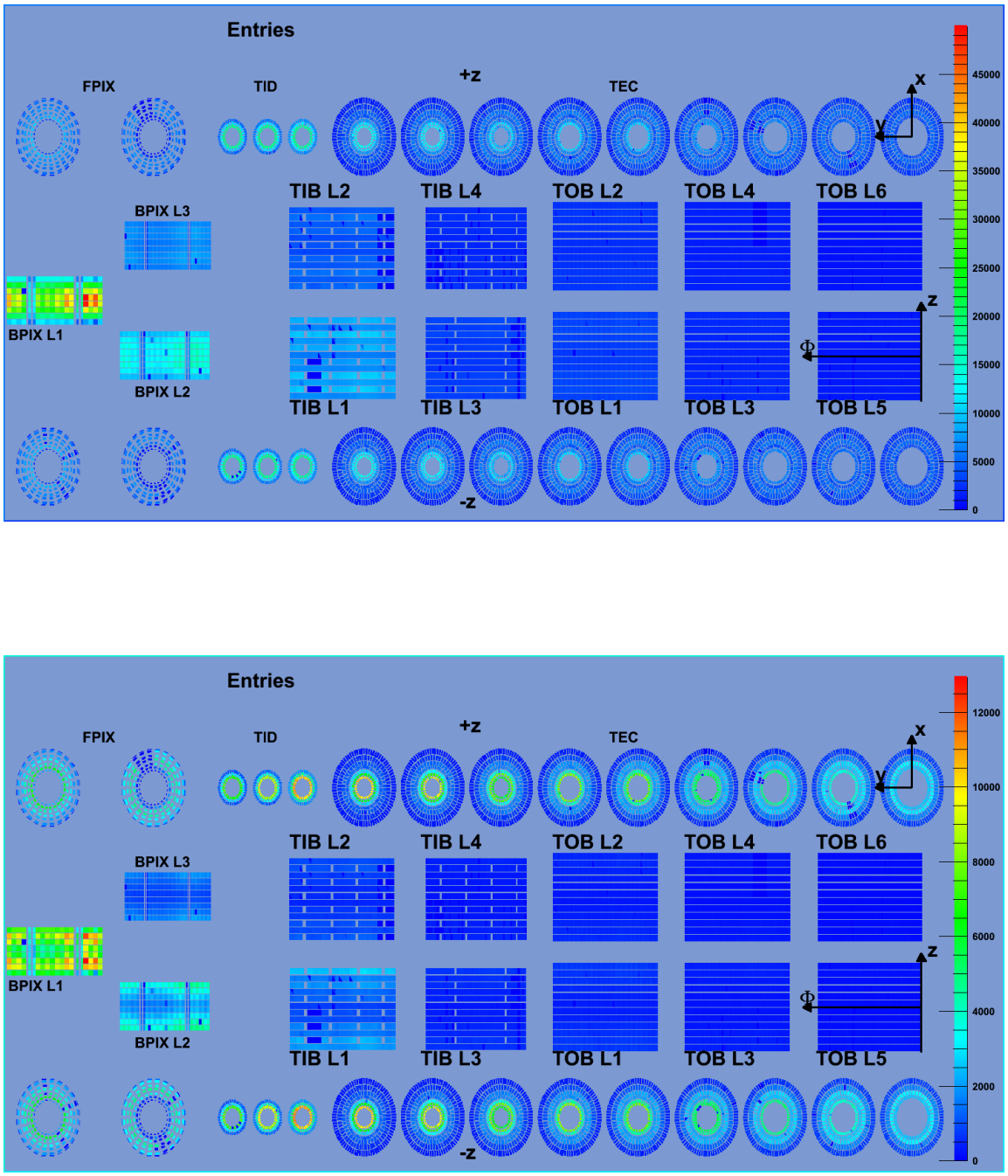

Figure G.2: Tracker map for tracks from minimum bias events before (top) and after (bottom) the alignment track selection.

Appendix H

B-tagging Performance with respect to c quarks

The b-tagging performance shown for the misidentification efficiencies for c quarks plotted versus the b-tagging efficiency. Since the topology of b and c jets differs less than for b jets and jets from light quarks, the impact of misalignment affects the corresponding b-tagging efficiencies and c-misidentification efficiencies only slightly. Even for the b probability algorithm which has shown b-tagging efficiency drops of more than 20% for the $10\,\mathrm{pb}^{-1}$-scenario for fixed misidentification values for u,d and quarks, the b-tagging efficiency is not affected more than 5-10% for fixed values of c quark misidentification.

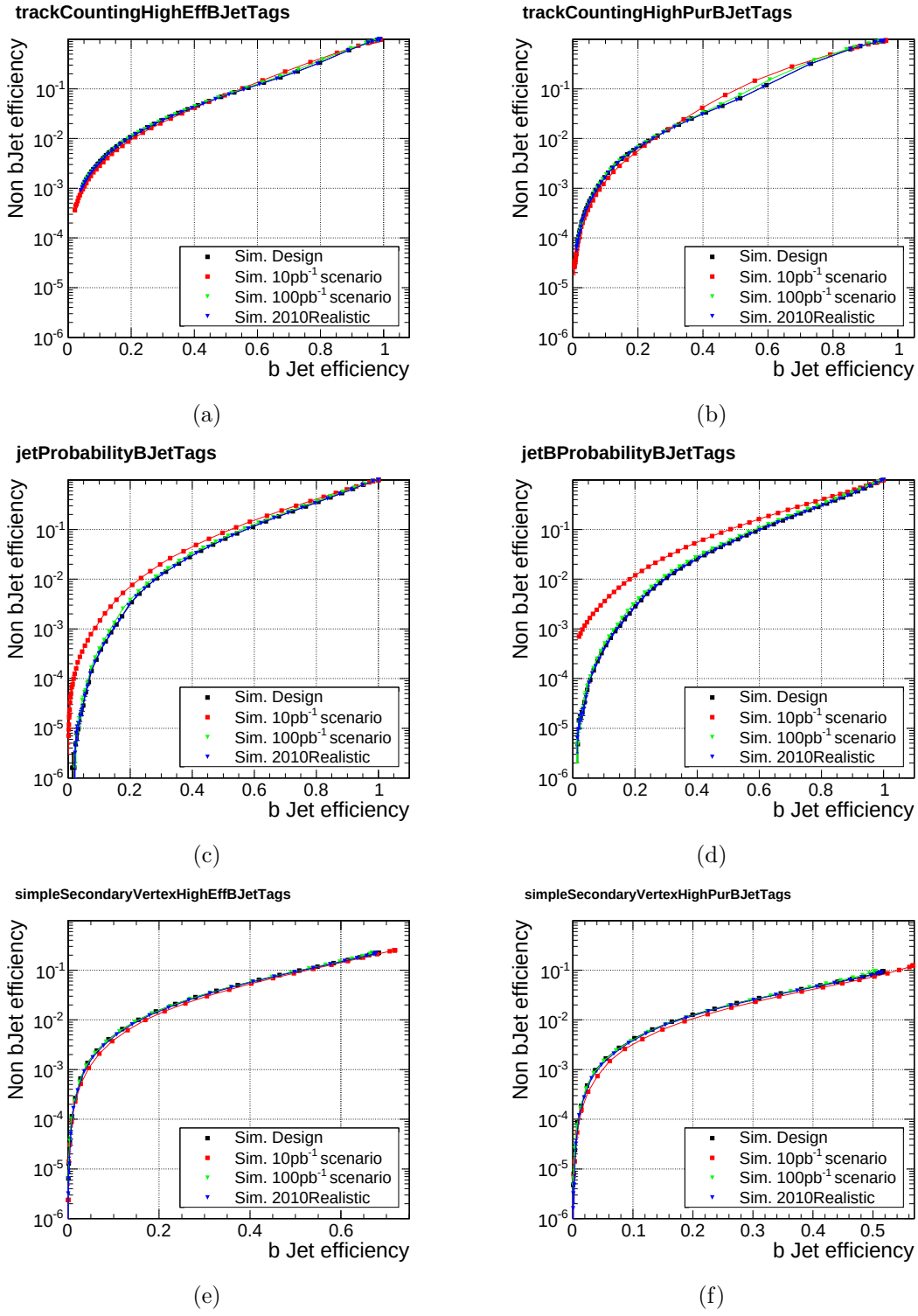

Figure H.1: c quark mistag vs b-tagging efficiency for TCHE (a), TCHP (b), jet probability (c), jet b probability (d), SSVHE (e) and SSVHP (f) for different misalignment scenarios.

Appendix I

Sensitivity Studies of the K_S Resonance to Systematic Misalignment

Since the cross section for the production of K_S is large compared to for example the Z boson, even the first weeks of collision data taking in 2010 provided sufficient data to study the K_S-mass differentially in $|\eta|$ and ϕ. The study presented here was intended to test the sensitivity of the K_S-mass with respect to weak modes of the tracker alignment as described in section 4.3. The tracks used for the vertex reconstruction are required to have:

- a normalized χ^2 >5,
- at least 6 hits and
- an impact parameter significance < 2.

The vertices are considered further if they have:

- a normalized χ^2 >7 and
- a 2d-vertex significance $< 15\,\text{cm}$.

The K_S-mass window is defined as $\pm 0.07\,\text{GeV}$ around the nominal K_S mass of $497.672 \pm 0.031\,\text{MeV}$ [2].

In order to investigate the impact of possible weak modes, the nine possible detector deformations introduced in figure 4.4 have been used to distort an aligned detector geometry, described in [71]. The same alignment used to produce this geometry has been rerun starting from the nine artificially distorted geometries. The resulting 'realigned' geometries are then used to refit the tracks and repeat the K_S analysis. Figures I.1-I.3 show the K_S-mass bias as a function of $|\eta|$ of track with lowest transverse momentum for the original aligned geometry referred to as 'ICHEP' and

the realigned geometries, named after the additionally applied distortion. The deviations are all within the error bars. The observed bias is the same for all geometries and thus seems to be related to other effects than the detector geometry. Even design conditions in the simulation show a similar behaviour shown in figure I.4. Although the distributions for the simulation are overall shifted towards higher values of the K_S-mass, the shape is very similar to the one observed in data which substantiate the conclusion of non-alignment related reasons for the bias.

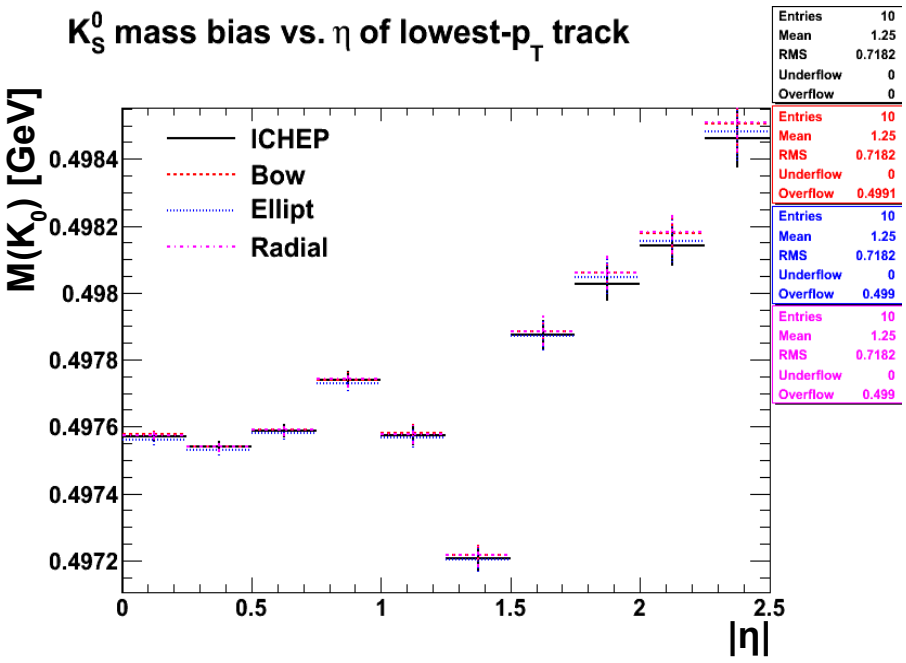

Figure I.1: K_S-mass as a function of $|\eta|$ for systematic misalignments affecting global r compared to reference geometry 'ICHEP'.

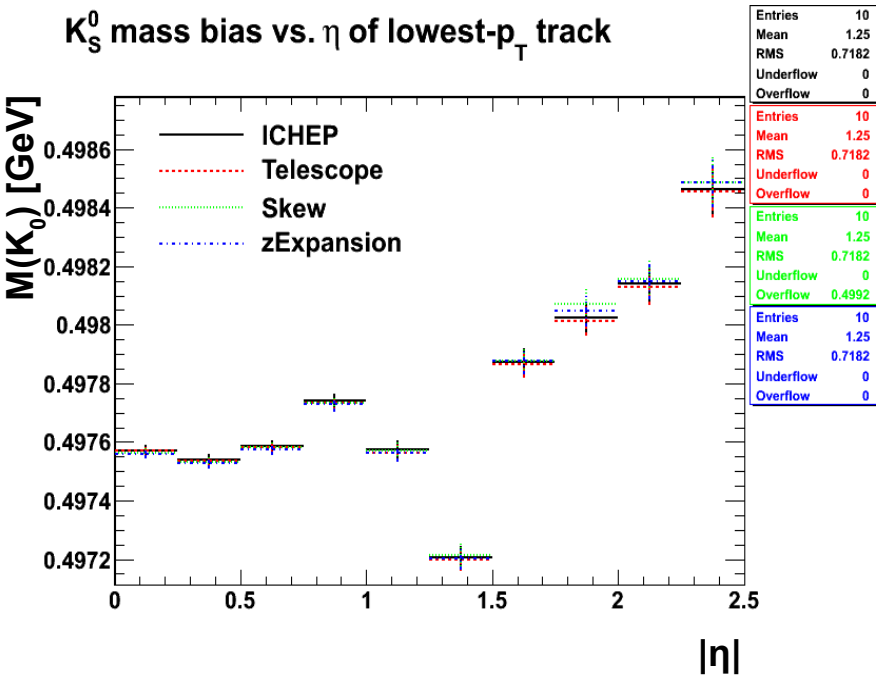

Figure I.2: K_S-mass as a function of $|\eta|$ for systematic misalignments affecting global z compared to reference geometry 'ICHEP'.

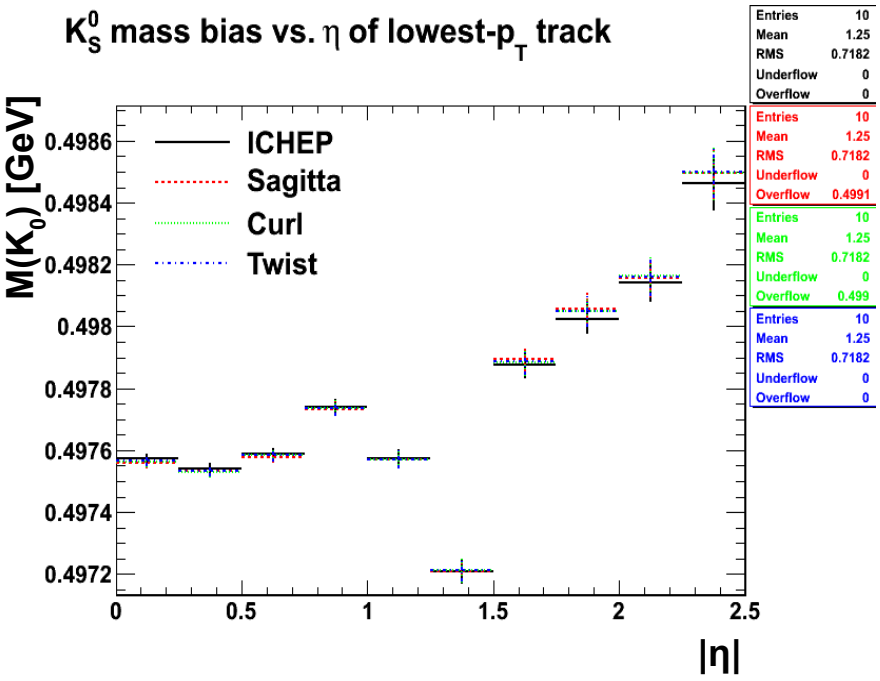

Figure I.3: K_S-mass as a function of $|\eta|$ for systematic misalignments affecting global $r\Delta\phi$ compared to reference geometry 'ICHEP'.

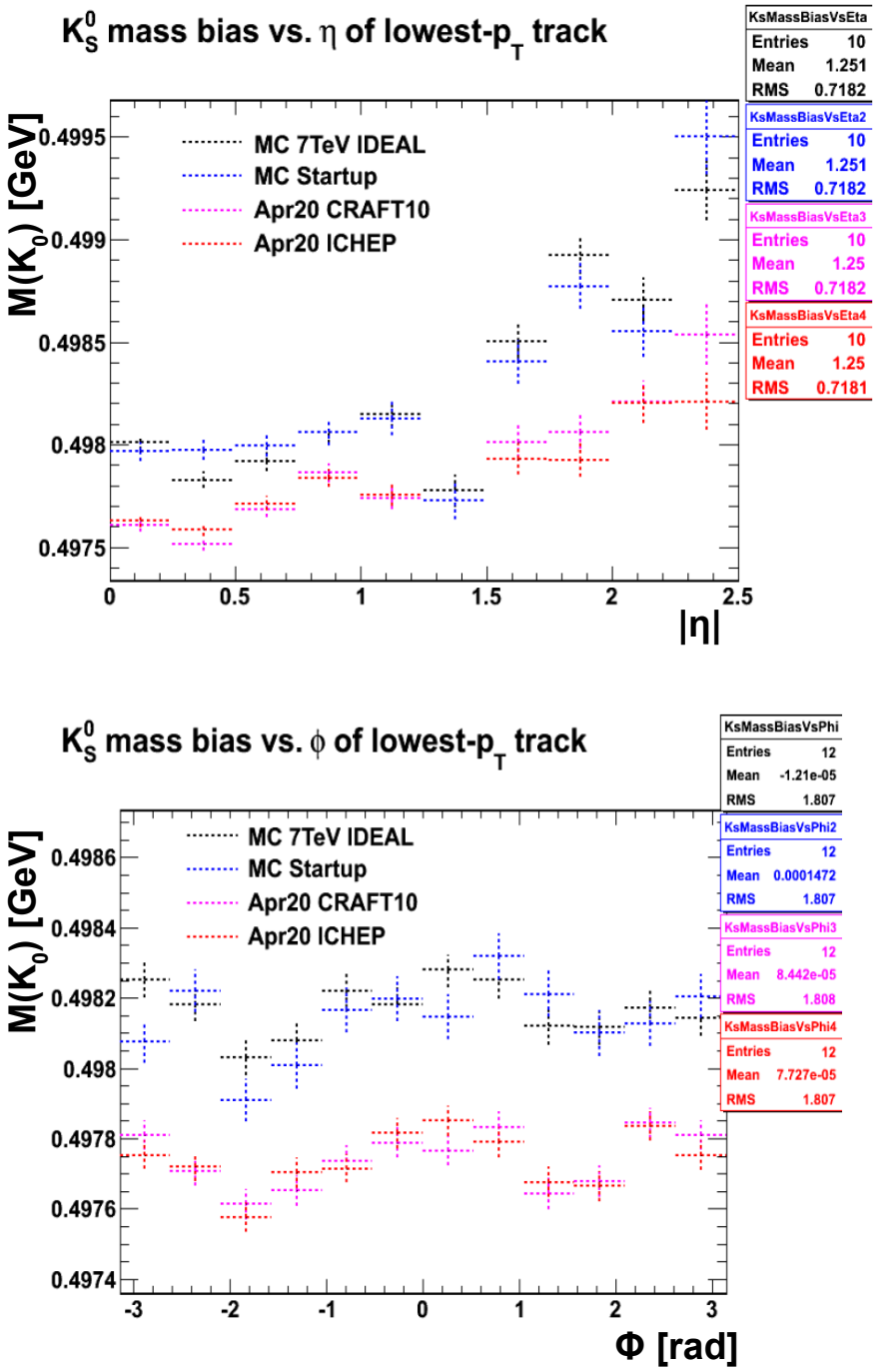

Figure I.4: K_S-mass as a function of $|\eta|$ and ϕ for data and simulation.

Appendix J

Voigtian Fits to the Z boson mass

The following plots show the fit of a Voigtian distribution to the invariant mass of the two isolated muons with leading transverse momentum in bins of $-2.4 < \eta < 2.4$. The fitted mean value is the input for the plots shown in section 6.2.2. The statistic in the outermost bin of $2.0 < |\eta| < 2.4$ has only few entries because the muons were required to be within $|\eta| < 2.1$ in order to stay within the $|\eta|$ region covered by the tracker ($|\eta| < 2.4$) when applying the isolation radius of 0.3. Therefore, the fit results in the outermost bins are not considered in the systematic studies in section 6.2.2.

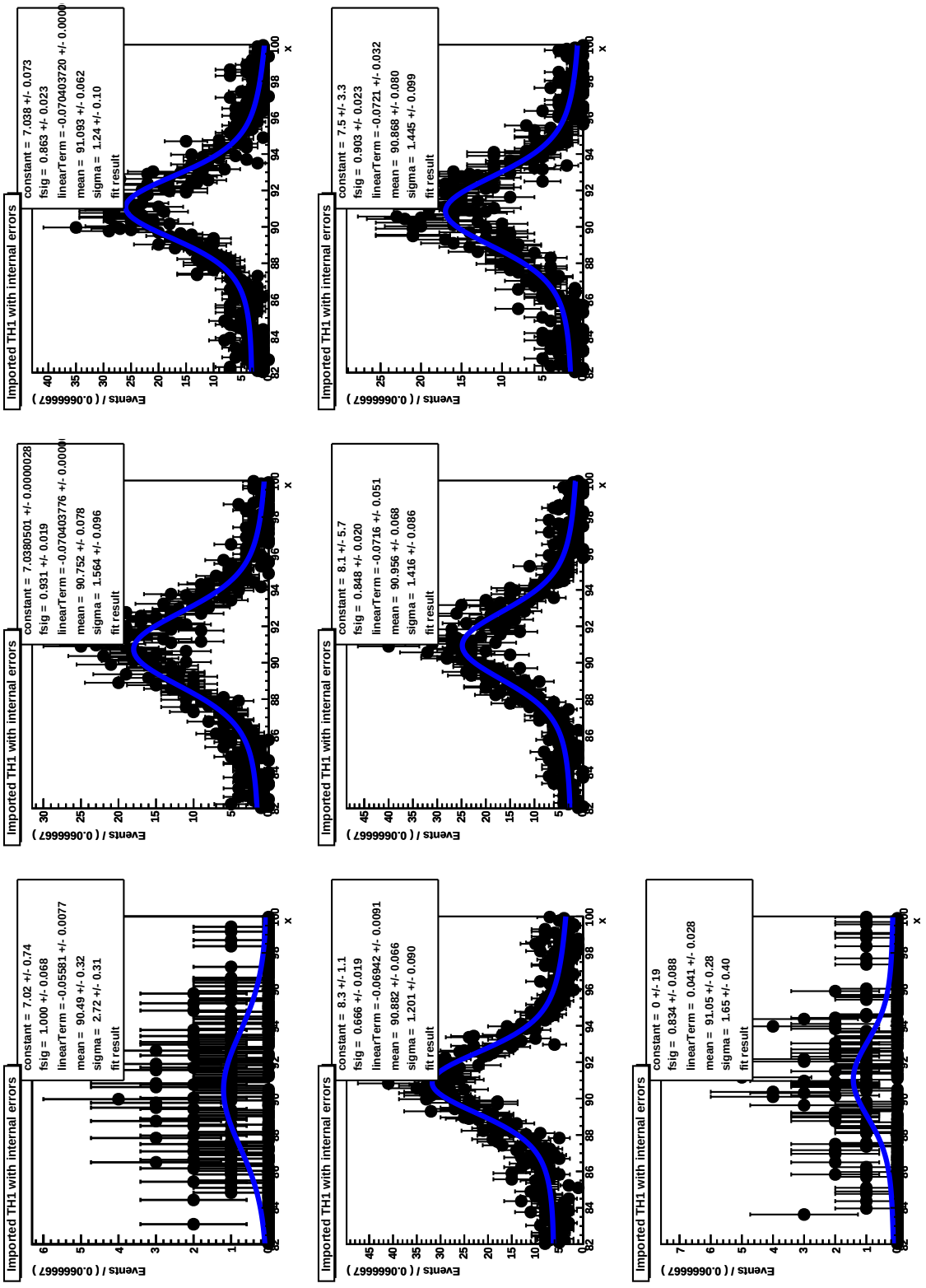

Figure J.1: Fit results of Z boson mass for different η-ranges of positive charged muon for geometry GR10_v4.

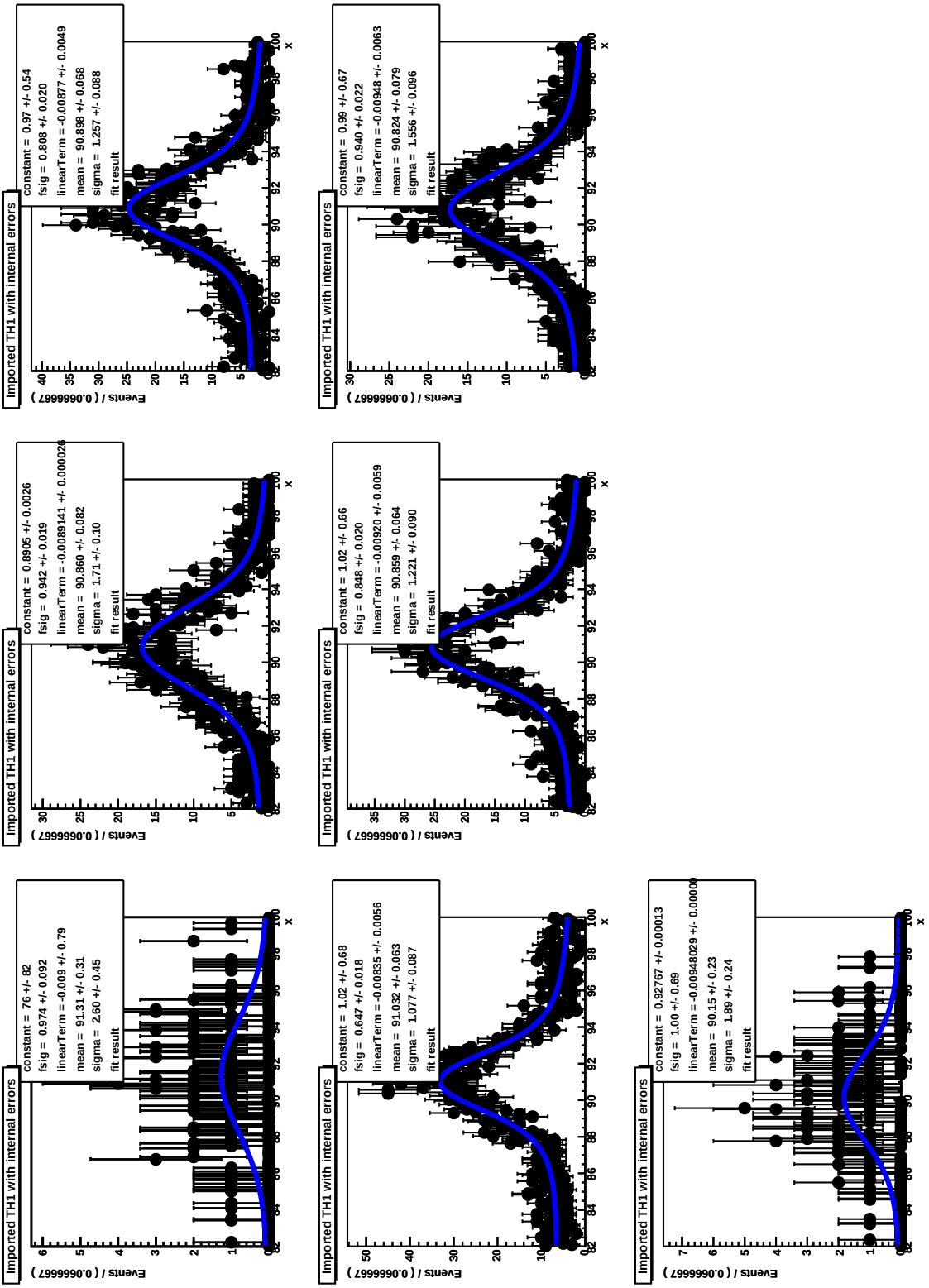

Figure J.2: Fit results of Z boson mass for different η-ranges of negative charged muon for GR10_v4.

Bibliography

[1] J. M. Campbell, J. W. Huston, and W. J. Stirling. Hard interactions of quarks and gluons: a primer for lhc physics. *Reports on Progress in Physics*, 70(1):89, 2007. 7, 13, 14, 15

[2] K Nakamura et al. Review of particle physics. *J. Phys.*, G37:075021, 2010. 7, 8, 10, 12, 19, 20, 21, 53, 54, 94, 131

[3] CMS collaboration. The CMS experiment at the CERN LHC. *JINST*, 3:S08004, 2008. 7, 25, 26, 27, 28, 29, 31, 33, 34, 35, 36, 38

[4] V. Khachatryan, A. M. Sirunyan, A. Tumasyan, W. Adam, T. Bergauer, M. Dragicevic, J. Erö, C. Fabjan, M. Friedl, R. Frühwirth, and et al. CMS tracking performance results from early LHC operation. *European Physical Journal C*, 70:1165–1192, December 2010. 7, 31

[5] V. Blobel. *Millepede II Linear Least Squares Fit with a Large Number of Parameters, http://www.desy.de/ blobel/Mptwo.pdf*, 2007. 8, 46, 47, 49

[6] A. Bonato. Weak modes in alignment. Technical report, 2011. 8, 51, 52

[7] V. Blobel, C. Kleinwort, and F. Meier. Fast alignment of a complex tracking detector using advanced track models. March 2011. 8, 55, 56

[8] A. Osorio-Oliveros F. Loddo, K. Buńkowski. The rpc technical trigger: A cosmic trigger and more for the cms experiment. Technical report, 2010. 8, 64

[9] CMS collaboration. Cms tracking performance results from early lhc operation. oai:cds.cern.ch:1277738. Jul 2010. 8, 68, 69, 71

[10] A. Rizzi, F. Palla, and G. Segneri. Track impact parameter based b-tagging with cms. Technical Report CMS-NOTE-2006-019. CERN-CMS-NOTE-2006-019, CERN, Geneva, Jan 2006. 8, 84, 85, 86

[11] CMS Collaboration. Commissioning of b-jet identification with pp collisions at sqrt(s) = 7 tev. 2010. 8, 84, 86, 87

[12] H. Enderle. *Determination of Momentum Biases in the Tracker Alignment and First Differential $t\bar{t}$ Production Cross Section Measurement at CMS (working title)*. PhD thesis, to be published 2011. 8, 97, 98

[13] K. Kodama et al. Observation of tau-neutrino interactions. *Phys. Lett.*, B504:218–224, 2001. 4

[14] S. L. Glashow, J. Iliopoulos, and L. Maiani. Weak interactions with lepton-hadron symmetry. *Phys. Rev. D*, 2(7):1285–1292, Oct 1970. 5

[15] S. Dawson. Introduction to electroweak symmetry breaking. 1998. 8

[16] ALEPH Collaboration, CDF Collaboration, D0 Collaboration, DELPHI Collaboration, L3 Collaboration, OPAL Collaboration, SLD Collaboration, LEP Electroweak Working Group, Tevatron Electroweak Working Groupa, and SLD electroweak heavy flavour groups. Precision Electroweak Measurements and Constraints on the Standard Model. 2010. 11

[17] V. Khachatryan et al. Transverse momentum and pseudorapidity distributions of charged hadrons in pp collisions at sqrt(s) = 0.9 and 2.36 TeV. *JHEP*, 02:041, 2010. 13, 62

[18] S. D. Drell and T.-M. Yan. Massive lepton-pair production in hadron-hadron collisions at high energies. *Phys. Rev. Lett.*, 25(5):316–320, Aug 1970. 14

[19] W.R. Leo. *Techniques for Nuclear and Particle Physics Experiments*. Springer-Verlag, 1987. 16, 18

[20] Ch. Berger. *Elementarteilchenphysik*. Springer-Verlag, 2002. 17

[21] J.W. Cronin. Cosmic rays: The most energetic particles in the universe. *Review of Modern Physics*, 71, 1999. 21

[22] P. K. F. Grieder. *Cosmic rays at earth: Researcher's reference, manual and data book*. Elsevier, 2001. 20

[23] (ed.) Evans and (ed.) Bryant. LHC Machine. *JINST*, 3:S08001, 2008. 24

[24] CERN Press Office. Cern announces lhc to run in 2012 . http://public.web.cern.ch/press/pressreleases/Releases2011/PR01.11E.html, January 2011. 24

[25] CMS Collaboration. Cms luminosity - public results . https://twiki.cern.ch/twiki/bin/view/CMSPublic/LumiPublicResults. 24

[26] ALICE collaboration. The ALICE experiment at the CERN LHC. *JINST*, 3:S08002, 2008. 25

[27] LHCb collaboration. The LHCb Detector at the LHC. *JINST*, 3:S08005, 2008. 25

[28] ATLAS collaboration. The ATLAS Experiment at the CERN Large Hadron Collider. *JINST*, 3:S08003, 2008. 25

[29] LHCf collaboration. The LHCf detector at the CERN Large Hadron Collider. *JINST*, 3:S08006, 2008. 25

[30] TOTEM collaboration. The TOTEM experiment at the CERN Large Hadron Collider. *JINST*, 3:S08007, 2008. 25

[31] J.-L. Caron. Lhc project illustrations, May 1998. 25

[32] G. A. Giurgiu and for the CMS collaboration. Pixel Hit Reconstruction with the CMS Detector. *ArXiv e-prints*, August 2008. 28

[33] V. Radicci. Operational experience and performance of the cms pixel detector during the first lhc beams. Technical Report CMS-CR-2010-117. CERN-CMS-CR-2010-117, CERN, Geneva, Jul 2010. 28

[34] S. Gadomski, G. Hall, T. S. Høgh, P. Jalocha, E. Nygård, and P. Weilhammer. The deconvolution method of fast pulse shaping at hadron colliders. 1992. 31, 121

[35] C.Genta & B.Mangano P.Lenzi. Track reconstruction of real cosmic muon events with CMS tracker detector. *J. Phys.: Conf. Ser.*, 119(3):032030, 2008. 38, 41, 42

[36] D. Notz R. K. Bock, H. Grote and M. Regler. *Data analysis techniques for high-energy physics experiments*. Cambridge University Press, 1990. 39, 40

[37] Thomas Speer, Kirill Prokofiev, R FrÃ$\frac{1}{4}$hwirth, Wolfgang Waltenberger, and Pascal Vanlaer. Vertex fitting in the cms tracker. Technical Report CMS-NOTE-2006-032. CERN-CMS-NOTE-2006-032, CERN, Geneva, Feb 2006. 40

[38] C. Kleinwort and F. Meier. Alignment of the CMS Silicon Tracker – and how to improve detectors in the future. *ArXiv e-prints*, October 2010. 42, 43

[39] C. Kleinwort. Strip resolution from alignment pulls . https://indico.cern.ch/contributionDisplay.py?contribId=6&confId=80863, Januar 2010. 44

[40] Torbjorn Sjostrand, Stephen Mrenna, and Peter Z. Skands. PYTHIA 6.4 Physics and Manual. *JHEP*, 05:026, 2006. 43

[41] J. Alwall, P. Demin, S. de Visscher, R. Frederix, M. Herquet, F. Maltoni, and T. Stelzer. *MadEvent - a multi-purpose event generator - powered by MadGraph*, March 2007. 43

[42] P. A. Biallass, T. Hebbeker, and K. Hoepfner. Simulation of Cosmic Muons and Comparison with Data from the Cosmic Challenge using Drift Tube C hambers. CMS-NOTE-2007-024. 43

[43] S. Agostinelli et al. G4–a simulation toolkit. *Nuclear Instruments and Methods in Physics Research Section A: Accelerators, Spectrometers, Detectors and Associated Equipment*, 506(3):250 – 303, 2003. 43

[44] F. P. Schilling. Track reconstruction and alignment with the cms silicon tracker. Technical Report physics/0610005, Oct 2006. Manuscript not submitted to the proceedings ICHEP06. 45

[45] V. Karimäki, T. Lampen, and F.-P. Schilling. The hip algorithm for track based alignment and its application to the cms pixel detector. Technical Report CMS-NOTE-2006-018. CERN-CMS-NOTE-2006-018, CERN, Geneva, Jan 2006. 46

[46] V. Blobel. Millepede 2 in 2009, 3rd lhc detector alignment workshop. In *https://indico.cern.ch/contributionDisplay.py?contribId=0&confId=50502*. 48, 51, 52

[47] J. Nocedal. Updating quasi-newton matrices with limited storage. *Mathematics of Computation*, 35(151):773–782, 1980. 48

[48] M. Stoye. *Calibration and Alignment of the CMS Silicon Tracking Detector*. PhD thesis, University of Hamburg, 2007. 48

[49] V. Blobel. A new fast track-fit algorithm based on broken lines. *Nuclear Instruments and Methods in Physics Research Section A: Accelerators, Spectrometers, Detectors and Associated Equipment*, 566(1):14 – 17, 2006. TIME 2005 - Proceedings of the 1st Workshop on Tracking in High Multiplicity Environments. 53

[50] Are Strandlie and W Wittek. Propagation of covariance matrices of track parameters in homogeneous magnetic fields in cms. Technical Report CMS-NOTE-2006-001. CERN-CMS-NOTE-2006-001, CERN, Geneva, Jan 2006. 54

[51] A. Strandlie and W. Wittek. Derivation of jacobians for the propagation of covariance matrices of track parameters in homogeneous magnetic fields. *Nuclear Instruments and Methods in Physics Research Section A: Accelerators, Spectrometers, Detectors and Associated Equipment*, 566(2):687 – 698, 2006. 54

[52] V. Blobel and E. Lohrmann. *Statistische und numerische Methoden der Datenanalyse*. Teubner Verlag, 1 edition, 1998. 56

[53] G. Flucke. The alignment software framework in cmssw. private communication. 57

[54] V. Blobel. Millepede source code . http://svnsrv.desy.de/public/MillepedeII/tags/V03-03-00/. 57

[55] C. Kleinwort. Mpii - parallelization . http://indico.desy.de/getFile.py/access?contribId=0&sessionId=0&resId=0%&materialId=slides&confId=3235. 58

[56] CMS Collaboration. Alignment of the cms silicon tracker during commissioning with cosmic rays. *JINST*, 5(03):T03009, 2010. 59, 61, 67, 75

[57] M. Swartz, D. Fehling, G. Giurgiu, P. Maksimovic, and V. Chiochia. A new technique for the reconstruction, validation, and simulation of hits in the CMS pixel detector. *PoS*, VERTEX2007:035, 2007. 61, 62

[58] M. Musich. *The Alignment of the CMS Tracker and its Impact on the early Quarkonium Physics*. PhD thesis, Universit'a degli Studi di Torino, 2011. 62, 78, 79

[59] T. Lampen, M. Weber, N. de Filippis, and A. Schmidt. Misalignment scenarios for the startup conditions of the cms tracker. Internal note, 2007. CMS IN-2007/061. 67

[60] M. Musich. Review of current ape . https://indico.cern.ch/contributionDisplay.py?contribId=13&confId=82615, October 2010. 75

[61] A. Whitbeck. Updated primary vertex validation trend plots. private communications, Nov 2010. 80, 81

[62] CMS Collaboration. Impact of tracker misalignment on the cms b-tagging performance. Aug 2009. 83, 84, 88

[63] CMS Collaboration. Algorithms for b jet identification in cms. Jul 2009. 86

[64] Cms Collaboration. Measurement of the w and z inclusive production cross sections at sqrts=7 tev with the cms experiment at the lhc. 2011. 93

[65] S. Bolognesi, M.A. Borgia, R. Castello, C. Mariotti, M. De Mattia, and T. Dorigo. Calibration of track momentum using dimuon resonances in cms. *Internal note*, 059, 2010. 93, 99

[66] W. Verkerke and D. Kirkby. *RooFit_Users_Manual_2.07-29*, v2.07 edition, 2006. 94

[67] E. Widl. *Global Alignment of the CMS Tracker*. PhD thesis, Technische Universität Wien, 2008. 100

[68] A. Spiridonov. Alignment with 0t cosmics . https://indico.cern.ch/contributionDisplay.py?contribId=8&confId=127125, Juni 2011. 100

[69] C. Kleinwort. Brokenlinesfine - general broken lines @ cms . http://indico.cern.ch/getFile.py/access?contribId=8&sessionId=1&resId=0-&materialId=slides&confId=117160. 115

[70] B. Hooberman, K. Burkett, S. Tkaczyk, and A.Venturi. Charge collection in deco mode in sst. 121, 122, 123, 124

[71] J. Draeger. The alignment of the cms silicon tracker. Technical Report CMS-CR-2010-207. CERN-CMS-CR-2010-207, CERN, Geneva, Nov 2010. 131

Acknowledgement

Regarding the last three years I was working within the CMS collaboration I have to thank particle physics for being fascinating and challenging at once such that thousands of physicists put their efforts together and build projects like LHC and the CMS detector. I want to thank Prof. Peter Schleper for his key role in awaking my fascination for particle physics and for the possibility to work in the international environment at CERN and clearly for the unique memory of the first event display showing 7 TeV collisions. I am grateful for his encouragement and supervision. His detailed and elaborate comments have been very helpful and improved this work.
I am greatly indebted to Prof. Ernesto Migliore referring this thesis and to Prof. Johannes Haller and Dr. Erika Garutti for having agreed to referring the thesis defence.
Major thanks are not enough to appreciate the continuous supervision by Prof. Ernesto Migliore, Dr. Gero Flucke and Dr. Alessio Bonato, their trust in me, and the interesting discussions of achieved results and suggestions for further studies.
Furthermore, I want to thank Dr. Hartmut Stadie for his patient help concerning any kind of technical problems and of course his encouragements and supervision in the process of writing this thesis.
Last but not least my thanks goes to all the nice colleagues who contributed to the friendly atmosphere in our group, our office and of course in the coffee kitchen.